A new scanning force microscope for temperature-controlled static and dynamic friction measurements, using an extended normal and lateral working range with high spatial resolution

INAUGURALDISSERTATION
zur
Erlangung der Würde eines Doktors der Philosophie
vorgelegt der
Philosophisch-Naturwissenschaftlichen Fakultät
der Universität Basel

von

Dipl.-Ing. Jörn Selbeck
aus Potsdam, Deutschland

BASEL, 2013

Genehmigt von der Philosophisch-Naturwissenschaftlichen Fakultät
auf Antrag von:

Professor Dr. Ernst Meyer
Professor Dr. Martino Poggio

Basel, den 17.09.2013

_____

Dekan

Professor Dr. Jörg Schibler

Namensnennung-Keine kommerzielle Nutzung-Keine Bearbeitung 3.0 Schweiz
(CC BY-NC-ND 3.0 CH)

Sie dürfen: Teilen — den Inhalt kopieren, verbreiten und zugänglich machen

Unter den folgenden Bedingungen:

Namensnennung — Sie müssen den Namen des Autors/Rechteinhabers in der von ihm festgelegten Weise nennen.

Keine kommerzielle Nutzung — Sie dürfen diesen Inhalt nicht für kommerzielle Zwecke nutzen.

Keine Bearbeitung erlaubt — Sie dürfen diesen Inhalt nicht bearbeiten, abwandeln oder in anderer Weise verändern.

Wobei gilt:

- **Verzichtserklärung —** Jede der vorgenannten Bedingungen kann **aufgehoben** werden, sofern Sie die ausdrückliche Einwilligung des Rechteinhabers dazu erhalten.
- **Public Domain (gemeinfreie oder nicht-schützbare Inhalte) —** Soweit das Werk, der Inhalt oder irgendein Teil davon zur Public Domain der jeweiligen Rechtsordnung gehört, wird dieser Status von der Lizenz in keiner Weise berührt.
- **Sonstige Rechte —** Die Lizenz hat keinerlei Einfluss auf die folgenden Rechte:
  - Die Rechte, die jedermann wegen der Schranken des Urheberrechts oder aufgrund gesetzlicher Erlaubnisse zustehen (in einigen Ländern als grundsätzliche Doktrin des **fair use** bekannt);
  - Die **Persönlichkeitsrechte** des Urhebers;
  - Rechte anderer Personen, entweder am Lizenzgegenstand selber oder bezüglich seiner Verwendung, zum Beispiel für **Werbung** oder Privatsphärenschutz.
- **Hinweis —** Bei jeder Nutzung oder Verbreitung müssen Sie anderen alle Lizenzbedingungen mitteilen, die für diesen Inhalt gelten. Am einfachsten ist es, an entsprechender Stelle einen Link auf diese Seite einzubinden.

Quelle: http://creativecommons.org/licenses/by-nc-nd/3.0/ch/ Datum: 12.11.2013

Acknowledgement

This dissertation would not have been possible without the support of many people and organizations. First, I would like to thank my parents, my wife, my children and my parents in law, for their love, kindness and support they have given during the years it has taken me to finalize this work.
I would like to thank Professor Dr. Ernst Meyer from the University of Basel, department of physics for his kind assistance and guidance, which was certainly not always easy due to the large distance between my working place in Berlin and his working place in Basel. Furthermore, the author would also like to convey thanks to Professor Dr. Martino Poggio from the department of physics as well, for his acceptance of the co-referee of my work.
The work take place at the federal institute for materials research and testing (BAM) in Berlin. Doctor habil. Eckhard Schulz and Professor Dr. Heinz Sturm were my advisors there. Both of them were abundantly helpful and offered invaluable assistance, support and guidance. This work would be not created without them.
A special gratitude I give to Doctor Volker Dworak, a friend of mine, and the colleague where I have worked together for more than ten years. His contribution in stimulating suggestions and encouragement has even been affected my work.
A further thank is addressed to the federal ministry of economics and technology (BMWi) as well as the 'Technologiestiftung Berlin' (TSB) for their funding of the two projects.
Finally yet importantly, I would like to thank the executive board of the Leibniz Institute for agricultural engineering Potsdam-Bornim (ATB) and especially Doctor Detlef Ehlert, head of the department of engineering for crop production who believe in me, finalize this dissertation and gave me the opportunity to work as a senior scientist in his department.

Contents

List of Symbols and Acronyms

4Q-PD	4-quadrant photodiode
8B10B	8 bit to 10 bit code
A	Surface area
A_{eff}	Effective surface area
ADC	Analogue to digital converter
AFM	Atomic force microscope
AWG	American wire gauge
C_e	Electrical capacitance
C_F	Filter capacitance
$C_{barrier}$	Electrical barrier capacitance
C_h	Thermal capacity
d_{Beam}	Diameter of a beam
d_{Sphere}	Diameter of a sphere
DAC	Digital to analogue converter
DMT	Deryaguin-Muller-Toporov
DSP	Digital signal processor
E	Young's modulus
E_m	Elastic modulus
E_x	Radiation exchange grade
ECU	Electronic control unit
$F_{cut\text{-}off}$	Cut-off frequency
F	Force
FFM	Friction force microscope
FIR	Finite impulse response
h_0	Equilibrium distance
I	Second moment of area
I_a	Area moment of inertia
I_{Bias}	Bias current
I_{dc}	Direct current
I_{PD}	Photodiode current
I_{JN}	Johnson noise current

I_{SNDark}	Dark shot noise current
$I_{SNPhoto}$	Photo shot noise current
I_{hf}	Heat flow
JKR	Johnson-Kendall-Roberts
K	Reduced Young's modulus
kSPS	Kilo samples per second
l	Length
l_{cond}	Conduction length
n	Refractive index
NA	Numerical aperture
LED	Light-emitting diode
LJ	Lennard-Jones
MD	Maugis-Dugdale
MSPS	Mega samples per second
NEP	Noise equivalent power
NTC	Negative temperature coefficient
NaCl	Sodium chloride
OP	Operational amplifier
P	Adhesive component of the total load
P_a	Adhesive component of the load
P_r	radiation power
PD	Photo diode
PI	Proportional/Integral (in terms of feedback circuit)
P-LED	Power-LED
PSD	Position sensitive device
Q	Heat flux
R_e	Electrical resistance
R_{Fx}	Filter resistance
R	Reference resistance
R_h	Heat resistance
R_s	Reduced sphere radius
SFB	Sonderforschungsbereich
SFM	Scanning force microscope

STM	Scanning tunneling microscope
T	Temperature
t	Time
T_{env}	Ambient temperature
U	Voltage
$U_{A,B,C,D}$	Voltages on one of the four sections of a 4Q-PD
U_{Bias}	Bias voltage
U_{Block}	Block voltage
U_{In}	Input voltage
U_L	Lateral voltage on a 4Q-PD
U_N	Normal voltage on a 4Q-PD
U_{Out}	Output voltage
UHV	Ultra high vacuum
ULE glass	Ultra low expansion glass
W_a	Work of adhesion
x, y, z	Spatial coordinates
X, Y, Z	Spatial coordinates in terms of hardware labelling
z_0	Characteristic atomic dimension
α	Angle
α_{conv}	convection coefficient
Δf_{BW}	Band width
ε	Emission coefficient
λ_{cond}	Thermal conductivity
λ_p	Responsivity of a photo detector
λ_T	Tabor parameter
ρ	Density
σ	Boltzmann constant
δ	Angle of tilt
δ_l	Elastic compression
μ	Classical friction coefficient

1 Introduction

"We brake everything" was an advertising slogan used by a manufacturer of brake pads and systems in the 1980's. While this was not a scientific statement, a Nobel Prize was awarded in the same decade for the scanning tunneling microscope[1] (STM) invented by G. K. Binnig and H. Rohrer in 1981 for which they were awarded the Nobel Prize in 1986. An enhancement of this device was the so-called scanning force microscope[2] (SFM) that was improved later to measure friction on the nanometre scale. The SFM is an evolution of the scanning tunnelling microscope, which was based on R. Young's topografiner[3] that was introduced in 1971.
The SFM that is commercially available today offers an enormous variety of measurement modes, such that many research groups can modify their systems for specialised physical, chemical, magnetic, electrical and biological problems.
To accommodate increasingly complex scientific questions, even the state-of-the-art SFM require upgrades. An enlarged scan area is required, for example, to observe interfacial phenomena or macroscopic scratches. However, it is very complicated to extend the maximum scan width of the SFM while maintaining the same scan resolution as for small scan areas. The dilemma between a larger scan range and an equal or higher spatial resolution results in a large increase in the amount of electronics - e.g. more bits for analogue to digital converter (ADC) and digital to analogue converter (DAC), and better signal to noise ratio of preamplifiers - mechanics and software required. Furthermore, the goal is a more extensive characterisation of the sample in only one measurement: therefore, the number of data input channels and the number of actuators must be increased. A larger number of input channels is necessary to collect specific information about the sample. While humidity, temperature and pressure parameters can currently be measured, these parameters could also be controlled with the new actuators to show the influence of such parameters on the sample or the scan. However, controlling environmental parameters can also cause novel critical behaviours. An example of such critical behaviour is related to the Curie temperature of piezo elements. The piezos depolarise above the critical temperature and lose their piezoelectric properties. Symmetric construction, active temperature compensation and an extended spatial error correction and linearization system must also be developed to reduce measurement errors.
An additional difficulty arises in heating samples containing volatile components that condense on the cantilever and the cantilever tip, changing the tip geometry and electrical and mechanical contact features[4,5]. A separate temperature-controlled cantilever can reduce or completely avoid the condensation during heating, or vice versa, the cantilever can be cooled to increase the condensation ratio[6], if needed.
The heated cantilever may even be used in thermal lithography[7,8]. Furthermore, the sample can be heated to a temperature slightly lower than the modification temperature so that the cantilever works faster due to the reduced thermal load.


Fig. 1-1 Brake endurance test

For friction measurements, an exact separation between the normal and lateral bending of the cantilever is necessary to reduce possible cross-talk between modes. A perfectly glued or clamped cantilever-substrate for optimal temperature and electric conductivity to the cantilever holder can eliminate torsion or inclination of the cantilever.
The glowing brake disc shown in Fig. 1-1 is an example of the requirements of a modern scanning force microscope system. Sonderforschungsbereiche[9] (SFB of the Deutsche Forschungsgemeinschaft) are conducting research on these brake discs and pads. Such pads can consist of up to 100 different components in different amounts and particle

sizes, embedded in polymers such as synthetic resins. A microscopic analysis of the sample topography, stiffness and friction is required following the endurance test shown in Fig. 1-1.
In this work, a new and improved SFM is presented. This SFM can measure many variables such as the individual dynamic and active temperature regulation of the sample and the cantilever, miscellaneous friction modes, x-, y-, z- linearization and an increased scan speed, simultaneous with high spatial resolution. The scan width is also laterally extended to 1 millimetre by 1 millimetre. This extension of the lateral scan range requires a larger tilt compensation. Therefore, the z-scanner has a range of more than 300 µm.
Detailed points are illustrated by examples of solutions designed for specific cases. Due to the discussed requirements, first the design of the cantilever and sample holder for temperature-controlled experiments on friction are discussed. The independent heating and cooling setups of the cantilever holder and the sample holder and the possible use of the bother holders are illustrated. With respect to the high temperature range, a failure-minimised detection of the normal and lateral cantilever deflection are shown. In detail, the advantages of a fibre optical light source for the beam deflection, the beam guidance in a prism, the positioning setup for the beam on the cantilever and the adjustment of the 4-quadrant photodiode in all three dimensions are described. The needful large scan range of 1 mm square assumes a new displacement setup. This leads to a separation of the dynamic behaviour of the Z-direction, a use of a hydraulic drive alternative to the piezo drive and a new type of linearization that is lightweight and can cope with the high dynamic spatial range. Last, the electronic control unit and software are examined. Described are the processor control and timing of the electronic control unit, the software on this unit for communicating with the PC and the PC software with the visualization approach for large images.

2 Macroscopic and microscopic friction

The Egyptians began investigating friction over 4000 years ago. However, written documentation on frictional force studies only began in the 15th century with the work of Leonardo Da Vinci. 200 years later, a French researcher named Guillaume Amontons rediscovered Da Vinci's observations.

Today, research on friction is increasingly oriented towards the microscopic scale. While tests on friction occur at the industrial scale, the underlying explanation for friction comes from the atomic scale.

2.1 Friction on the macroscopic scale

Leonardo Da Vinci was the first person to record experiments on friction. His experiments on rolling and static friction are shown in Fig. 2-1[10]. Da Vinci's research on friction resulted in two main findings: friction is independent of the apparent contact area and friction is proportional to the normal force.

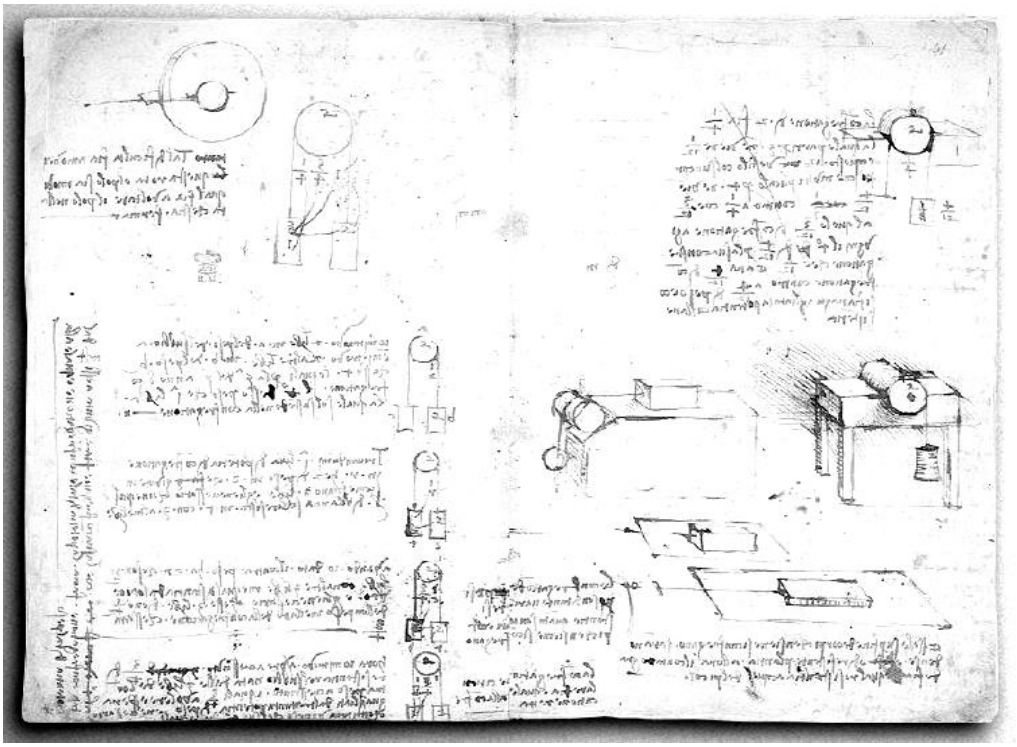

Fig. 2-1 The first documentation of experiments on friction

Approximately 200 years later and without knowledge of Da Vinci's experiments, G. Amontons and L. Euler reached the same conclusions as Da Vinci. They extended their findings to formulate the so-called law of Amontons and Euler: static friction is greater than dynamic friction.

Amontons conducted additional experiments using lard as a lubricant. C. A. Coulomb knew, reproduced and understood Amontons' work. He formulated a result that the dynamic friction is velocity-independent, which is known as Coulomb's law.

Morin reproduced Coulomb's work with many combinations of different materials, such as various types of wood, iron, brass, leather and ropes, as well as several lubricants such as talc,

soap, grease, oil, lard and water. Morin's work[11] produced the following results separating dry and lubricated friction:

The frictional force per unit area

- is proportional to the normal force for dry friction and independent of the normal force for lubricated friction
- depends on the roughness for dry friction and is independent of the roughness for lubricated friction
- is larger at the start of motion for dry friction and zero at the beginning of motion for lubricated friction

Microscopic techniques that are necessary to investigate frictional phenomena more closely are described in the following section.

2.2 Friction on the microscopic scale

The classical laws of friction, as described in the section above, may be used for a wide range of materials. However, it is difficult to derive these laws from fundamental atomic or molecular principles. Statistical mechanics was used in conjunction with thermodynamics to gain a better understanding of frictional phenomena. In the 1970's, surface roughness was ruled out as a possible mechanism for most types of friction: instead, friction was viewed as the bonding of atoms of two different materials that resist sliding when the materials are brought into contact[12]. Unfortunately, this "adhesive bonding" view of friction, due to Bowden and Tabor, does not predict the magnitude of the frictional force or the mechanism of energy dissipation. Tabor recognised that friction in the absence of wear (no tearing at the sliding interface) must have another loss mechanism. The elongation and tear of the bonding of atoms and molecules between interfaces is released in the form of atomic vibrations called phonons. G. A. Tomlinson first suggested the phenomena of phonons as a mechanism for friction in 1929. The following figure shows the basic Tomlinson model of friction:

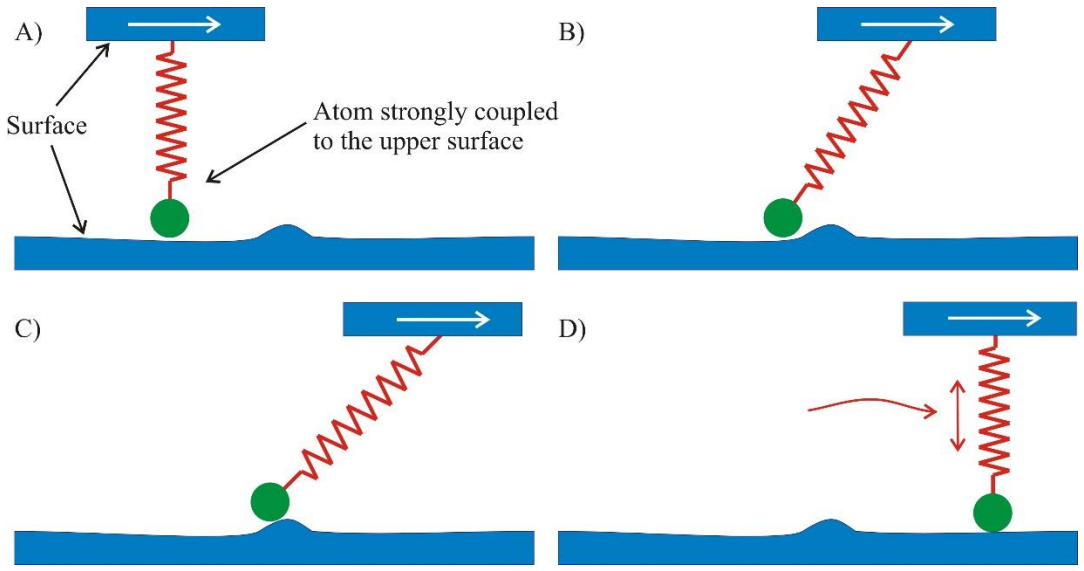

Fig. 2-2 Tomlinson model for a single atom

The single atom in Fig. 2-2 is strongly coupled to the upper surface. When the upper surface moves to the right, the atom slides over the lower surface. A time (position)-dependent force acts on the single atom during this relative motion between the two surfaces. The atom reaches

the potential hill where it sticks, increasing the applied force. The spring bends until the elastic energy stored in the spring is equal to the energy of the potential hill. The atom shoots back, releasing the spring. Phonons are generated from the energy transfer due to the spring oscillation to the upper surface. The model illustrated here is a good example for a single atom. However, a model that can be used in practical applications needs to account for the motion of multiple atoms: in SFM measurements, for example, the tip-sample region consists of a multitude of atoms.
This extension to multiple atoms is known as the Frenkel-Kontorova model. This model describes a harmonic chain of atoms that moves over a periodic potential, as shown in the following figure:

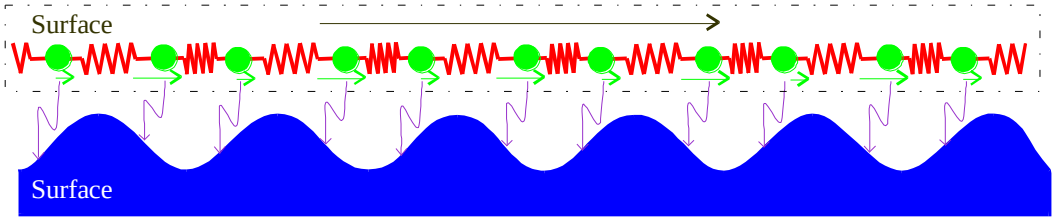

Fig. 2-3 The Frenkel-Kontorova model

Several chains of atoms interconnected by springs form a soft layer. When the upper layer moves with a constant velocity, a force proportional to the velocity damps every atom. With the damping of each single atom, a wave is emitted from each atom towards the lower surface. However, a model with a more rigid upper layer is needed to describe friction measurements by a scanning force microscope. The Frenkel-Kontorova-Tomlinson model combines the Tomlinson and Frenkel-Kontorova models.

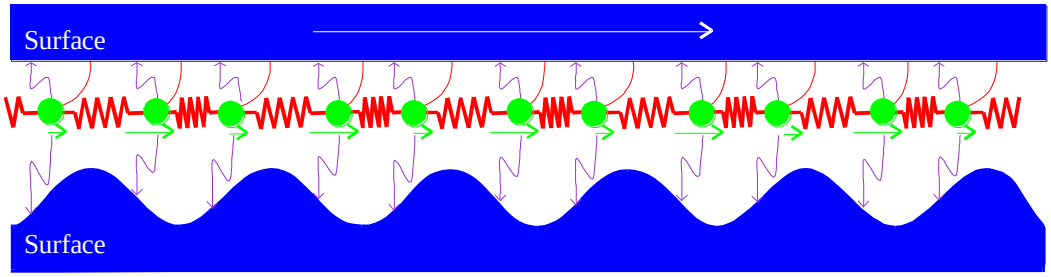

Fig. 2-4 The Frenkel-Kontorova-Tomlinson model

Fig. 2-4 shows the combined model. The difference between the models in Fig. 2-4 and Fig. 2-3 is that the atoms are now strongly bonded by leaf springs to the upper substrate. When the upper substrate moves at a constant velocity, the atoms are damped again. However, the phonons generated by the oscillations of each atom during the motion are now divided into a component that reaches the lower substrate and a component that reaches the upper substrate.
For application to the SFM, this short introduction to surface-surface contact mechanisms must be led over from a description of two flat surfaces to the tip-surface geometry. A short review of the different non-atomistic models is also given. The oldest but most often used theory is that for elastic spherical surfaces due to Hertz[13]. The theory describes the main relationships between pressure, contact radius and deformation for two spherical bodies as shown in Fig. 2-5.

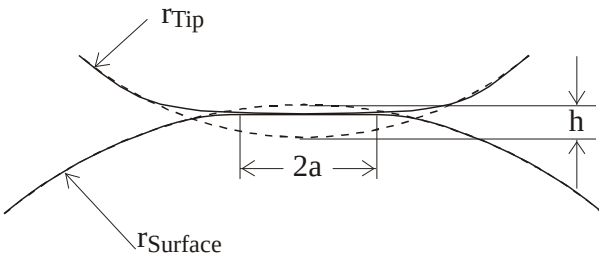

Fig. 2-5 Hertz model of tip-sample contact

Johnson-Kendall-Roberts (JKR) theory extends the Hertz model by including the surface energy and its influence on the properties of an elastic contact. The Hertz theory assumes that there are no attractive forces between the two surfaces in contact. Certainly, the effect of adhesion is observed in SFM experiments on force-distance curves or even as a snap-in effect during the approach of the cantilever. This effect leads to a finite tensile load that is required to separate the two surfaces (the pull-off force).
Another theory, known as the Deryaguin-Muller-Toporov (DMT) theory, is based on a Lennard-Jones (LJ) interatomic potential. Tabor showed that both theories are extreme limits of the same theory parameterized by the later on called Tabor parameter (λ_T)[14]. These values of λ_T correspond to stiffness, energy of adhesion and size of the interacting spheres. This model also accounts for forces acting outside the contact area.
The Maugis-Dugdale (MD) theory is used when the JKR and DMT theories are inadequate and the coefficient λ is approximately 1. The Maugis theory is the most comprehensive and accurate theory for a wide range of materials from large rigid spheres with high surface energies to small compliant bodies with low surface energies.
The Bradley theory describes the contact mechanism using a LJ potential, as in the DMT theory, but it focuses on two rigid spheres.
All these descriptions of the contact mechanisms for tribological contacts can be applied under the constraints shown in Fig. 2-6. The figure shows a schematic of all the theories in a force versus λ_T diagram, where λ_T is a dimensionless parameter given by:

$$\lambda = \frac{2.06}{z_0} \cdot \sqrt{\frac{R_s W_a^{\,2}}{\pi K^2}} \qquad \text{Eq. 2-1}$$

Here, z_0 is a characteristic atomic dimension, R_s is the reduced sphere radius, W_a is the work of adhesion at the contact and K is the effective Young's modulus.
λ_T is also proportional to the parameter μ_M introduced by Muller[15] with $\lambda_T = 0.4\ \mu_M$.

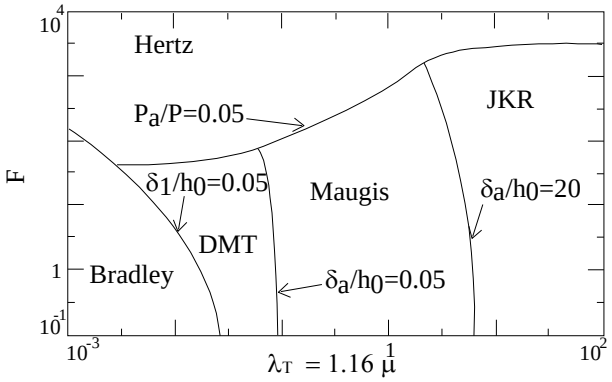

Fig. 2-6 Map of the elastic behaviour of bodies[16]

P_a/P is the ratio between the adhesive component of the load and the total load. For negligible adhesion, bodies fall in the Hertz regime (approximately $F > 10^3 \pi W_a R_s$). δ_1 is the elastic compression and h_0 is an equilibrium distance. When $\delta_1 << h_0$, bodies are rigid and follow the Bradley theory ($\lambda < 10^3$). δ_a is the adhesion-dependent deformation. For weak adhesion, the behaviour of materials is described by the DMT theory (approximately $10^{-2} < \lambda_T < 10^{-1}$). JKR theory predicts the behaviour of highly adhesive bodies (approximately $\lambda_T > 10^1$). The Maugis theory is used in the intermediate region (approximately $10^{-1} < \lambda_T < 10^1$)[17]. Almost independent of λ_T is the Maugis-Dugdale theory.

The use of these theories and their applicability for use with an SFM and possible measurement techniques are discussed in the next section.

3 Applicable modes for friction measurements

This section provides a brief overview of techniques for measuring friction forces using a SFM. Torsional deflection of cantilever is used to measure the lateral forces on probing tips. The vast majority of SFM use a four-quadrant photodiode (4Q-PD) to detect the deflection signal of the cantilever (see section 5.5 at page 5-56). The photodiode can separate the normal and the lateral components of the forces. This type of scanning force microscope, which is called a friction force microscope (FFM), can detect forces in the sub-nano-Newton regime. Mate first performed measurements[18] with the FFM and observed two important effects.

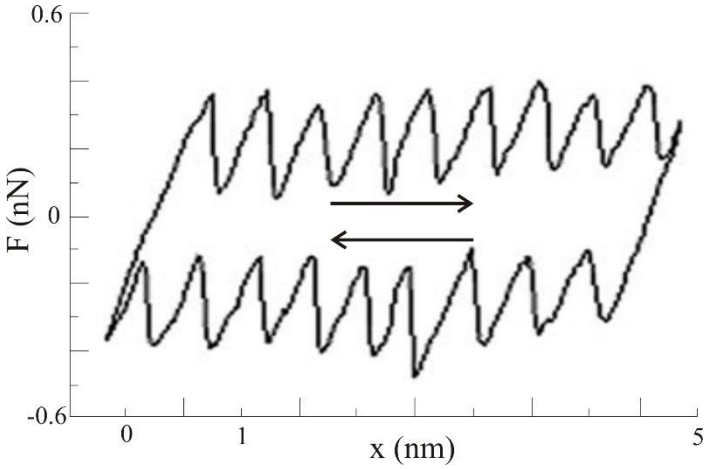

Fig. 3-1 Friction loop for NaCl in UHV[19]

The figure above shows these effects: one, a saw-tooth-shaped force curve resulting from a stick-slip phenomenon in the lateral force and second, hysteresis of the forward and backward scan, which is known as the friction loop.
Using the 4Q-PD to detect flexural deflection, which corresponds to the normal force, and torsional deflection, which corresponds to the lateral force. The first extension to the basic mode is the lateral motion of the cantilever or the sample, which is known as the lateral excitation mode[20]. The cantilever or sample is attached to a shear-force piezo that moves the cantilever or sample at a certain frequency.

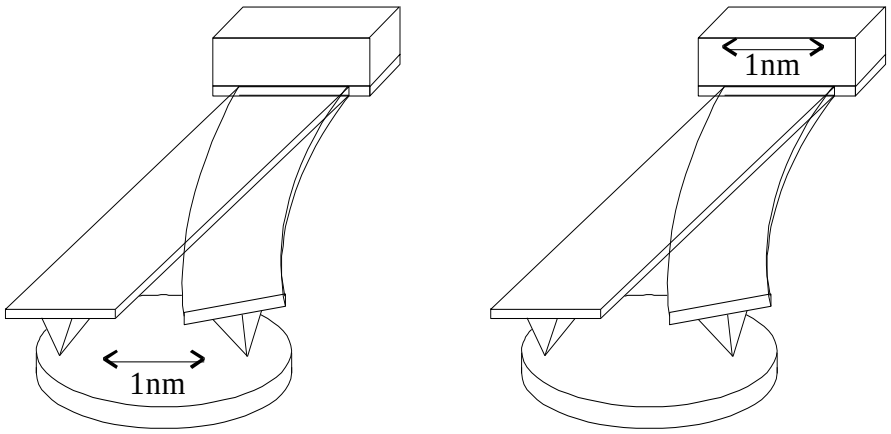

Fig. 3-2 Lateral force modulation of the sample (left) and the cantilever (right)

This lateral excitation, shown in the Fig. 3-2, can provide topography information on friction, lateral stiffness and viscosity[20]. The frequency can vary from a few kHz to several MHz depending on the mass of the moving sample or cantilever.

The torsional resonance mode provides information on lateral stiffness and viscosity. Fig. 3-3 (left) shows that the cantilever tip vibrates laterally (parallel) to the sample surface and remains close to the sample surface during the measurement, ensuring more intensive tip–sample interaction and providing more information on the surface and material properties.

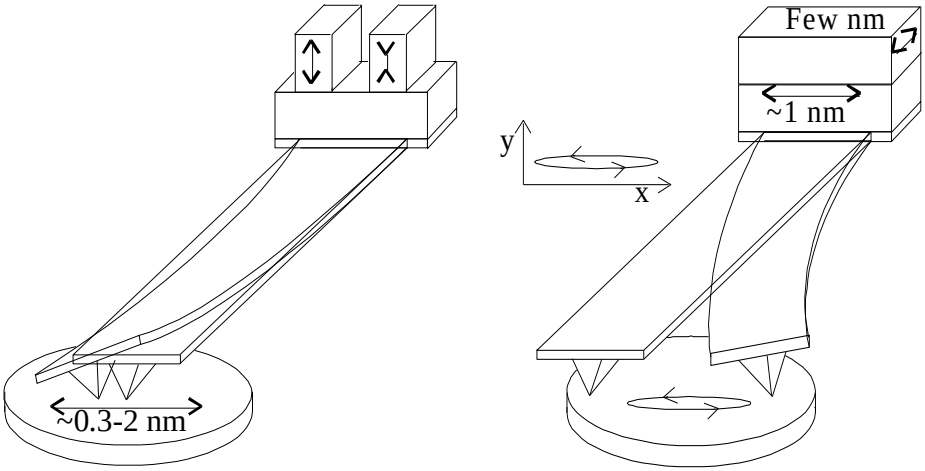

Fig. 3-3 Torsional resonance (left) and elliptical lateral force modulation (right)

Fig. 3-3 (right) is a new technique using a more or less elliptical lateral force modulation: the friction is measured at a single point without stick-slip phenomena at the reversal points. The elliptical trace of the vibrating cantilever results in a non-zero velocity for the tip-surface contact.

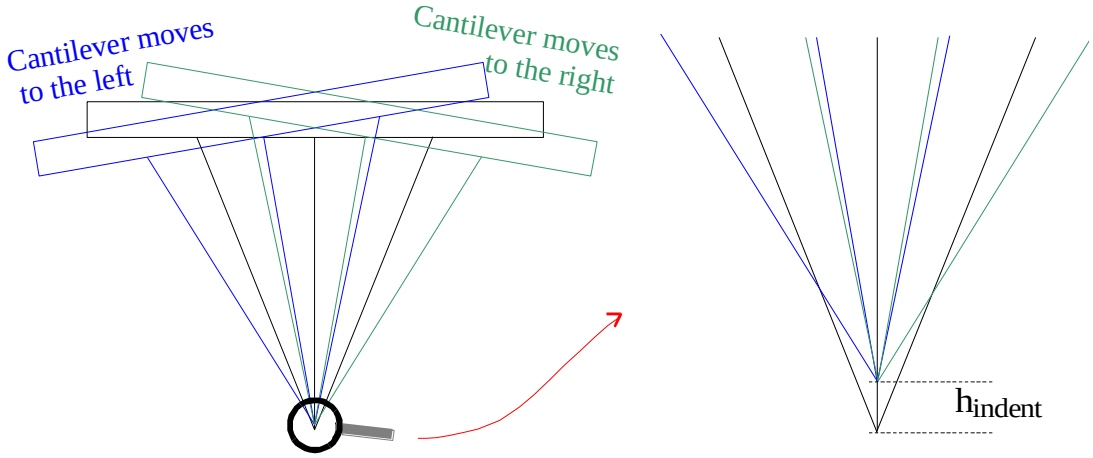

Fig. 3-4 Torsional bending of the cantilever(left) and the indentation variation (right)

In the dynamic friction mode, the cantilever dithers laterally over the sample, such that a turning point on each side is observable. Within this turning point, the cantilever is bent torsionally by the frictional force and is erected during the transition from one to the other side by a greater amount. The torsional lever amplification is several times larger than the normal lever amplification. Due to the torsional amplification, this erection results in an additional normal deflection error to the constant normal force on the sample (Fig. 3-4 [the torsion is exaggerated to provide a better view]), but can be removed as shown in the following scan modes.
Both scan modes use a lateral dither piezo and an additional z-piezo. The left image of Fig. 3-5 shows the motion of the cantilever in a pan-like shape. Before the cantilever reaches the turning

point on the left or right side, the z-piezo shrink, releasing the cantilever about a few nanometres. This reduces the normal force so that the cantilever can erect itself more easily without further indentation of the sample at the turning point as shown in Fig. 3-4 right side.

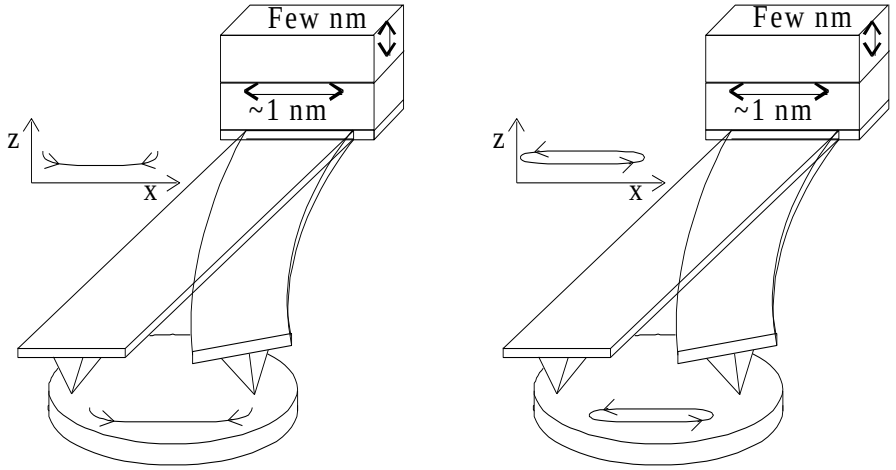

Fig. 3-5 Constant force and velocity dynamic friction mode with forward and backward dynamic friction (left) and with only one direction (right)

The velocity increases after the turning point and the cantilever is gently settled back to the original set-point.
The image on the right side uses the same cantilever motion but does not stop in the z-direction at the turning point. Instead, the cantilever moves further up and back to the other side to start the next loop after settling back onto the surface in the same direction as the previous lateral movement.
A sine/cosine-shaped voltage could generate such an x-z-movement. However, a sine/cosine voltage cannot be used for the piezos, because the velocity must be constant within each friction cycle. Dworak discusses this behaviour for the turning point during scanning force image acquisition[21].
Of course, the rounding of the turning point to a turning area is common. Fig. 7-3 (see page 7-75) shows this behaviour later in the manuscript for the scan area turning points and the optimisation of the scan area. However, a similar problem arises as for the frictional turning points at the end of the frictional loop. The results can be adapted to this lateral motion. Fig. 3-6 shows that the x-direction consists of a linear (light blue) zone where the friction occurs and an x-braking zone (red) where the cantilever is accelerated in the z-direction. In the x-acceleration zone (green), the z-motion is reduced to zero when the cantilever lateral velocity is linear. There is a ‘fly back’ zone (blue), followed by another x-braking zone (violet) and acceleration zone (olive); meanwhile, motion in the z-direction is accelerated and braked to begin the next frictional measurement.

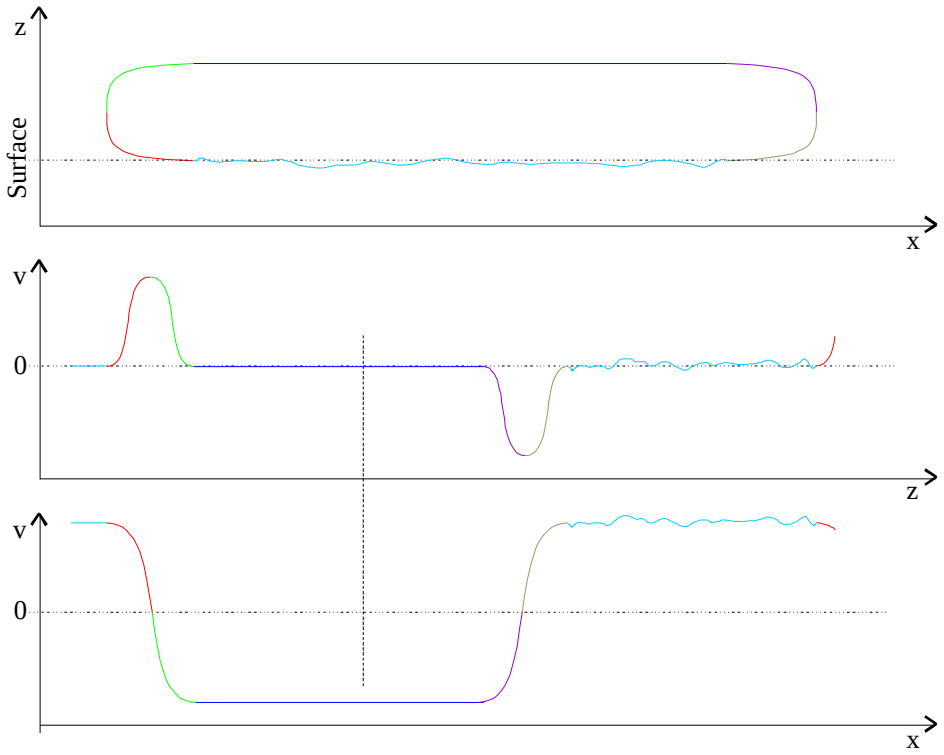

Fig. 3-6 The x- and z-motion and separated velocities in the x- and z-direction

As mentioned above, there are actually several measuring points within one loop of the cantilever (see Fig. 3-7, left image) at high sample rates. This result enables closer examination of each friction loop. It is conceivable that the scan could be stopped so that the loop could be traversed several times, to sample each position multiple times to reduce the noise for the loop. This force-distance-curve mapping technique can be thus used to map the friction loop.
The direction of the loop can also be changed by a turn in the scan direction. Thus, it may be possible to visualise the results of the friction measurements in both scan directions (see Fig. 3-7, right image).

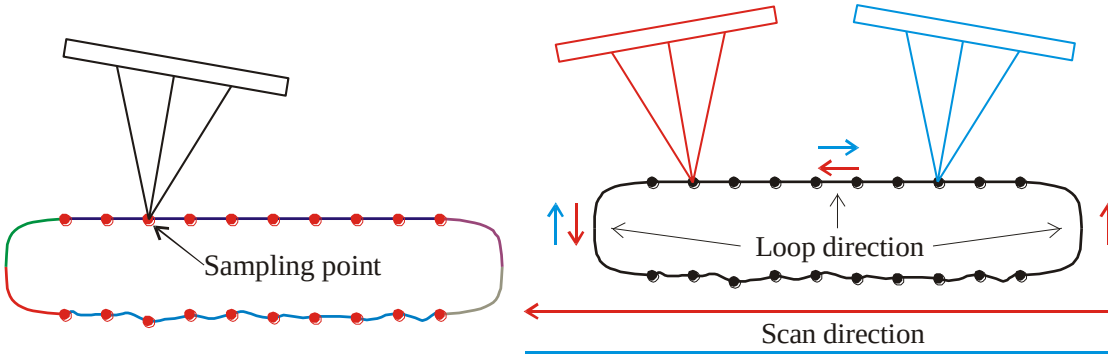

Fig. 3-7 Visualisation of the sampling points (left) and the direction of motion of the scan and the loop (right)

Oversampling facilitates the measurement of several data points during the friction measurement. Data measured during the ‘non-contact’ backward motion can be subtracted from data measured during the contact motion of the tip to eliminate different types of measurement errors.
So far, the loop direction has been opposite to the scan direction so that the velocities of cantilever and sample must be added together. However, if the loop has the same direction as the

scan during the contact phase, the velocities should be subtracted from each other. Therefore, the scan speed is higher in comparison with the friction speed. This results in a high imaging speed, with less friction speed to provide sufficient time to observe large samples. The friction velocity during the scan can vary from zero (when the scan and the loop have the same velocity) to ‘static’ behaviour (when the loop is off) to higher velocities (when the velocities of the loop and the scan are in the same direction).

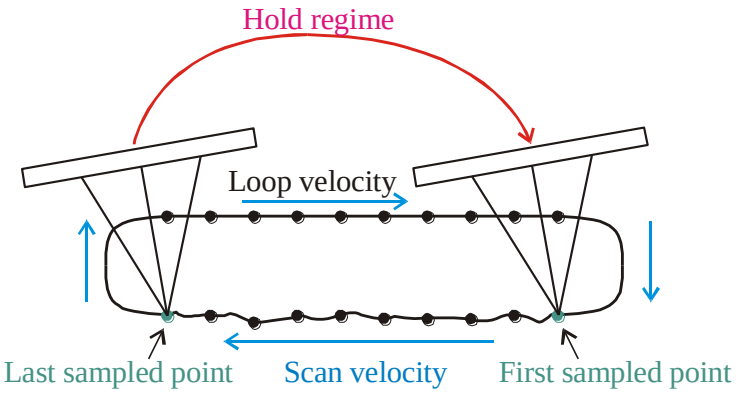

Fig. 3-8 Sample-and-hold feedback for slow loop measurements

This measurement technique can close the gap between the ‘static’ friction and the high frequency dynamic friction regimes. A sample-and-hold circuit has been implemented into the scanning force microscope system introduced here. This circuit is used when the frequency of the loop cycles are in the range of the bandwidth of the feedback loop.
The feedback system measures and reacts to the z-motion of the cantilever loop. To suspend this behaviour during the lift-off phase of the loop, the feedback system is switched to a hold state until the cantilever is in the contact regime: the feedback system is then released to measure actual data again. The sample-and-hold circuit has its limits. If the scan velocity increases to high values when the loop frequency is low, the path of motion of the sample increases during one loop. Therefore, the distance between the last sampled point of the actual loop and the initial sampled point of the following loop (Fig. 3-8) increases to unacceptable values.
All the lateral vibration modes introduced here relate to samples and/or a cantilever setup that can be heated. This list of techniques presented here is not meant to be comprehensive and only serves as an overview of commonly used techniques. These accepted techniques and the newly introduced techniques are implemented for the novel scanning force microscope presented here.

4 Construction of the cantilever holder and sample holder for temperature-controlled experiments on friction

The novel scanning force microscope is designed to use a scan area up to 1000 µm times 1000 µm with separate heatable stages for the cantilever and the sample.
The following figure shows vertical sections of the entire microscope, revealing the setup and locations of the cantilever and sample holders.

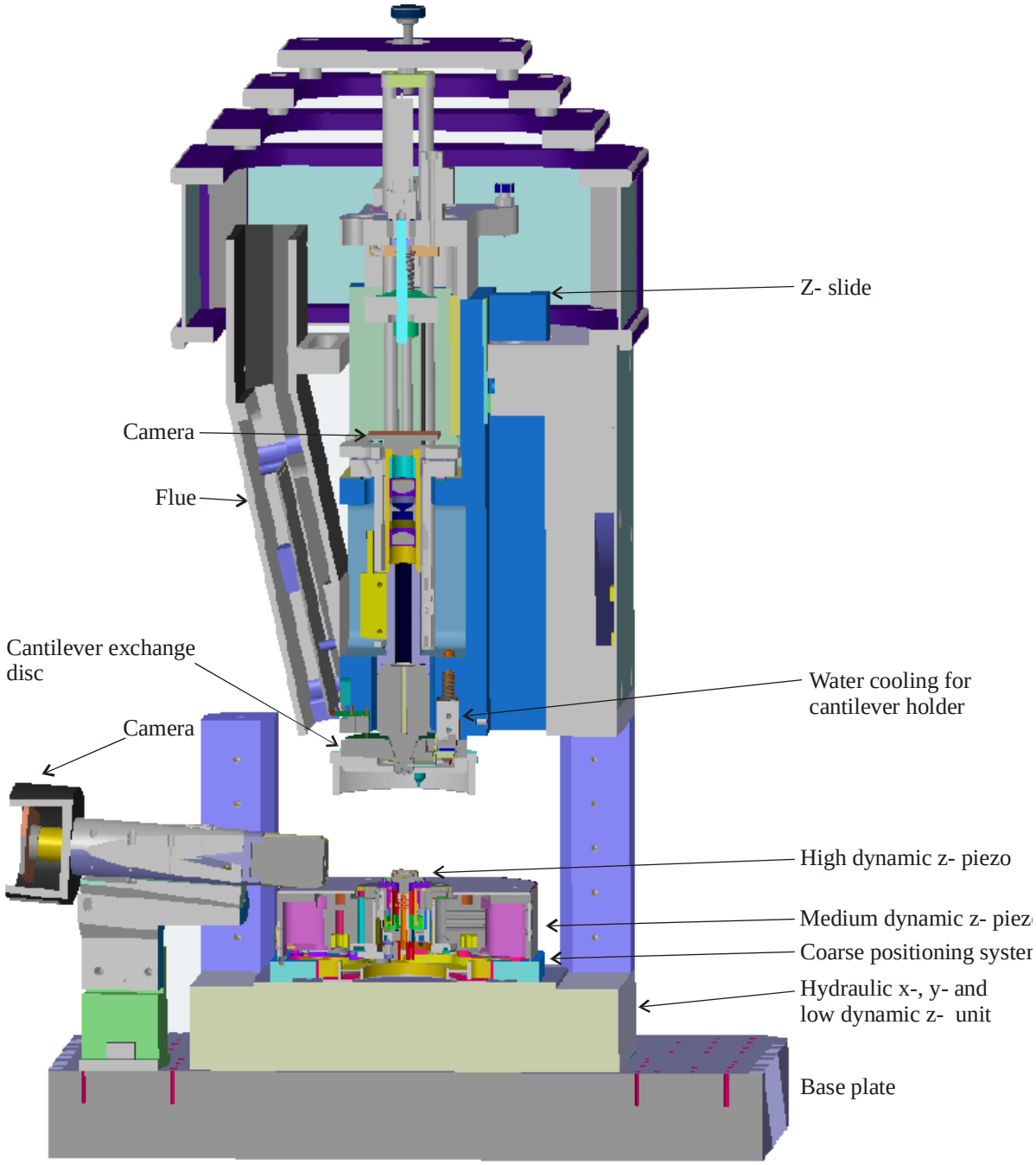

Fig. 4-1 The novel scanning force microscope (vertical section)

Two components of the complete system are discussed in the following section: first, the entire cantilever holder disc, with its heat and cooling system, and second, the mid-range and high frequency range Z-piezo drive within which the sample holder setup is implemented.

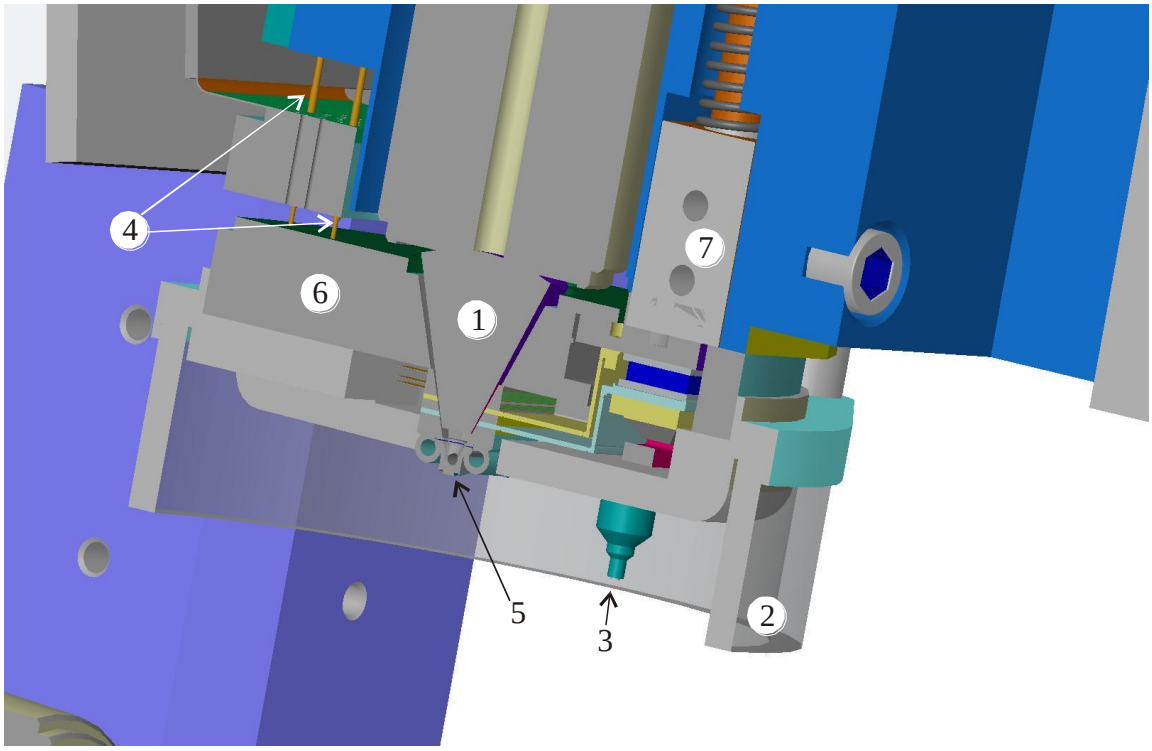

Fig. 4-2 The cantilever holder setup [markers 1 to 7]

Fig. 4-2 and Fig. 4-3 show the cantilever holder disc inserted into the SFM system. Each figure shows the disc from a different angle.
Marker 1 shows the ULE (ultra low expansion) glass body that is used to combine the sample view from the normal incidence camera and the entrance of the light beam to the cantilever deflection system. The use of the glass body is described in more detail in section 5.2. (Beam guidance in the prism is described on page 5-52).
Marker 2 is the quartz glass chamber. The chamber protects the cantilever and the sample from the surroundings. The chamber avoids airflow and acoustic coupling and minimises thermal convection by covering the heated sample and/or cantilever. Two feedthroughs change the gas or gas composition inside the chamber during the scan.
The 3rd marker indicates one of three actual fibre-based distance control sensors. These sensors detect the fast approach of the cantilever. The sensors and their modes of operation are discussed in more detail in section 6.3 (page 6-69). The sensors have a linear distance control area of approximately 500 µm to observe the entire z-displacement range of the SFM. The sensors can also detect the temperature to control and compensate the dilatation during dynamic temperature experiments[22].
Electrical contact is established through gold spring contact pins marked with a "4". These contacts are for the cantilever holder ground-connection and for connecting the cantilever with an AC or DC voltage supply or for current measurements. The contacts also supply the shear and oscillator piezos, the resistive heater and the temperature sensor of the cantilever. A few pairs of contact pins are left free for other experimental measurements on humidity control, for example.
The cantilever holder with the cantilever, tagged with number "5", is plugged into a receptacle with circular springs on either side. Most of the milled parts of the microscope are made from an aluminium alloy with a tensile strength of 400 to 600 $^{N}/_{mm^2}$. The aluminium alloy cannot be used in the receptacle because the alloy loses its tensile strength above a temperature of 100°C. Titanium alloys show similar mechanical behaviour but lose their tensile strength at temperatures higher than 400°C. A more detailed discussion is given in the following section.

To change the cantilever, the Z-slide is lifted up followed by releasing the quartz glass chamber (2) downward. Three chuck cones fix the cantilever holder disc (labelled with 6) to the z-slide. Unfastening the cones allows the disc, with the optical glass body (1) and cantilever holder (5), to be removed from the system. The cantilever holder can then be removed from the disc and the cantilever can be changed. The entire disc can also be connected to a "dummy" stage so that additional tools, such as an optical microscope, can be used to precisely adjust the new cantilever.

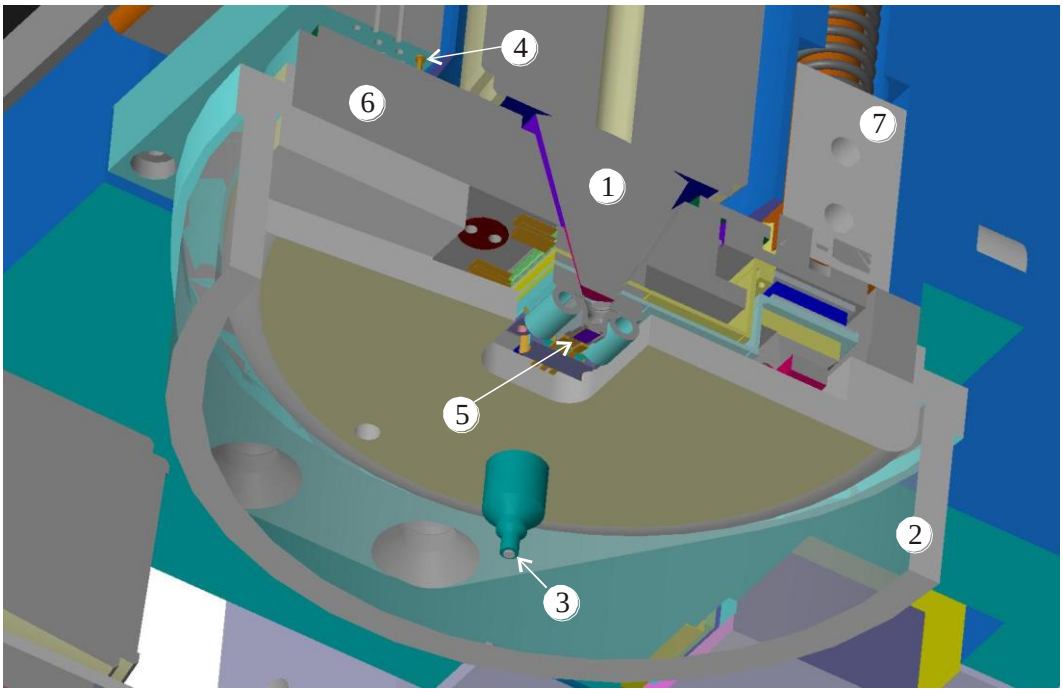

Fig. 4-3 The cantilever holder setup (viewed from below) [markers 1 to 7]

Marker 7 shows the water cooling system for the cantilever holder disc. The water-cooling block is thermally connected to the dither piezo stack. The cantilever is connected over a thermoelectric cooling (Peltier) system that helps to transfer the thermal load to the water-cooling block.
The sample holder is reviewed next. The sample holder is thermally insulated, like the cantilever holder, to protect the piezo against thermal destruction and the system against thermal drift. For completeness, marker 8 shows the object lens of the second camera, which views the sample at an angle of approximately 10°. The hydraulic X-, Y-, Z-table is shown by marker 9. This table carries a piezo walker X-, Y-table, shown by marker 10, which enables the 'coarse' positioning of the sample with a ±2.5 mm stroke in the x- and y-directions.
The system has three separate Z-scanners, which are stacked on top of each other: one for low frequencies, one for mid-range frequencies and one for the high frequency regime. The frequency response of each of the three drives enables the drive with the higher resonance frequency to excite the drive below with the lower resonance frequency into an oscillation. The feedback parameters can damp the oscillations but cannot completely suppress the behaviour. The problem is better solved by reducing the stimulus. Marker 11 in Fig. 4-4, which is more easily observed in Fig. 4-6, shows a mass ring that compensates for the forces of the dynamic motion. The mid-range frequency piezo uses six piezo stacks to move the high frequency Z-drive and the sample holder, and to compensate for the force during dynamic motion additional 6 piezos of the same size to move the compensatory mass in the opposite direction. The mass is calculated to compensate for the entire holder, the high frequency Z-drive with its sample holder and the sample holder with a massive sample.

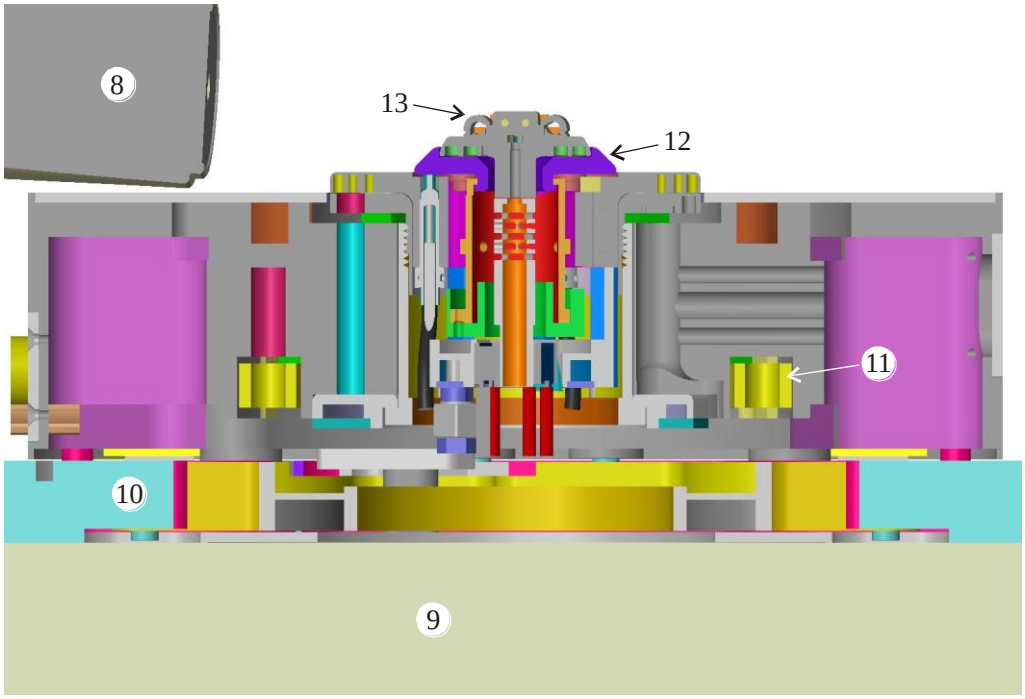

Fig. 4-4 The sample holder setup (overview) [markers 9 to 13]

The compensation piezos can be adjusted to move slightly less than the piezos that move the sample, if the sample is lighter than that calculated. The same piezos are used for the sample motion and the compensatory motion, thus allowing the sample and the mass to move the same distance in opposite directions. As the piezos show nonlinear behaviour, it is essential to use the same piezos (not e.g. half-size piezo with double mass) to achieve the best compensation.

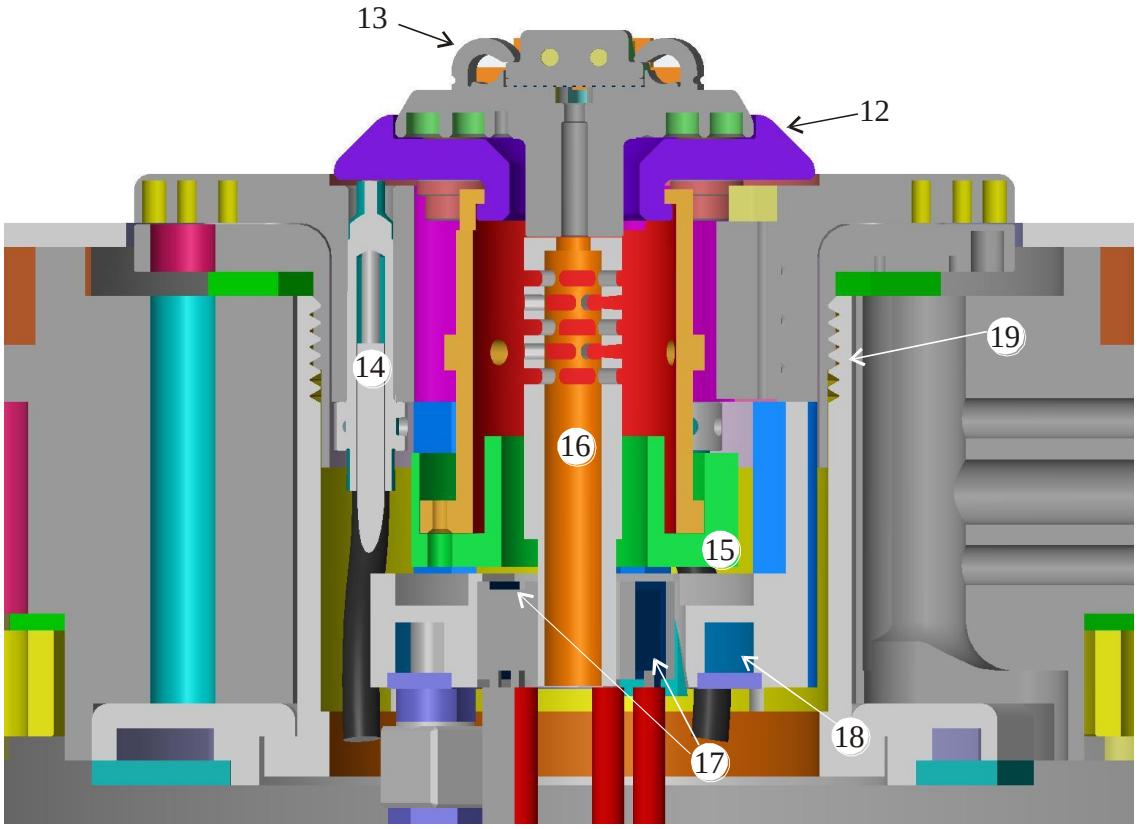

Fig. 4-5 Detailed sample holder setup [markers 12 to 19]

The piezos must be pre-loaded because they are only stable under compressive stress. Marker 19 shows the pre-loaded spring for the mid-range frequency Z-drive piezos. The spring is made of copper beryllium and laser-structured with a meander structure (not shown in the figures) to minimise changes in the pre-loading due to variations in length of the piezos.
Marker 12 shows a thermally isolated body that thermally separates the high from the mid-range frequency Z-drive. This disc is made of Zerodur® (Schott AG, Mainz, Germany), a glass ceramic with a low thermal conductivity of $1.46 {}^{W}/_{(m*K)}$ and a small coefficient of expansion of approximately $0.05*10^{-6}$ K^{-1}.
Marker 13 shows the high frequency Z-drive with the sample holder. As mentioned previously in the context of the cantilever holder receptacle, most of the milled parts of this microscope are made of an aluminium alloy with a tensile strength of 400 to 600 ${}^{N}/_{mm^2}$. Due to the better tensile strength stability by higher temperature, this part is made of titanium. Titanium's different density is compensated for by milling grooves in the backside of the sample holder, leaving only small bars for stability.
Three fibre sensors (marker 14) control the motion of the high frequency Z- drive, with one fibre controlling each piezo. This control guarantees precise z-motion without tilting the sample. Fibre optical sensors (not shown in the figures for clarity) also control the mid-range frequency Z-drive. Therefore, the high frequency Z-drive and the mid-range frequency Z-drive are so called close-loop scanner.
The high frequency Z-drive also has force compensation. The force compensation mass is shown by marker 15. The same principle is used as for the mid-range frequency Z-drive. The mass is calculated to compensate for the movable parts of this drive and the sample. These piezos are adjustable to within a few per cent of the stroke to adapt the compensation mass to the sample mass.

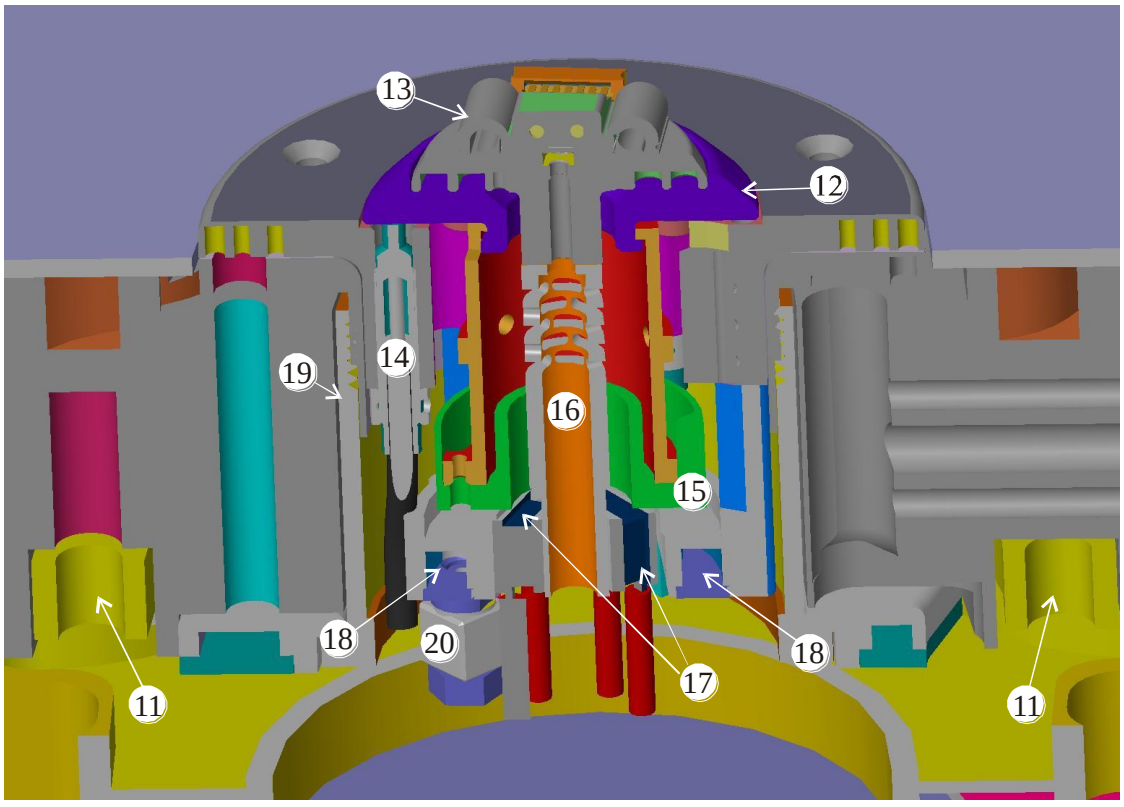

Fig. 4-6 The sample holder setup (tilted) [markers 11 to 20]

Marker 16 shows a copper beryllium spring. This spring pre-loads the high frequency Z-drive. The spring also serves as a thermal conductor to cool the sample holder and the sample within it. The system must be actively cooled if a dynamical thermal experiment is performed or if the sample is heated to a high temperature. At the bottom of the spring, three thermoelectric cooling elements, marked with 17, are used to increase the thermal gradient. An additional water-cooling system is used as a heat sink. A capped trench, marked by 18, is separated into two channels, whereby half the water can flow to the left and half the water can flow to the right, to improve temperature equilibration under flow. This water cools the spring holder and the spring via the thermoelectric cooling elements. Marker 20 shows the throughput for the water. The discharge for the water cooling system is located on the right side of the system but is not shown in the figure.
This concludes the brief introduction of the main components of the cantilever holder and the sample holder, the position of these components within the microscope, as well as temperature management and the influence of temperature on the different components of the microscope system. A more detailed analysis of the cantilever holder, the sample holder and temperature management follows.

4.1 The cantilever receptacle and holder setup

The cantilever receptacle is a stack of piezos, ceramic isolation plates and active temperature control elements. Fig. 4-7 shows the setup for the stack.

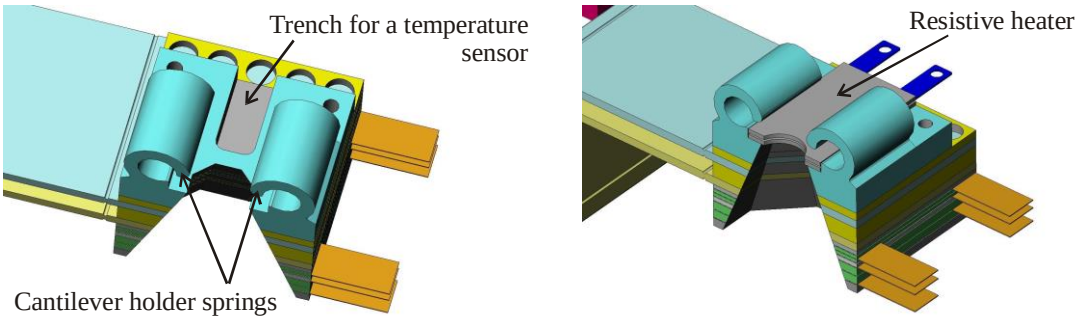

Fig. 4-7 The receptacle without the cantilever holder and contact clamps (left), and with the resistive heater (right)

The trench where the temperature sensor (PT100) is located is shown on the left-hand side of the figure above. This sensor is glued to the resistive heater. The heater is seen in the right-hand side of the figure above and covers the temperature sensor, which only contacts the heater via the glue. The glue has a thermal conductivity of $7.5^{W}/_{m*K}$.

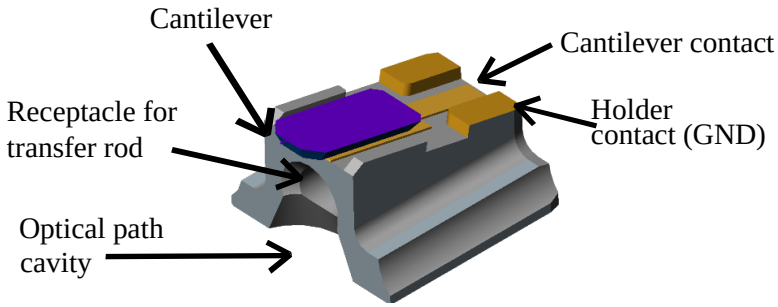

Fig. 4-8 The cantilever holder and the cantilever

Different cantilever holders are needed for different measurement modes. The holder shown in Fig. 4-8 has two ground contacts to give the holder a defined potential and a third contact, which is insulated against the holder and where the cantilever is glued on. This contact can be used to measure current or to apply a given potential to the cantilever.

4.2 Independent temperature control of the cantilever

The microscope has a separate feedback system for the temperature control of the cantilever. In the present setup, the temperature sensor for thermal feedback is located beneath the resistive heater. Temperature control systems suffer from time–delays in sensor feedback due to the thermal capacitance of the materials that conduct thermal energy.
Investigating the thermal dynamics of the cantilever temperature system provides an estimate of the possible range of temperature variations. Such calculations provide information on the temperature and the temperature variations of the cantilever bar, but not on the thermal energy transferred to the sample.

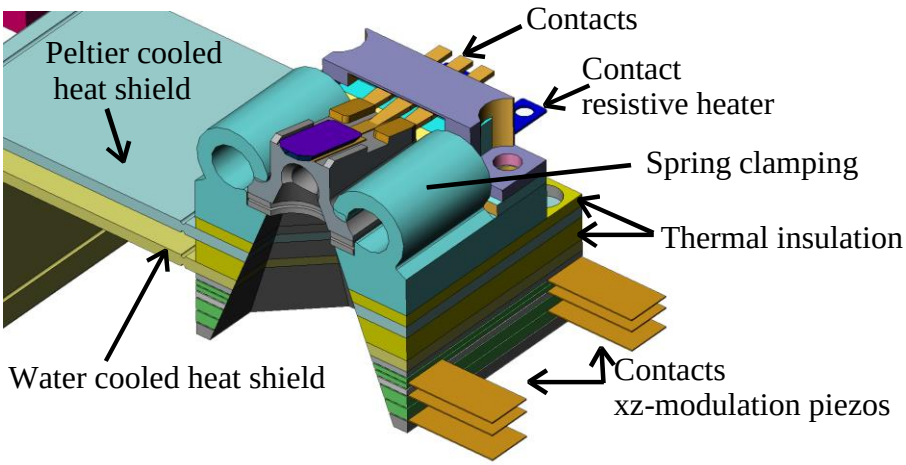

Fig. 4-9 The cantilever holder within the receptacle unit

The following figure provides a detailed frontal view of the complete setup of the cantilever holder stack, along with the different materials used.

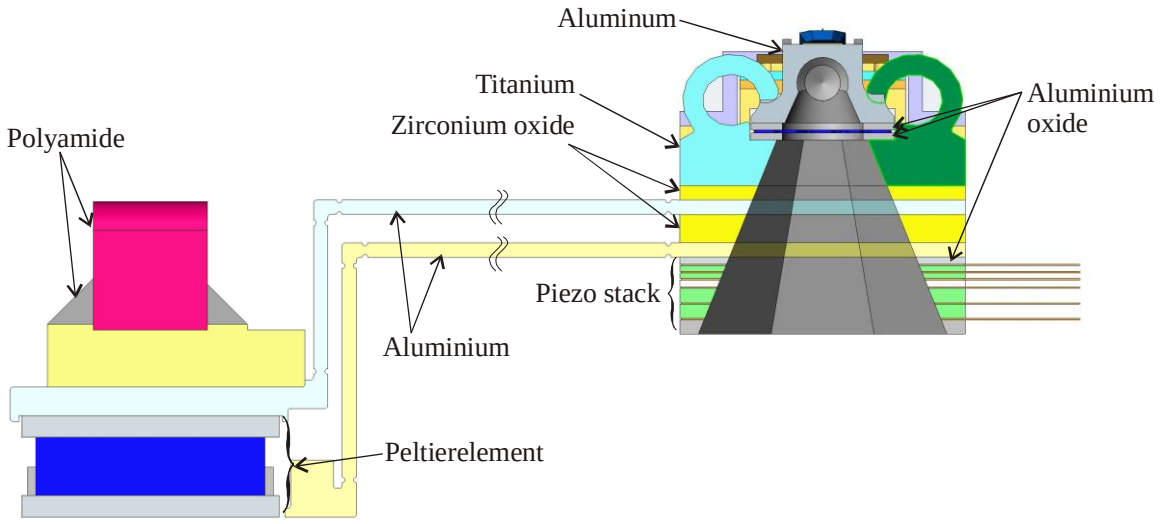

Fig. 4-10 Frontal view of the cantilever receptacle thermal setup with the specific materials used

First, the thermal losses from thermal radiation and convection are calculated.

The calculation of thermal radiation is the calculation of the amount of energy, which is exchanged by radiation between one body and its environment. Calculating the thermal radiation is complicated by the complex geometries and irradiation characteristics of the bodies under consideration. The medium between the bodies can also be involved in absorption and emission. Thus, the geometry must be simplified to obtain a practical solution.
Each body with a temperature higher than absolute zero emits heat radiation. The radiation power is calculated using the Stefan-Boltzmann-Law as follows:

$$P_r = \sigma \cdot A \cdot T^4 \qquad \text{Eq. 4-1}$$

where A denotes the surface area, T denotes the temperature and the Boltzmann constant σ equals 5.67 10^{-8} $^{W}/_{m^2K^4}$. However, the Stefan-Boltzmann-Law is only valid for black body radiation. For non-black-body radiation, a modification of the equation is necessary. A black body has an emission coefficient ε = 1. For non-black bodies, this coefficient is less than 1. In the present case, isotropic radiation of a so-called grey body or Grey Lambert Emitter is assumed. Therefore, the Stefan-Boltzmann-Equation is modified to[23]:

$$P_r = \varepsilon \cdot \sigma \cdot A \cdot T^4 \qquad \text{Eq. 4-2}$$

A further condition is that the bodies of interest in the given microscope setup are covered by other bodies which are also physically grey bodies. This means that the body, which covers the first body, also has a temperature higher than absolute zero and that the radiation can be calculated as:

$$P_r = E \cdot \sigma \cdot A \cdot (T_1^4 - T_2^4) \qquad \text{Eq. 4-3}$$

Here, the emission coefficient ε is replaced by the radiation exchange grade E, which is given by[23]

$$E_x = \frac{1}{\frac{1}{\varepsilon_1} + \frac{A_1}{A_2}\left(\frac{1}{\varepsilon_2} - 1\right)} \qquad \text{Eq. 4-4}$$

The radiation exchange grade E_x results from the geometric series of the radiation from one body, partial absorption by the second body, the partial reflection of the radiation from the second body back to the emitting body and so on. For a first estimate, a static temperature maximum of 150 K above the ambient temperature for the cantilever holder and 25°C for the covering body is assumed. The sizes of the different surfaces of the microscope can be taken from the mechanical construction software SolidWorks®.
The equation above can be reduced using the following conditions for the given setup. The relative proportions of the surface areas of the two bodies affect the emission coefficient of the second body. The surface area of the emitting body is several times smaller than the second body in the setup described here. The emission coefficient of the second body, which is black-coated-aluminium, is approximately 0.9. Therefore, E_x is equal to ε_1 to a good approximation.
The maximum radiation of the system is reached if the temperature of all the parts is 150 K above the ambient temperature. In this case, a sum over all the surfaces multiplied by the individual emission coefficient results in the following equation:

$$P_r = \sigma \cdot \begin{bmatrix} \left(\varepsilon_{Cantilever} \cdot A_{Cantilever}\right) + \left(\varepsilon_{Titaniumhodder} \cdot A_{Titaniumhodder}\right) + \ \cdots \\ + \left(\varepsilon_{Polyamide} \cdot A_{Polyamide}\right) \end{bmatrix} \cdot \left(T_1^4 - T_2^4\right) \qquad \text{Eq. 4-5}$$

Using the values from Tab. 4-1 in Eq. 4-5 results in a thermal power loss of approximately 10 mW through thermal radiation, assuming that all the parts of the cantilever holder are heated to 150 K (T_1 = 175°C) in an environment at T_2 = 25°C.

	Specific heat capacity	Specific heat conductivity λ	Emission coefficient ε [1]	Surface size (with air contact)	Volume
Cantilever (native oxide)	700.0 $^{J}/_{kg*K}$	130 $^{W}/_{m*K}$	0.83	7,4 mm²	1.3 mm³
Aluminium Cantilever holder (native oxide)	930.0 $^{J}/_{kg*K}$	239.0 $^{W}/_{m*K}$	0.25	57.9 mm²	36.9 mm³
Aluminium To Peltier-Element (native oxide)	930.0 $^{J}/_{kg*K}$	239.0 $^{W}/_{m*K}$	0.25	400.1 mm²	159.7 mm³
Aluminium To Water-Cooler (native oxide)	930.0 $^{J}/_{kg*K}$	239.0 $^{W}/_{m*K}$	0.25	248.8 mm²	231.6 mm³
Titanium Holder receptacle (native oxide)	520.0 $^{J}/_{kg*K}$	21.9 $^{W}/_{m*K}$	0.4	122.1 mm²	118.8 mm³
Zirconium oxide 0.5 mm	460.0 $^{J}/_{kg*K}$	2.1 $^{W}/_{m*K}$	0.8	17.7 mm²	45.4 mm³
Zirconium oxide 1.0 mm	460.0 $^{J}/_{kg*K}$	2.1 $^{W}/_{m*K}$	0.8	33.8 mm²	86.3 mm³
Aluminium oxide Piezo top cover	950.0 $^{J}/_{kg*K}$	24.5 $^{W}/_{m*K}$	0.3	6.8 mm²	18.4 mm³
Polyamide Pressing block of Peltier-Element	1700.0 $^{J}/_{kg*K}$	0.25 $^{W}/_{m*K}$	0.9	98.6 mm²	123.0 mm³

[1] The emission coefficient is given at infrared wavelengths

Tab. 4-1 Characteristics of the different materials used

The second thermal loss is due to convection. The convection in the system considered here is passive and can be calculated as follows:

$$P_{conv} = \alpha_{conv} \cdot A_{eff} \cdot (T_{body} - T_{env}) \qquad \text{Eq. 4-6}$$

where T_{body} is the temperature of the individual body, A_{eff} is the effective surface area that is involved in the convection process, T_{env} is the ambient temperature and α_{conv} is the convection coefficient of the specific body. The calculation of α_{conv} is complex because many parameters

have an influence on the heat transmission coefficient. However, one possible approximation for α_{conv} due to natural convection is given by[24,25]

$$\alpha_{conv} = 1.42 \cdot \sqrt[4]{\frac{T_{body} - T_{env}}{l_{conv}}} \qquad \left[\frac{W}{m^2 K}\right] \qquad \text{Eq. 4-7}$$

The convection coefficient is calculated by the fourth root of the temperature difference divided by the effective length of the airflow contact with the body. The equation for the complete cantilever stack is

$$P_{conv} = 1.42 \cdot \left(\left(\frac{A_{eff}}{\sqrt[4]{l_{conv}}} \right)_{Cantilever} + \left(\frac{A_{eff}}{\sqrt[4]{l_{conv}}} \right)_{Titanholder} + \ldots + \left(\frac{A_{eff}}{\sqrt[4]{l_{conv}}} \right)_{Polyamide} \right) \cdot \left(T_{body} - T_{env}\right)^{5/4} \qquad \text{Eq. 4-8}$$

Natural convection is only possible if the body walls are approximately vertical. The following table shows the calculated values for the effective surface sizes and the effective convection lengths (calculated using the mechanical construction software SolidWorks®) of the different materials used in the actual setup.

	Effective Surface size	Effective convection length
Cantilever (native oxide)	2.7 mm²	8.6 mm
Aluminium Cantilever holder (native oxide)	6.7 mm² 4.3 mm²	2.7 mm 2.0 mm
Aluminium To Peltier-Element (native oxide)	19.5 mm² 10.1 mm² 10.8 mm²	0.5 mm 1.0 mm 10.7 mm
Aluminium To Water-Cooler (native oxide)	19.2 mm² 10.8 mm² 5.7 mm²	0.5 mm 10.7 mm 2.0 mm
Titanium Holder receptacle (native oxide)	63.6 mm²	1.6 mm

	Effective Surface size	Effective convection length
Zirconium oxide 0.5 mm	20 mm²	0.5 mm
Zirconium oxide 1.0 mm	40 mm²	1.0 mm
Aluminium oxide Piezo top cover	10 mm²	0.25 mm
Polyamide Pressing block for Peltier-Element	74.8 mm² 52.8 mm²	2.2 mm 1.8 mm

Tab. 4-2 Effective surface sizes and heights of the different system components used in the calculation of convection losses for the setup

Convection losses can be calculated using the values from Tab. 4-2 in Eq. 4-8. The overall convection loss is about one watt. This calculation ignores the fact that the air flowing up around the stack (see the stack on the right side of Fig. 4-10) has a higher temperature at the top of the stack than at the base of the stack. Therefore, this calculation corresponds to a worst-case scenario. Comparing both the previously discussed loss routes show that thermal radiation has nearly no effect in the temperature range considered for this system. Therefore, convection should be monitored for the system.

The heat conduction in the system will be calculated next. Heat conduction is more interesting to calculate because it indicates how fast the temperature of the cantilever can be changed. On the other hand, the heat conduction can be regarded just as an additional loss route. For example, the wires of the resistive heater conduct some of the heat away from the heater. The resistive heater is connected to a transfer circuit board, which is connected via spring-loaded pins to the microscope. It is assumed that the board is at the ambient temperature of 25°C. 40 mm long copper wires with AWG 27 connect the heater and the board. Copper has a specific heat conductivity of 360 $^{W}/_{m*K}$. To reach a temperature at the cantilever chip that is 150 K higher than the ambient temperature in an adequate time, the heater must use a higher temperature to generate the necessary gradient.
The Fourier law of heat conduction can be used to calculate the thermal power transferred. The heat flux from Fourier's law is calculated by

$$Q = \lambda \cdot \frac{A}{l} \cdot t \cdot \Delta T \quad \rightarrow \quad Q = \lambda \cdot \frac{A}{l} \cdot t \cdot (T_1 - T_2) \qquad \text{Eq. 4-9}$$

Eq. 4-9 can be written in terms of $^{Q}/_{t}$ as follows:

$$\frac{Q}{t} = \lambda_{cond} \cdot \frac{A}{l_{cond}} \cdot (T_1 - T_2) \qquad \text{Eq. 4-10}$$

where $^{Q}/_{t}$ is the amount of heat transferred per unit time.
Assuming a maximum heater temperature of 200 K above the ambient temperature and using the values discussed above in Eq. 4-11, a loss of 0.56 W via the wires is calculated.
This static estimation produces an overall loss of approximately 1.6 W for the maximum temperature of the cantilever holder setup.
Following this static temperature estimation for the setup, a dynamic estimation of the heater performance will be made.
To produce a solvable equation, the following assumption is made about the square base stack where the resistive heater is located: the thermal conductivity of the metals used is high compared with the estimated temperature gradients so that the temperature distribution in the materials can be assumed to be homogeneous.
Attention should be paid to the several connections between the different materials and the thermal capacity of the materials. The heat capacity of the materials must be used in calculating the dynamic thermal behaviour of the cantilever holder. The heat capacity is given by

$$C_h = \frac{Q}{T} \quad \rightarrow \quad Q = C_h \cdot T \qquad \text{Eq. 4-11}$$

where C_h is the thermal capacity. Combining the time-dependent Eq. 4-10 and Eq. 4-11 yields

$$\frac{Q}{t} = C_h \cdot \frac{dT}{dt} = \frac{\lambda_{cond}}{l_{cond}} \cdot A \cdot (T_1 - T_2) \qquad \text{Eq. 4-12}$$

The heat transferred per unit time may be expressed as follows:

$$I_{hf} = \frac{Q}{t} \qquad \text{Eq. 4-13}$$

Eq. 4-12 may be re-written using the previously stated assumption that the temperature is equal over the entire region between the two bodies:

$$C_h \cdot \frac{dT}{dt} + \frac{\lambda_{cond}}{l_{cond}} \cdot A \cdot T_2 - \frac{\lambda_{cond}}{l_{cond}} \cdot A \cdot T_1 = 0 \qquad \text{Eq. 4-14}$$

Dividing the equation through by the factor C_h produces

$$\frac{dT}{dt} + \frac{\lambda_{cond} \cdot A}{l_{cond} \cdot C_h} \cdot T_2 - \frac{\lambda_{cond} \cdot A}{l_{cond} \cdot C_h} \cdot T_1 = 0 \qquad \text{Eq. 4-15}$$

This equation resembles the mathematical description of a passive low-pass filter in the field of electrical engineering. A low-pass filter consists of a resistor-capacitor combination as shown in Fig. 4-11.

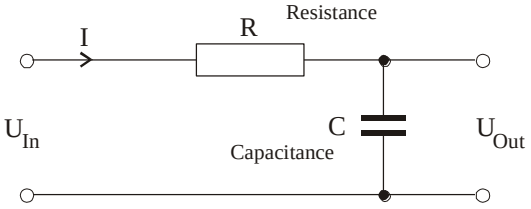

Fig. 4-11 Passive low-pass filter

The electrical passive low-pass filter shown above can be described by the following differential equation:

$$\frac{dU_{Out}}{dt} + \frac{1}{R_e C_e} \cdot U_{Out} - \frac{1}{R_e C_e} \cdot U_{In} = 0 \qquad \text{Eq. 4-16}$$

The time constant for the low-pass filter is defined as $\tau = R_e C_e$. Using this definition in Eq. 4-16 gives

$$\frac{dU_{Out}}{dt} + \frac{1}{\tau} \cdot U_{Out} - \frac{1}{\tau} \cdot U_{In} = 0 \qquad \text{Eq. 4-17}$$

Comparing Eq. 4-15 with Eq. 4-17 produces an analogous thermal time constant

$$\tau = \frac{l_{cond} \cdot C_h}{\lambda_{cond} \cdot A} \qquad \text{Eq. 4-18}$$

Analogously to the electrical time constant ($\tau = R_e C_e$), the thermal time constant can be separated into a thermal capacitance C_h and a thermal resistance

$$R_h = \frac{l_{cond}}{\lambda_{cond} \cdot A} \qquad \text{Eq. 4-19}$$

Continuing with this physical analogy, the circuit of the passive low-pass filter can be transformed into an equivalent thermal circuit.

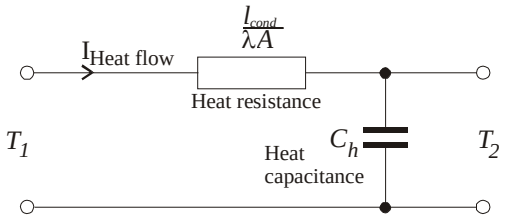

Fig. 4-12 Thermal equivalent of the passive low-pass filter

The step response functions of the electrical low-pass filter and the equivalent thermal circuit are as follows:

$$U_{Out} = U_{In} \cdot \left(1 - e^{-t/\tau}\right) \qquad T_2 = T_1 \cdot \left(1 - e^{-t/\tau}\right) \qquad \text{Eq. 4-20}$$

The thermal behaviour of each of the components used in the cantilever holder setup can be calculated using the equations above. The material constants needed to calculate the thermal response of each part of the setup are given in the table below. Tab. 4-3 provides the material constants needed to calculate the heat capacitance C_h.

	Specific heat capacity	Volume	Density ρ	Heat Capacitance C_h
Cantilever bar (native oxide)	700.0 $^{J}/_{kg*K}$	0.009 mm^3	2.33 $^{mg}/_{mm^3}$	14.6 10^{-6} $^{J}/_{K}$
Cantilever (native oxide)	700.0 $^{J}/_{kg*K}$	1.3 mm^3	2.33 $^{mg}/_{mm^3}$	2.7 10^{-3} $^{J}/_{K}$
Aluminium Cantilever holder (native oxide)	930.0 $^{J}/_{kg*K}$	36.9 mm^3	2.7 $^{mg}/_{mm^3}$	0.093 $^{J}/_{K}$
Aluminium To Peltier-Element (native oxide)	930.0 $^{J}/_{kg*K}$	159.7 mm^3	2.7 $^{mg}/_{mm^3}$	0.401 $^{J}/_{K}$
Aluminium To Water-Cooler (native oxide)	930.0 $^{J}/_{kg*K}$	231.6 mm^3	2.7 $^{mg}/_{mm^3}$	0.580 $^{J}/_{K}$
Titanium Holder receptacle (native oxide)	520.0 $^{J}/_{kg*K}$	118.8 mm^3	4.5 $^{mg}/_{mm^3}$	0.278 $^{J}/_{K}$
Zirconium oxide 0.5 mm	460.0 $^{J}/_{kg*K}$	45.4 mm^3	6.1 $^{mg}/_{mm^3}$	0.127 $^{J}/_{K}$
Zirconium oxide 1.0 mm	460.0 $^{J}/_{kg*K}$	86.3 mm^3	6.1 $^{mg}/_{mm^3}$	0.242 $^{J}/_{K}$
Constantan Heater	390.0 $^{J}/_{kg*K}$	2.2 mm^3	8.9 $^{mg}/_{mm^3}$	0.014 $^{J}/_{K}$
Aluminium oxide Heater cover	950.0 $^{J}/_{kg*K}$	9.2 mm^3	3.94 $^{mg}/_{mm^3}$	0.034 $^{J}/_{K}$
Aluminium oxide Piezo top cover	950.0 $^{J}/_{kg*K}$	50.0 mm^3	3.94 $^{mg}/_{mm^3}$	0.187 $^{J}/_{K}$
Polyamide Pressing block of the Peltier-Element	1700 $^{J}/_{kg*K}$	123.0 mm^3	1.14 $^{mg}/_{mm^3}$	0.238 $^{J}/_{K}$

Tab. 4-3 Material constants needed to calculate the heat capacitance for the different parts of the setup

Following calculation of the different thermal capacitances, the heat resistances R_h can be calculated using the part dimensions and material constants given in Tab. 4-4.

	Thermal path length l	Thermal contact area A	Specific heat conductivity λ	Heat Resistance R_h
Cantilever bar (native oxide)	0.23 mm	0.8 10^{-3} mm^2	130 $^{W}/_{m*K}$	2216 $^{K}/_{W}$
Cantilever (native oxide)	0.31 mm	3.1 mm^2	130 $^{W}/_{m*K}$	769.2 10^{-3} $^{K}/_{W}$
Aluminium Cantilever holder (native oxide)	2.45 mm	36.64 mm^2	239.0 $^{W}/_{m*K}$	280.3 10^{-3} $^{K}/_{W}$
Aluminium To Peltier-Element (native oxide)	11.13 mm	5.0 mm^2	239.0 $^{W}/_{m*K}$	9.1 $^{K}/_{W}$
Aluminium To Water-Cooler (native oxide)	11.14 mm	5.0 mm^2	239.0 $^{W}/_{m*K}$	9.3 $^{K}/_{W}$
Titanium Holder receptacle (native oxide)	1.4 mm	53.3 mm^2	21.9 $^{W}/_{m*K}$	1.2 $^{K}/_{W}$
Zirconium oxide 0.5 mm	0.5 mm	33.5 mm^2	2.1 $^{W}/_{m*K}$	7.14 $^{K}/_{W}$
Zirconium oxide 1.0 mm	1.5 mm	33.2 mm^2	2.1 $^{W}/_{m*K}$	21.42 $^{K}/_{W}$
Constantan Heater	0.1 mm	22.0 mm^2	19.5 $^{W}/_{m*K}$	233.1 10^{-3} $^{K}/_{W}$
Aluminium oxide Heater cover	0.25 mm	36.8 mm^2	24.5 $^{W}/_{m*K}$	279.6 10^{-3} $^{K}/_{W}$
Aluminium oxide Piezo top cover	0.5 mm	100.0 mm^2	24.5 $^{W}/_{m*K}$	204.1 10^{-3} $^{K}/_{W}$
Polyamide Pressing block of Peltier-Element	4.5 mm	100.0 mm^2	0.25 $^{W}/_{m*K}$	180.0 $^{K}/_{W}$

Tab. 4-4 Materials characteristics to calculate the heat resistances of the different parts of the setup

The heat transfer velocity can be calculated using these values and the electronic simulation software known as PSpice.

The layer of glue between the components (aluminium and zirconium oxide) is used for a sample calculation. The glue (Arctic Silver) has a specific heat conductivity of 7.5 $^{W}/_{m*K}$ and is stable from -40°C to above 150°C after curing. An adhesive layer should have a typical thickness of 11 µm between lapped bodies. The specific heat capacitance is approximately 150.0 $^{J}/_{kg*K}$ and the layer of glue has a volume of 10*10*0.011 mm^3. Using a density of 7.35 $^{mg}/_{mm^3}$, the heat capacitance C_h for the layer of glue is 1.2 10^{-3} $^{J}/_{K}$. The thermal resistance is calculated using Eq. 4-19. Therefore, it follows from the given dimensions and the specific thermal conductivity λ that the layer of glue has a heat resistance R_h of 733.3 10^{-6} $^{K}/_{W}$.

Fig. 4-13 shows the simulation circuit with the previously calculated values.

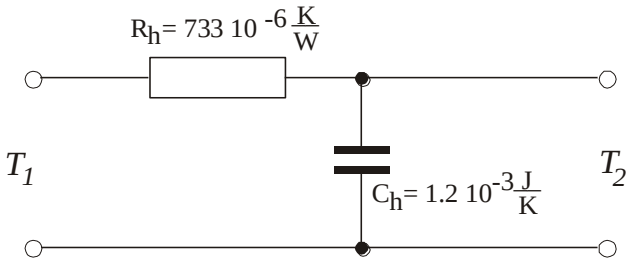

Fig. 4-13 Thermal simulation circuit for the glue layer

The simulation software can now be used to calculate and visualise the time variation of the temperature gradient and the temperature response at T_2 to a given temperature profile at T_1 for the layer of glue.

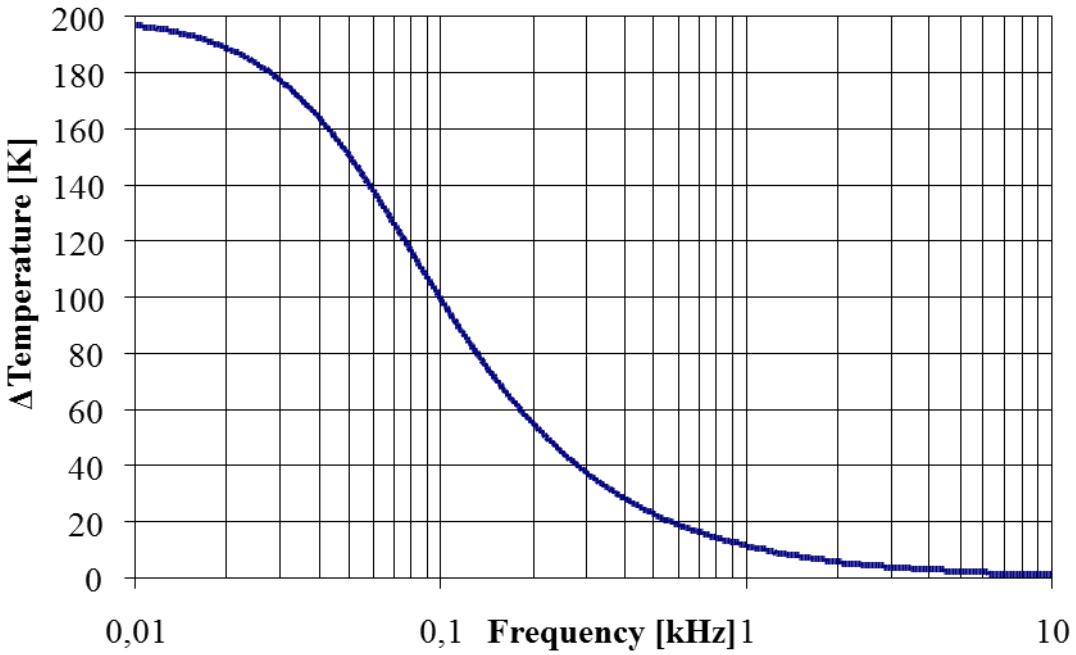

Fig. 4-14 Frequency-dependent temperature change

Fig. 4-14 shows a temperature versus frequency plot for the layer of glue corresponding to a sinusoidal temperature change.
The simulated temperature gradient is shown in Fig. 4-15. The temperature gradient is large relative to the small scale of the layer of glue (6 K per millisecond).
The thermal glue between the components of the cantilever holder setup ensures that the actual contact area has the same dimensions as the apparent area. Furthermore, all the components of the setup are lapped. Therefore, the layer of glue can be considered to have a constant thickness.
The layer of glue has been used as a demonstration of the simulation method. However, the heat resistance of the layer is 3 decades smaller and the heat capacitance is two times smaller, respectively, than the lowest values of all the other components of the cantilever holder setup.

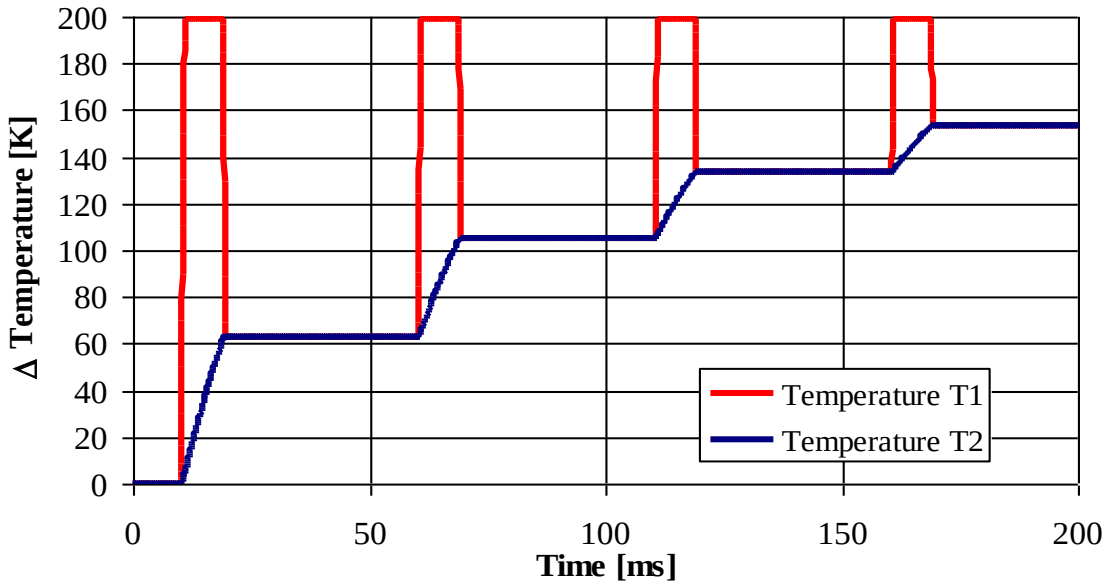

Fig. 4-15 Time-dependent temperature change

In the overall simulation of the complete holder, the following assumptions are made:

- The layers of glue are not accounted for due to the negligible effect they have on the setup;
- The contact area is equivalent to the seating;
- Thermal radiation is neglected because it has only a small effect in the temperature regime investigated.

Each simulated component consists of a resistor and a capacitor as shown in Fig. 4-13. An additional resistor in parallel with the capacitor simulates the convection loss for this component. The convection losses show a power law dependence of $^5/_4$ on the temperature difference (see Eq. 4-8). Therefore, a variable resistance is used to simulate the convection loss. Appendix A - 2 on page 85 shows a sub-circuit which fulfils the requirements of the variable resistance. Using T_{body}-T_{env}=*1* in Eq. 4-8 and taking the reciprocal of the result gives the resistance used in the simulation.
Fig. 4-16 shows the possible heating and cooling characteristic curves. The complete schematic of the simulation can be found in Appendix A - 1 on page 84.
The resistive heater (upper red curve) is heated up to 200 K above the ambient temperature (section A). The lower blue curve is the simulated temperature at the end of the cantilever bar where the tip is located. After 18 seconds, the cantilever bar reaches 140 K above the ambient temperature and after 40 seconds, the bar has a temperature of 150 K above the ambient temperature. The temperature of the heater must be decreased after the 40th second to maintain the temperature at the cantilever bar (section B). A PI feedback circuit is used to control the temperature within the system. After 100 seconds, the heater is switched off and heat losses of the setup can be observed (section C). As mentioned above, the calculated convection losses are slightly higher than in reality because a laminar flow is assumed for all the components and the initial temperature is taken to be the ambient temperature. In reality, the setup is covered within the cantilever holder disc so that the ambient air temperature is higher than the temperature outside the equipment. Furthermore, the initial temperature of each component of the stack 'sees' the air temperature of the component beneath it as the initial temperature for the convection calculation. Therefore, the system uses a Peltier cooler for a defined and computable cooling of the cantilever.

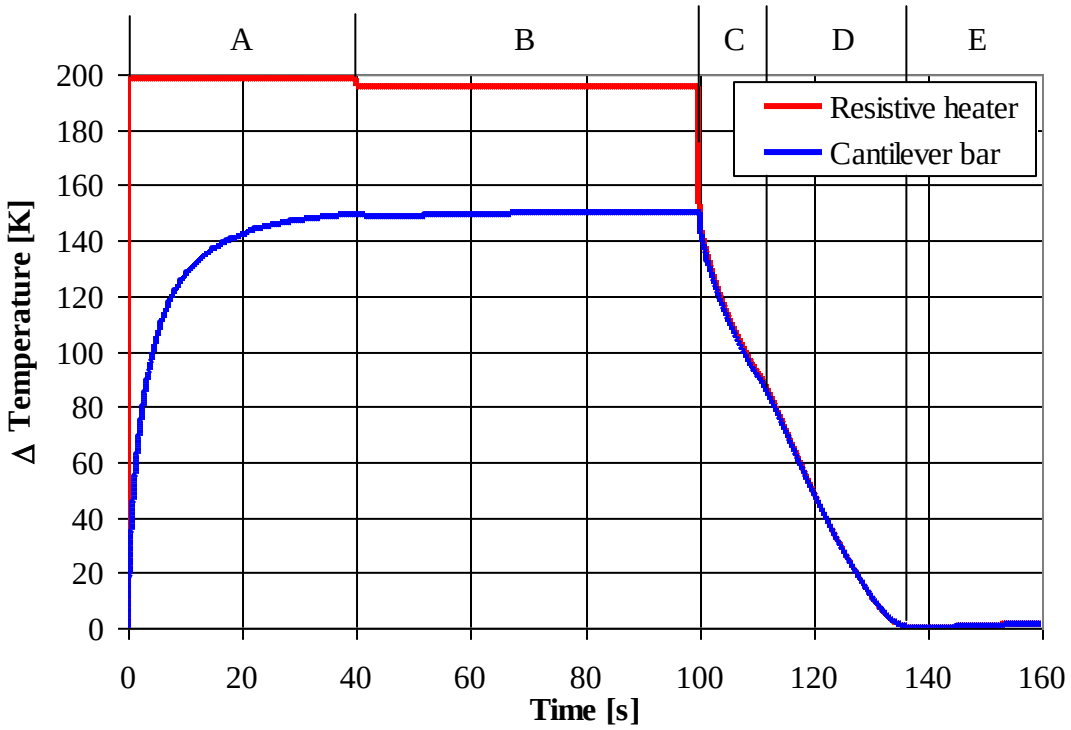

Fig. 4-16 Simulated temperature characteristics of the resistive heater and the end of the cantilever bar

After 110 seconds, the Peltier element is activated to cool the setup down (section D). A complete cool down from 150 K to 0 K above the ambient temperature takes less than 40 seconds. After the Peltier element is switched off (t= 138 s; section E) the temperature rises slightly again due to the temperature equilibration of the cantilever holder setup.

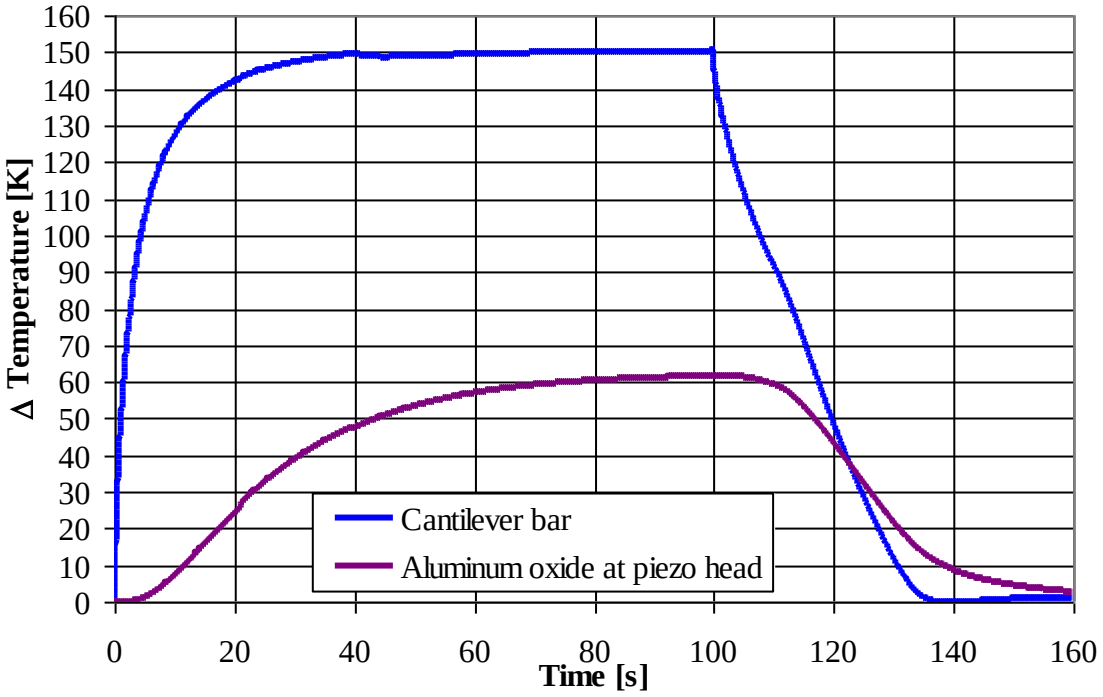

Fig. 4-17 Simulated temperature characteristics at the end of the cantilever bar and the piezo/zirconium boundary

Another important temperature measurement site, which should be simulated, is at the upper aluminium oxide disc of the piezo stack (Fig. 4-10, page 4-28).
This measurement indicates the temperature that affects the dither piezo stack. The piezo ceramic looses its piezo electrical properties if the ceramic is heated above its Curie temperature. The Curie temperature depends on the particular ceramic material. Fig. 4-17 shows the calculated maximum temperature at the top of the piezo stack, which is approximately 62 K above the ambient temperature. The shear piezos used are produced by the PIC 255 ceramic (Company: Physik Instrumente PI). This type of ceramic has a Curie temperature of 350°C. Therefore, the maximum temperature at the dither piezo for the cantilever is far below the Curie temperature, even if self-heating by the piezo takes place.
This system can be used with standard cantilevers used for typical AFM measurements like contact or non-contact measures. The cantilever used here has a time constant τ of narrow 17 ms derived from Fig. 4-17. Alternative to the heated cantilever holder setup leading the thermal flux through the cantilever to the tip, piezo-resistive cantilevers could be used. There are different types of piezo resistive cantilever on the market and they differ in production of the resistive area and dimension. A bulk resistive heater in the cantilever bar has a τ between 350 µs to 450 µs[26]. The time constant can be decreased to 0.8 µs to 10 µs using an ion implant and annealing process[27]. These values were derived from the resistive changing during the heating process. Therefore, no prediction can be made of the tip-sample thermal behaviour. Due to the prize of such cantilever, the application and its needed temperature gradients must decide between heated cantilever tip, cantilever bar and bulk heated cantilever.
The simulation shows that the cantilever setup can change temperature dynamically during the time period of the scan. These temperature changes make it possible to heat and cool the cantilever during even one scan line. Standard measurements and friction measurements are possible with several heating and cooling cycles or with user-defined temperature ramps adapted to the experimental requirements. Frictional measurements on polymers at or around the glass transition temperature and lithographic modifications on sample surfaces are feasible.
However, the cantilever is a local heating source. To observe global heating and cooling cycles during data acquisition, the sample must itself be heated. The following section describes the sample holder setup for temperature control of the sample.

4.3 The sample holder setup

The same difficulties are encountered for the sample holder as for the cantilever holder. A maximum thermal dynamic and a temperature guard for the piezos are necessary.

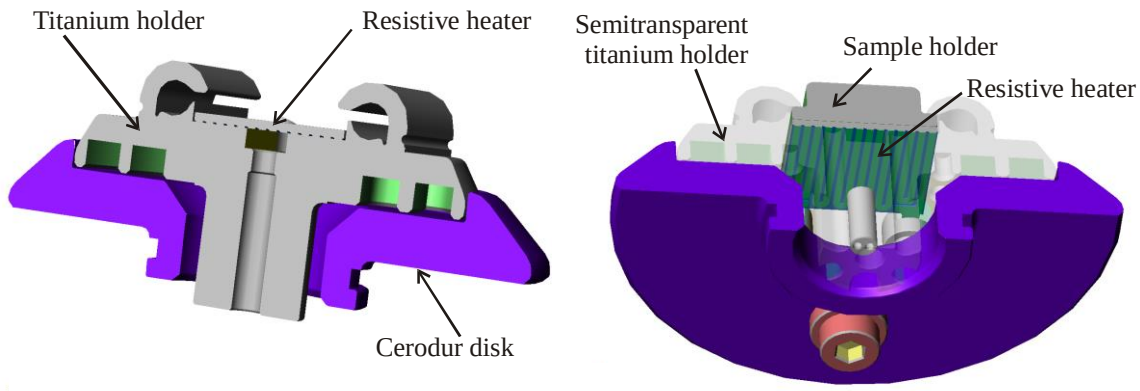

Fig. 4-18 Sample holder with the receptacle and the Zerodur® disc

The complex shapes of the different parts of the sample holder complicate the estimation of the thermal path lengths. To obtain useful results, the shortest path lengths will be used for insulating materials and the longest path lengths for thermal conducting materials. This approximation corresponds to a worst-case scenario, such that the equipment should work more efficiently in reality than estimated.
An overview of the setup of the sample holder is given in Fig. 4-5 and Fig. 4-6. A detailed description relating to the thermal properties of the high frequency Z-piezo drive and the implemented sample holder is given in the following figures.
Fig. 4-18 (right) shows the sample holder inserted in the holder receptacle, in between which the resistive heater is located. The lower violet-coloured component is the thermal shield made of Zerodur® for the z-piezos. Zerodur® is a glass ceramic and has a very low thermal conductivity of 1.46 $^{W}/_{m*K}$. The titanium holder has notches in its lower side to reduce the mass and the contact area between the holder and the Zerodur® disc.

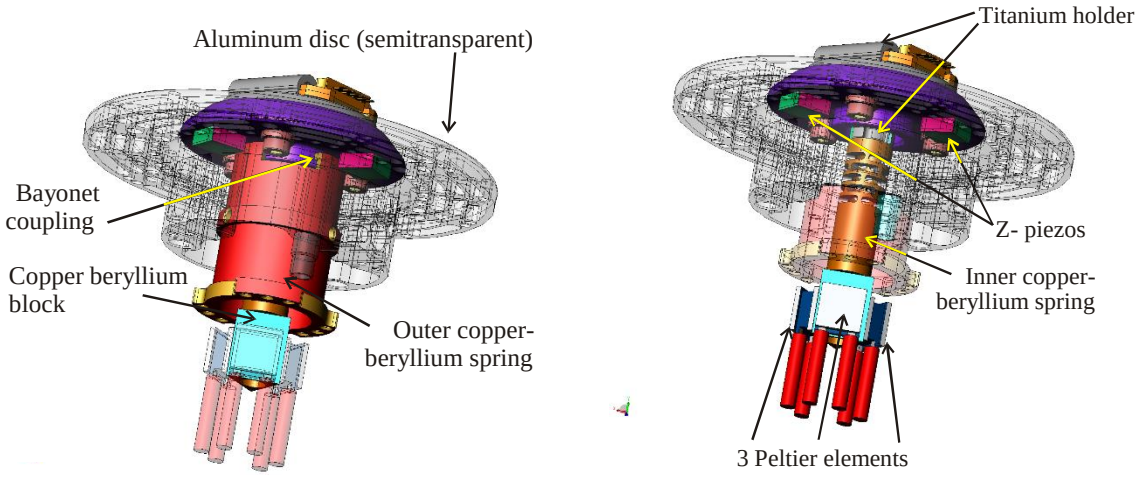

Fig. 4-19 Sample holder with outer pre-loaded springs (left) and inner (right) contact spring

The setup of Fig. 4-18 is mounted on an aluminium disc as shown in Fig. 4-19. The aluminium disc is bolted to the titanium holder. Serrated lock washers ensure that the screws are held in place even during temperature changes. The washers further reduce the contact area between the screws and the aluminium disc, lowering the heat flux to the disc.
The Zerodur® disc is equipped with a copper-beryllium spring. This spring is visible on the left-hand side of Fig. 4-19. The red cylindrical spring is connected to the Zerodur® disc by a bayonet coupling. The spring is laser-structured such that its resonance frequency is higher than the resonance frequency of the piezos (this structure is not shown in the figure). This spring presses the Zerodur® disc with the cantilever holder onto the three Z-piezos (two piezos can be observed in Fig. 4-19; the third piezo is hidden by the inner beryllium spring). A piezo is a multilayer assembly of ceramic, conductive and insulating layers and can be destroyed by low pulling forces.
The outer spring provides the three piezos with the necessary pre-loading force. The spring is elongated approximately 2 mm and the high-frequency Z-piezos are compressed by approximately 2.3 µm. Thus, the variation in the force on the piezo is about a thousandth of the pre-loading force.
The inner copper/beryllium spring is bolted to the titanium holder on the upper side and to a triangular-shaped copper/beryllium block on the lower side (Fig. 4-19, right side). Three Peltier elements are connected to the block, one on each face of the triangular shape. The left side of the exploded assembly drawing of Fig. 4-20 also shows the inner copper beryllium spring.

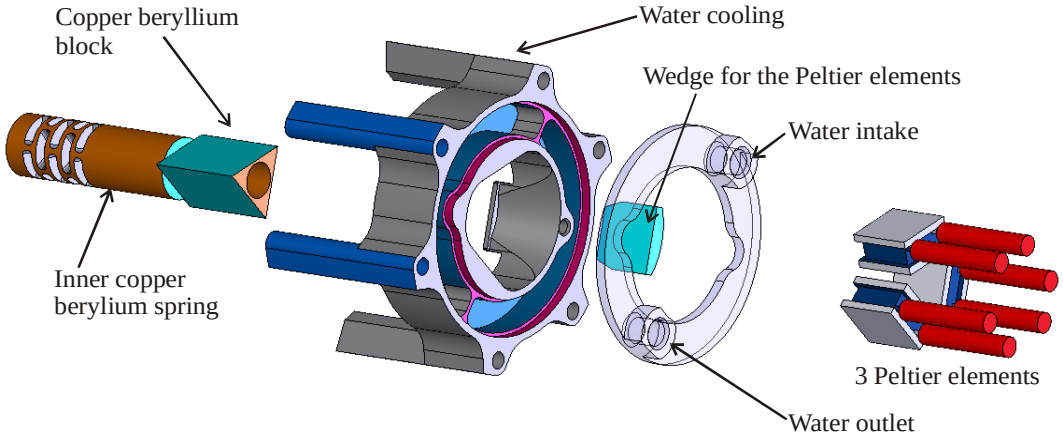

Fig. 4-20 Inner copper beryllium spring with Peltier elements and water cooling block

The water cooling block with two waterways and a semi-transparent cover with the intake and outlet can be observed in the centre of the figure. The right side shows the three Peltier elements. The spring is inserted into the cooling block from the left side and the three Peltier elements are inserted from the right side to enclose the triangular-shaped copper beryllium block. This assembly is pressed together by the wedge. The setup shown is then mounted within the sample holder setup. Fig. 4-21 shows the configuration from the bottom view (left side) and from the side view (right side).

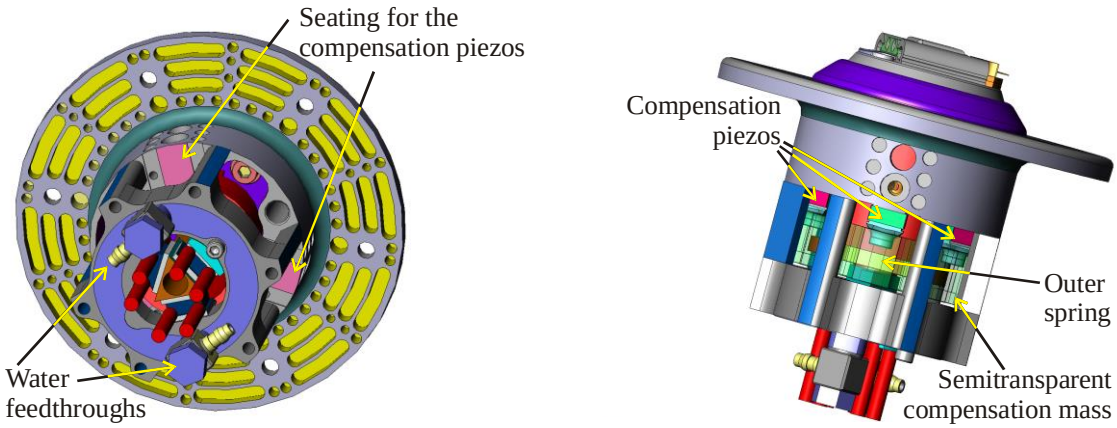

Fig. 4-21 Thermal setup of the sample holder; bottom view (left) and side view (right)

The left side of Fig. 4-21 shows the clamped Peltier elements within the water cooling block. The block is bolted to the aluminium disc (the six screws are hidden in this view). The two water feedthroughs and the seating of two of the three compensation piezos can be observed. The compensatory mass is hidden to provide a better view of the thermal details of the setup.
The side view (right side of Fig. 4-21) shows the complete stack with sample holder, receptacle disc, Zerodur® disc, aluminium disc and water cooling block. The piezos for the high frequency Z-drive lie in between the Zerodur® and aluminium disc and cannot be observed here. Between the legs of the water cooling block, the inner and the semi-transparent outer copper beryllium spring can be observed. All three compensation piezos are shown.

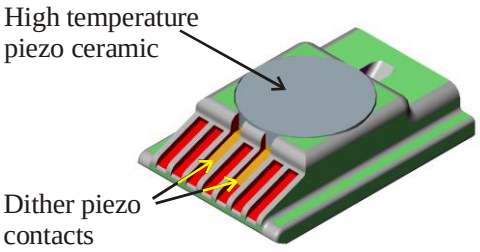

Fig. 4-22 Sample holder with a high-temperature dither piezo ceramic

The setup shown does not allow for a thermally insulated dither piezo for the sample. Therefore, the temperature can exceed temperatures above the Curie temperature for standard piezo ceramics. If a thermal heater and a dither piezo for the sample are needed, a special piezo ceramic with a higher Curie temperature must be used. Modified bismuth/titanate has a Curie temperature of approximately 820 °C. This ceramic can withstand sample temperatures of approximately 150 K above the ambient temperature.
The dither piezo is covered with a thin copper foil that is glued to the piezo and the sidewalls of the holder to lower the thermal resistance. Fig. 4-22 shows the sample holder without the copper foil to illustrate the position of the dither piezo.
In the next section, the simulation of the sample holder setup described here will be discussed.

4.4 Independent temperature control of the sample

The sample holder can be heated independently in addition to the independent cantilever temperature control. A simulation of the thermal behaviour of the sample holder setup models the possible thermal dynamics, as performed previously for the cantilever holder.
The calculated radiation loss for the cantilever holder is only a few milliwatts compared to 15 W of heating power. Radiation losses are only observable at much higher temperatures than the maximum temperature of 150 K above the ambient temperature that is used here. Therefore, radiation losses are also neglected in this setup.

	Effective Surface size	Effective convection length
Aluminium Sample holder (native oxide)	12.1 mm²	1.9 mm
Titanium Holder receptacle (native oxide)	121.6 mm²	1.6 mm
Zerodur® Thermal shield	59.4 mm²	2.2 mm
Aluminium Z- piezos holder disk	135.5 mm²	2.5 mm
Copper beryllium inner spring	348.7 mm²	18.5 mm
Copper beryllium outer spring	529.5 mm²	16.9 mm

Tab. 4-5 Effective surface sizes and lengths of the different components to calculate the convection loss of the sample holder setup

Convection is the other and more important loss mechanism. Convection depends on the surface area where the convection takes place and the length of the path where the ambient air is in contact with the solid material for heat transfer. Eq. 4-8 from page 4-31 is used to calculate the overall convection for a maximum temperature of 150 K above the ambient temperature.

The following chart shows the calculated values for the effective surface sizes and the effective convection lengths of the different components used in the actual setup.
The same conditions as for the cantilever holder will be assumed. The sample holder is heated up to 150 K above the ambient temperature and held at this temperature. Two assumptions will be made about the sample holder setup. First, the aluminium disc is connected to the aluminium components of the mid-range frequency Z-drive where the maximum temperature is 80K above the ambient temperature. This is a reasonable assumption because the disc is insulated by the Zerodur® disc. The only connection to the titanium receptacle is by the three screws and the serrated lock washers, which keep the thermal contact area to a minimum.

	Specific heat capacity	Volume	Density ρ	Heat Capacitance C_h
Aluminium Sample holder (native oxide)	930.0 $^{J}/_{kg*K}$	202.6 mm^3	2.7 $^{mg}/_{mm^3}$	0.51 $^{J}/_{K}$
Titanium Holder receptacle (native oxide)	520.0 $^{J}/_{kg*K}$	988,93. mm^3	4.5 $^{mg}/_{mm^3}$	2.31 $^{J}/_{K}$
Aluminium oxide Heater cover	950.0 $^{J}/_{kg*K}$	40.3 mm^3	3.94 $^{mg}/_{mm^3}$	0.15 $^{J}/_{K}$
Constantan Heater	390.0 $^{J}/_{kg*K}$	5.6 mm^3	8.9 $^{mg}/_{mm^3}$	19.4 10^{-3} $^{J}/_{K}$
Zerodur® Thermal shield	800.0 $^{J}/_{kg*K}$	1706.2 mm^3	2.53 $^{mg}/_{mm^3}$	3.45 $^{J}/_{K}$
Copper-beryllium Inner spring	385.0 $^{J}/_{kg*K}$	519.8 mm^3	8.8 $^{mg}/_{mm^3}$	1.76 $^{J}/_{K}$
Copper-beryllium Outer spring	385.0 $^{J}/_{kg*K}$	370.9 mm^3	8.8 $^{mg}/_{mm^3}$	1.26 $^{J}/_{K}$
Copper foil Z-piezo protection Small area	389.0 $^{J}/_{kg*K}$	5.5. mm^3	8.92 $^{mg}/_{mm^3}$	19.1 10^{-3} $^{J}/_{K}$
Copper foil Z-piezo Large area	389.0 $^{J}/_{kg*K}$	3.6. mm^3	8.92 $^{mg}/_{mm^3}$	12.5 10^{-3} $^{J}/_{K}$
Piezo 6x6x2 mm	350.0 $^{J}/_{kg*K}$	50.0 mm^3	7.7 $^{mg}/_{mm^3}$	0.13 $^{J}/_{K}$
Aluminium Z- piezos holder disk (native oxide)	930.0 $^{J}/_{kg*K}$	6230.5 mm^3	2.7 $^{mg}/_{mm^3}$	15.6 $^{J}/_{K}$
Aluminium Leg of water cooler (native oxide)	930.0 $^{J}/_{kg*K}$	33.6 mm^3	2.7 $^{mg}/_{mm^3}$	84.4 10^{-3} $^{J}/_{K}$
Steel screw	500.0 $^{J}/_{kg*K}$	43.8 mm^3	8.03 $^{mg}/_{mm^3}$	0.18 $^{J}/_{K}$
Spring steel serrated lock washers	490.0 $^{J}/_{kg*K}$	5.1 mm^3	7.85 $^{mg}/_{mm^3}$	19.6 10^{-3} $^{J}/_{K}$

Tab. 4-6 Material characteristics to calculate the heat capacitance of the different components of the setup

Furthermore, the aluminium disc is permanently cooled via the six legs from the water cooler. The second assumption is that the outer copper beryllium spring has a maximum temperature of 80 K above the ambient temperature because the middle of the spring is connected to the aluminium disc with an assumed temperature of 80 K. Both materials have well, if not very well, thermal conductivity so that the thermal gradients within the components are very low.
The overall convection loss is calculated to be 2.2 W. This represents a maximum value, due to the assumption of a laminar flux and because all the components are surrounded with air at the ambient temperature. Further, the inner spring is more or less encapsulated within the outer spring. Thus, the air temperature between the springs can attain the material temperature resulting in the disruption of convection due to the absence of a temperature gradient.

	Thermal path length l	Thermal contact area A	Specific heat conductivity λ	Heat Resistance R_h
Aluminium Sample holder (native oxide)	3.0 mm	87.0 mm^2	239.0 $^{W}/_{m*K}$	144.3 10^{-3} $^{K}/_{W}$
Titanium Holder receptacle (native oxide)	9.1 mm	68.7 mm^2	21.9 $^{W}/_{m*K}$	6.0 $^{K}/_{W}$
Aluminium oxide Heater cover	0.4 mm	100.8 mm^2	24.5 $^{W}/_{m*K}$	162.0 10^{-3} $^{K}/_{W}$
Constantan Heater	0.08 mm	63.6 mm^2	19.5 $^{W}/_{m*K}$	64.5 10^{-3} $^{K}/_{W}$
Zerodur® Thermal shield	9.8 mm	24.6 mm^2	1.46 $^{W}/_{m*K}$	272.85 $^{K}/_{W}$
Copper-beryllium Inner spring	37.0 mm	24.8 mm^2	226 $^{W}/_{m*K}$	6.6 $^{K}/_{W}$
Copper-beryllium Outer spring	17.8 mm	38.9 mm^2	226 $^{W}/_{m*K}$	2.02 $^{K}/_{W}$
Copper foil Z-piezo protection Small area	2.0 mm	0.2 mm^2	401 $^{W}/_{m*K}$	24.9 $^{K}/_{W}$
Copper foil Z-piezo Large area	0.1 mm	36.0 mm^2	401 $^{W}/_{m*K}$	6.9 10^{-3} $^{K}/_{W}$
Piezo 6x6x2 mm	2.0 mm	36.0 mm^2	1.1 $^{W}/_{m*K}$	50.5 $^{K}/_{W}$
Aluminium Z- piezos holder disk (native oxide)	13.3 mm	1.2 mm^2	239.0 $^{W}/_{m*K}$	46.4 $^{K}/_{W}$
Aluminium Leg of water cooler (native oxide)	10.5 mm	3.2 mm^2	239.0 $^{W}/_{m*K}$	13.7 $^{K}/_{W}$
Steel Screw	3.5 mm	7.3 mm^2	16.27 $^{W}/_{m*K}$	37.9 $^{K}/_{W}$
Spring steel serrated lock washers	1.0 mm	2.7 mm^2	46.73 $^{W}/_{m*K}$	7.9 $^{K}/_{W}$

Tab. 4-7 Material characteristics to calculate the thermal resistance of the different components of the sample holder setup

The dynamic behaviour for the system will now be examined. The heat capacitance of each component is first calculated. To lower thermal effects on the three high frequency Z-piezos, a thin copper foil is glued on top of the piezos and to the aluminium disc. The copper foil drains the heat from the Zerodur® disc to the aluminium disc, reducing the thermal exposure of the piezos.
The setup of the sample holder is more complicated than the cantilever setup in terms of calculating the thermal flux. More contact areas and parallel connections need to be simulated. All the calculated values in Tab. 4-6 and Tab. 4-7 are for single elements, such as for one screw or one leg of the water cooling block. Tab. 4-6 shows the different thermal capacities and Tab. 4-7 lists the thermal resistances for the components of the sample holder setup.
The schematic for the simulation can now be generated using the calculated values of the three charts. The thermal circuit for each component is the same as for the cantilever setup (see Fig. 4-13 on page 4-36) using the values from the charts. Likewise, an additional non-linear resistor in parallel with a capacitor is used to simulate convection losses.
The schematic of the simulation is shown in Appendix A - 5 on page 86. The results of the simulation are shown in Fig. 4-23 and Fig. 4-24.
Fig. 4-23 shows the heater temperature (blue curve) and the temperature at the surface of the sample holder. The resistive heater is driven for 15 seconds at a temperature of 200 K above the ambient temperature (section A). After 15 seconds, the temperature difference between the sample holder and the environment is 150 K. Section B shows that this temperature can be maintained using a heater temperature of 184 K. After the heater is switched off (section C), the temperature decreases due to heat losses. After 110 seconds, the three Peltier elements are switched on (section D). The Peltier elements help to decrease the temperature of the sample holder to the ambient temperature. A temperature difference between the sample holder and the ambient of 0 K is reached after less than 40 seconds.

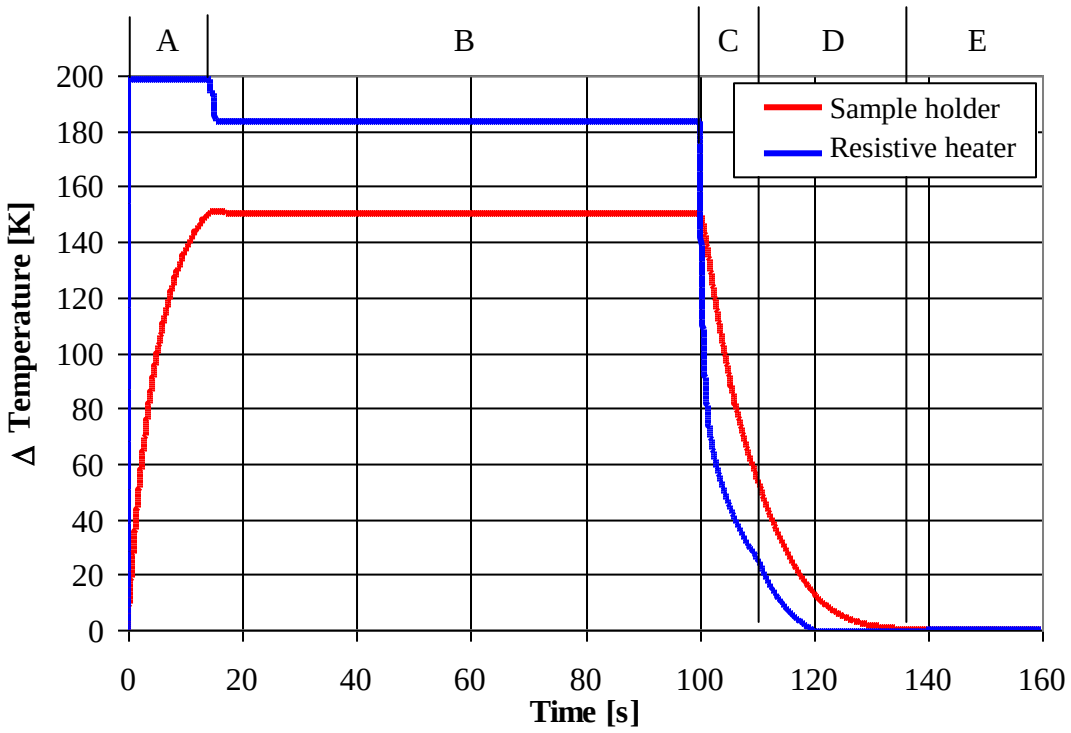

Fig. 4-23 Temperature characteristics of the resistive heater and the sample holder

The Peltier elements are switched off after 140 seconds and the temperature difference between the sample holder and the ambient remains at 0 K (section E).

he piezo-stacks of the setup for the sample-holder are located near the heat source. These stacks can be damaged as well if the temperature rises to the vicinity of the Curie temperature of the piezo material. The piezo stacks are protected by the Zerodur® disc and the copper foils. The Zerodur® disc has a high thermal resistance so that heat transferred to the disc can be sent to the thermal sink, i.e., the copper-beryllium spring. The portion of the heat that reaches the part of the Zerodur® disc where the piezos are located is guided through the aluminium disc via the copper foil. This remainder of the heat reaching the piezo stack is calculated and shown in Fig. 4-24.
The maximum temperature of the piezos is about 30 K above the ambient temperature. Thus, the piezos in the sample holder setup are well protected.
This chapter has shown the temperature capabilities of the cantilever holder and sample holder. The temperature of the various piezos is in a range where the piezos do not lose their piezo electric properties. However, the heat ageing of the piezos increases with the temperature and the heating time.

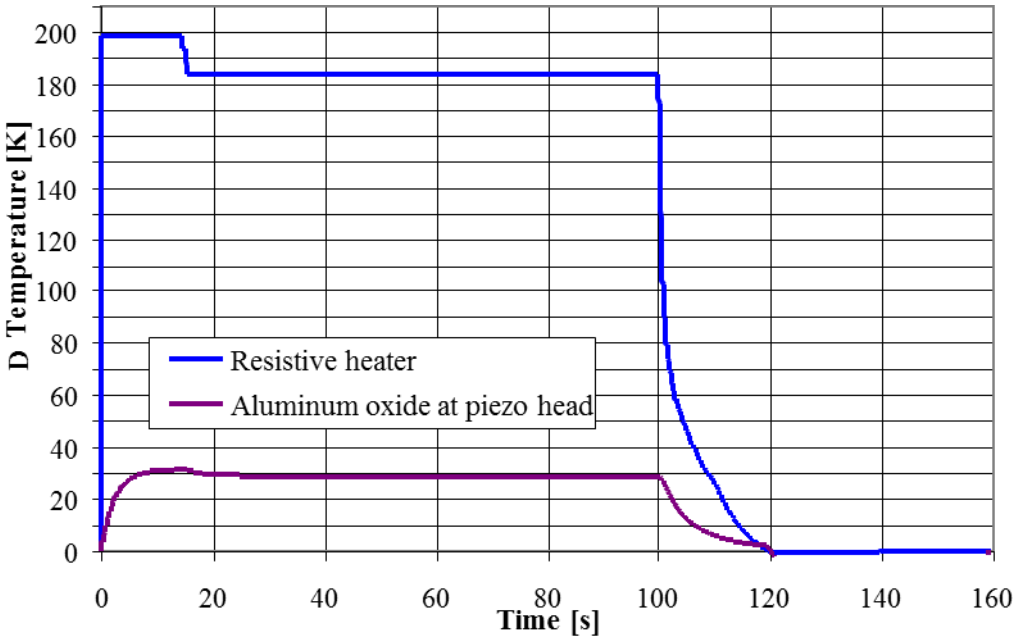

Fig. 4-24 Temperature characteristics of the resistive heater and the piezo/copper foil boundary

The cantilever bar and the sample holder can be separately tempered to approximately 150 K above the ambient temperature. This presents a range of experimental setups that these holders could be used for as described in the following section.

4.5 Possible uses for the cantilever holder and sample holder

Beside the normal use of the cantilever holder and the sample holder, the individual temperature control of both holders opens up possibilities for a variety of new scanning techniques, as well as the modification of existing well-known scanning techniques.
The novel SFM has the ability to ramp the temperature over a time period spanning several image scans. Thus, measurements can be made at an equilibrated sample temperature and slow temperature-dependent material changes can be observed.
Indentation experiments can be performed on globally heated samples or with locally heated samples using the cantilever. Vice versa, the heated sample can be indented with an actively cooled cantilever.

The temperature control capabilities are also useful for dip pen lithography. Normally, a liquid dip is used, such as a water-based solution. However, with the individual temperature control of the cantilever, a solution with higher and/or temperature-dependent viscosity can be used.
The sample can be preheated, so that the temperature change of the cantilever can be small enough to modify the sample surface.
The exhaust steam ratio can be measured from a heated surface. The cantilever can be cooled to increase the ratio. A chemically activated cantilever can also be used. This type of cantilever collects only a specific portion of the exhaust and the cantilever can be heated to remove the condensation artefacts of undesirable species.
The techniques discussed here have been presented to provide an overview of possible options and are not meant to be comprehensive.

5 Optimisation of the light beam guidance for failure-minimised detection of the normal and lateral cantilever deflection

Beside the mechanical loop setup, the beam deflection system is one of the most delicate components of a highly sensitive and stable scanning force microscope. Various problems may occur, as discussed below. Lasers are sensitive to temperature and current fluctuations, even in the small signal regime. The heating of air by the sample and/or cantilever leads to density fluctuations of the air and thus affects the beam. The beam spot size, which is broader than the width of the cantilever, can lead to interference effects, disturbing the four-quadrant photodiode (4Q-PD), especially with reflective samples. Last, but not least, the detection unit has to accurately collect data from the moving beam, depending on the cantilever motion. The following sections provide more details on these challenges and their solutions.

5.1 Advantages of a fibre optical light source for the beam deflection setup

The motion of the scanned cantilever can be detected using different measuring systems. The beam deflection system and the interferometer system are well-known examples[28]. Other systems use resistive cantilevers, a tunnelling tip or a capacitive detector to detect the cantilever motion. One disadvantage of some detection systems is the lack of a torsional measurement to detect the lateral force. Another disadvantage is the necessarily small distance between the cantilever and detection system.

The novel scanning force microscope uses a beam deflection system to detect normal and lateral motion with the 4Q-PD. The light source and the photodiode can be far away from the cantilever for a parallel beam.

A convergent, divergent or parallel beam shape and the power distribution within the beam influence the signal quality of the measuring system. The majority of scanning force microscopes uses a laser in the beam deflection system, which has a high coherence. Thus, a volitional reflection from the cantilever can interfere with a non-volitional reflection from the sample surface, causing an erroneous signal to be measured by the photodiode detector[29]. Focusing 100% of the beam on the cantilever is the easiest way to avoid interference from backscattered laser light from the surface. However, focusing down to a diameter of a few tenths of microns is complicated, as will be later discussed. In addition to introducing quantum noise and mode hopping noise, destroying the coherence provides an opportunity against the interference effect[30]. An alternative known as the ‘Power LED’ has been developed over the last few years. However, these types of LEDs have a large emission area, requiring the beam to be focused on the cantilever with a focus width equal to or less than the width of the cantilever: a single lens system with an aperture is highly inefficient. However, a focus width far below the cantilever width is also inefficient because the roughness of the reflection zone of the cantilever dominates the dispersion of the beam. The local light power density of the focus point is also high enough to heat the cantilever, bending the cantilever in the worst case. Bending can also occur for cantilevers with a reflection coating, due to the different thermal expansion coefficients of the cantilever and the coating material.

The laser in the system presented here is used in an unusual way. To maximise performance, the LED has a small coherence length and the laser has a small emission area. Thus, the laser can be driven below the laser condition with constant current in the ‘LED mode’ and the small emission area facilitates coupling light into the glass fibre with a single lens.

If the focal point is positioned exactly on the cantilever, the opening angle of the incident beam can affect the optical lever amplification. Even if a light source with a waist is used to generate the focus, the simplification afforded by crossing light rays does not affect the assertion of

plausibility. From the theorem on intersecting lines, the light beam widens and the power density decreases such that the photocurrent of a 4Q-PD is constant even for long distances, neglecting the non-photosensitive gap (see Fig. 5-1). Thus, if the angle of the deflection is small relative to the opening angle of the divergent light beam, the lever amplification cannot be increased by increasing the distance in the cantilever-photodiode arrangement.

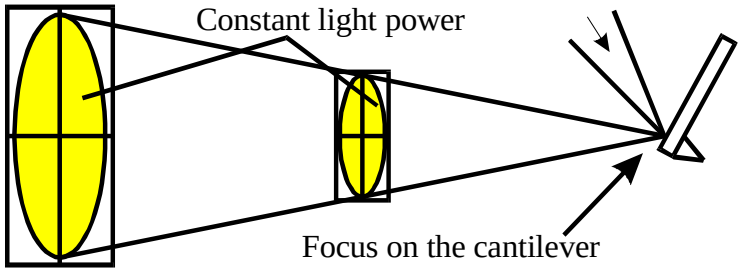

Fig. 5-1 The differential signal of the 4Q-PD is independent of the distance to the light source

In contrast, setting up a parallel light beam is more involved. The higher lever amplification leads to a longer path of the reflected beam on the photodiode and consequently to a stronger electric signal. It follows that the light guidance should be optimised such that the beam is almost parallel, resulting in higher sensitivity. Decreasing the active photodiode area can increase the sensitivity of detection of cantilever motion. This results in an improved signal-to-noise-ratio because of the decrease in the NEP (noise equivalent power [see Eq. 5-7]), the gap between the four areas of the 4Q-PD and the junction capacitance (which primarily defines the bandwidth of the detection system).
Setting up a laser beam with a diminutive divergence and a diameter approximately 30 µm is challenging[29] because the free geometric volume within a scanning force head is small and the thermal exposure must be small, too.
A single mode glass fibre with a core diameter of 2.3 µm is used to approximate an ideal point source as closely as possible.

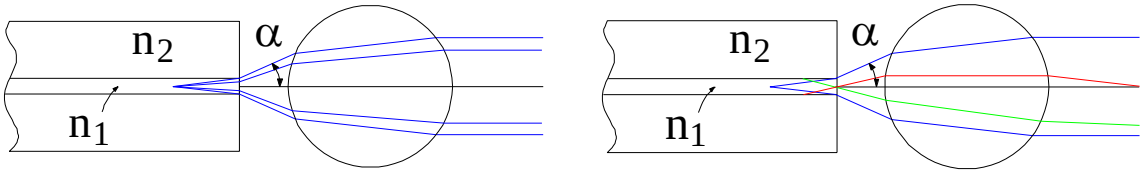

Fig. 5-2 Diagram of an ideal (left) and non-ideal light point source

A spherical lens is adjusted so that the focal point of the sphere is positioned at the theoretical focal point within the glass fibre (Fig. 5-2 left side). For a known numerical aperture (NA) and refractive index of the material of the sphere, the beam diameter can be calculated as follows:

$$d_{Beam} = \frac{NA \cdot n \cdot d_{Sphere}}{2(n-1)} \qquad \text{Eq. 5-1}$$

In practice, the glass fibre is non-ideal so that the ‘focal point’ of several rays is distributed within the glass fibre core (Fig. 5-2, right side). Therefore, a lens with a short focal length cannot focus an upwardly directed beam because it leaves the core below the optical axis, as shown in the left side of Fig. 5-3. This may result, for example, in only a portion of the light power being focused on the cantilever with the non-focused light forming a halo around the centre, which can lead to interference effects. Consequently, a lens with long focal length is necessary. A more efficient lens-area-to-surface-roughness ratio can also reduce the effect of

surface roughness. Other lens types such as drum lenses must be used because the diameter of a spherical lens with a long focal length is too large.
The focal length can also be reduced by modifying the glass fibre to decrease the NA and the fibre-lens distance can be decreased respectively, to shrink the diameter of the sphere. One way to change the NA is to generate a spherical lens at the end of a glass fibre. The glass fibre used here has an outer diameter of 125 µm with a core diameter of 2.3 µm, as mentioned above. With an NA of approximately 0.14, the half-opening angle is 5.5°, so that the virtual focal point within the fibre is approximately 20 µm away from the end of the fibre. A 15-µm diameter for a half-sphere at the end of the fibre is calculated to produce an ideal parallel beam output.
The diameter of the glass fibre must be reduced to fabricate a sphere of the required size. A new, hydrofluoric acid-free method has been developed for this system[31]. A rotating glass fibre is pressed into a groove of a perpendicular, rotating steel shaft. Different types of shapes can be produced by varying the grinding pressure, particle size and the amount of grinding material in the fluid, as shown in Fig. 5-4 (small pictures, centre and bottom). The upper small image shows an incompletely ground glass fibre.

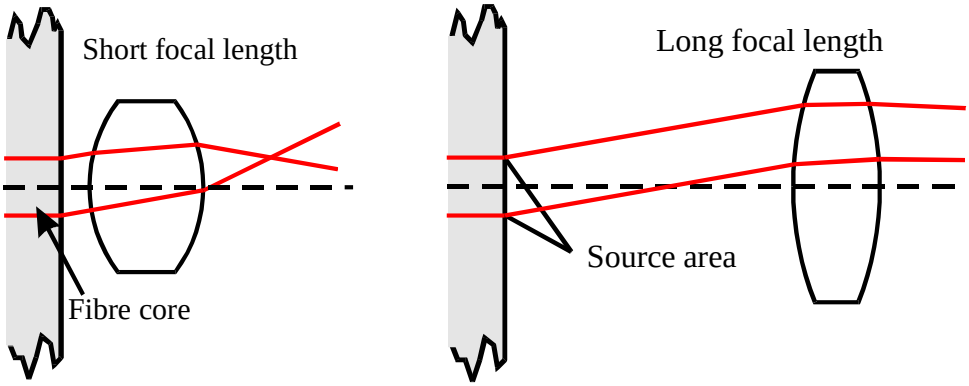

Fig. 5-3 Dependence of the light source distribution on the focusing capability of short and long focal length lenses

This grinding process is self-adjusting if the pressure and the amount of grinding fluid are constant. A standard glass fibre splice-tool is used for the lens. The sphere is melted from the original tip of the fibre (Fig. 5-4, right image; a glass fibre with an outer fibre diameter of 54 µm is needed for a 9-µm core): the size is varied by controlling the time and the power of the arc of the splice tool[32].

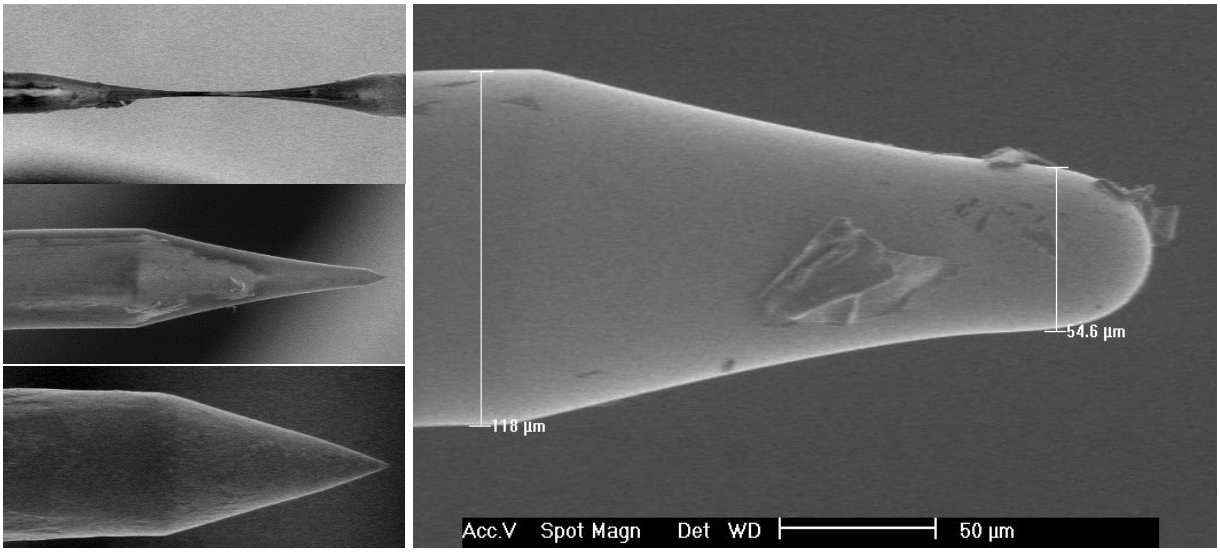

Fig. 5-4 Different grinding profiles and a melted glass fibre tip (patents submitted[31 32])

The NA can be lowered by a factor of two. With such a ground and melted glass fibre, together with a plane convex lens (focal length 12 mm), a focus on a 40-µm wide cantilever at a 35-mm distance is produced without an aperture. Less than 2% of the incident light misses the cantilever.
Interestingly, a similar result can be produced with a non-ground glass fibre and a lens that is several times bigger, as shown in Fig. 5-6.

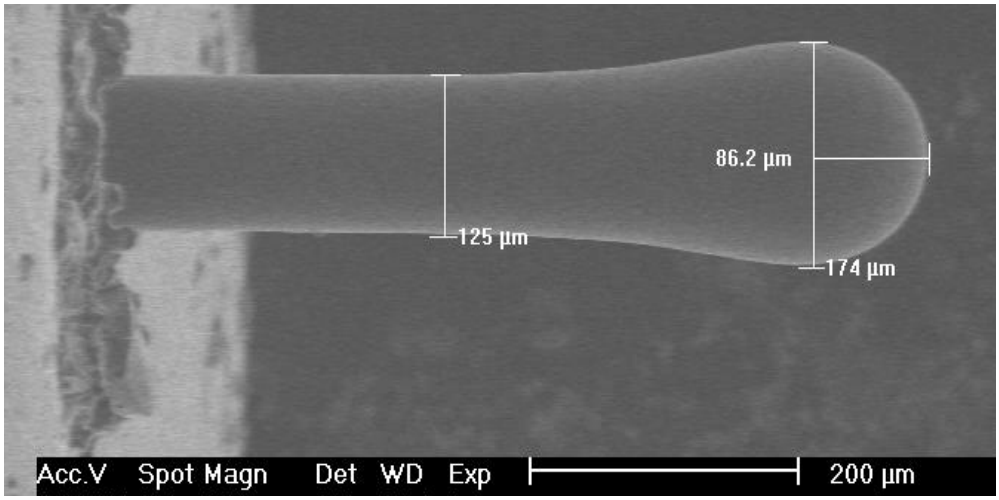

Fig. 5-5 A 'match'-shaped glass fibre

This behaviour can be explained by the construction of the glass fibre. The core and cladding are made of glass and differ by a boron-doped core, in the simplest case. The doping changes the refractive index of the glass fibre. The refractive index differs between the core and the cladding in a few parts per thousandth. This leads to light being guided within the core. The melting of the glass fibre to form a lens at the end of the fibre is accompanied by additional changes beyond the change in the outer shape of the glass fibre. The thermally induced deformation also affects the doping profile between the core and cladding. There is only a small deformation at the ground tip because the melting process is short and only a very small part at the end of the tip is melted.

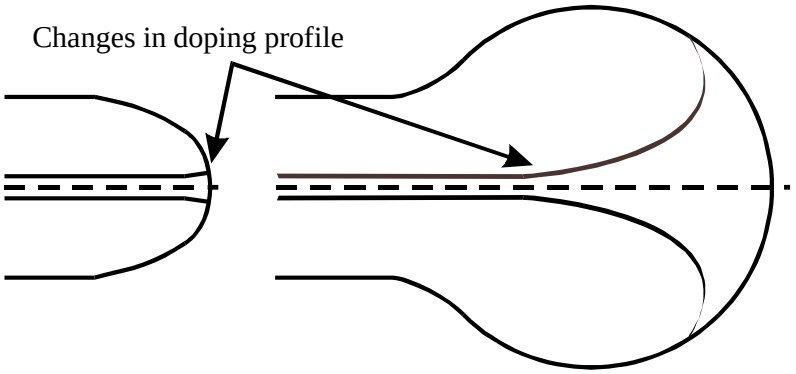

Fig. 5-6 Change of the doping profile due to melting

In contrast, the non-ground fibre retracts a quarter to a half millimetre upon melting with an immense change in the doping profile. Fig. 5-6 shows the assumed doping profile after the melting process. Both fibre types can be reproduced. The advantage of the recently melted glass fibre is that there is only one production step. However, if the glass fibre has to be threaded into a small hole, as shown in the left side of Fig. 5-5 (a wire eroded fibre holder with a 127-µm hole), the ground and melted fibre is favoured.

Thus, the new beam deflection system consists of a laser, driven in the LED mode, a ground and melted glass fibre, with an additional lens to focus light into the fibre, and on the pigtail output side a match-shaped fibre, with a lens to focus the light onto the cantilever.
A prism is required to combine the beam deflection light throughput to the cantilever with a normal incidence camera view of the cantilever and sample.

5.2 Beam guidance in the prism

The system has two cameras to image the cantilever and the sample position. One camera is placed at an angle of approximately 15° to the lateral sample position and is used, for example, to observe the approach of the cantilever onto the sample surface.
The second camera has a top view of the cantilever at a normal incidence to the sample. A prism is used to combine this top view of the second camera with the throughput of the light beam for the beam deflection system. In a temperature-controlled scanning force microscope, the beam of the deflection system is easier to handle in a solid glass body than in a gaseous medium because there is no ascending turbulent hot air to disturb the beam. The prism is constructed from two glass bodies, as shown in Fig. 5-7. To avoid the disadvantages inherent in using glass, the two glass bodies have to be made of ultra-low expansion (ULE) glass, which is stable against temperature tension, very homogeneous, and completely free of blowholes.

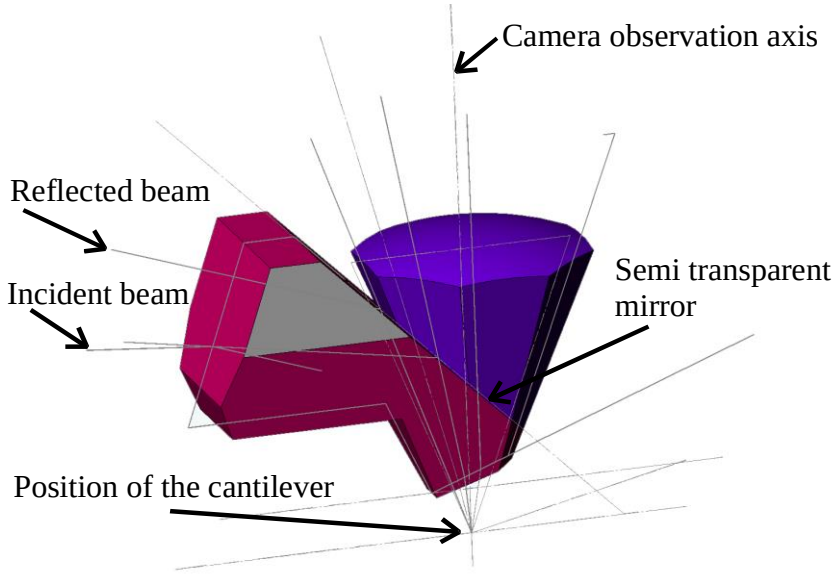

Fig. 5-7 Prism for combining the camera view and the light beam feedthrough

A small component is metallised in the region where the two bodies are glued together, as shown in Fig. 5-8, to mirror the incident and reflected beam of the deflection system to a certain position. The mirrored section is not a blind spot on the camera image because the mirror is not in the image plane of the camera focus. The camera, of course, loses light due to the shadowing effect of the reflective coating; however, there is only a small per-cent of light lost with this beam deflection system compared with other systems that use beam splitter cubes. Furthermore, the camera view is only a tool to help adjust and observe the sample. The important part of the camera is the beam deflection system, which guides the light to the cantilever and back to the 4Q-PD to the extent possible.

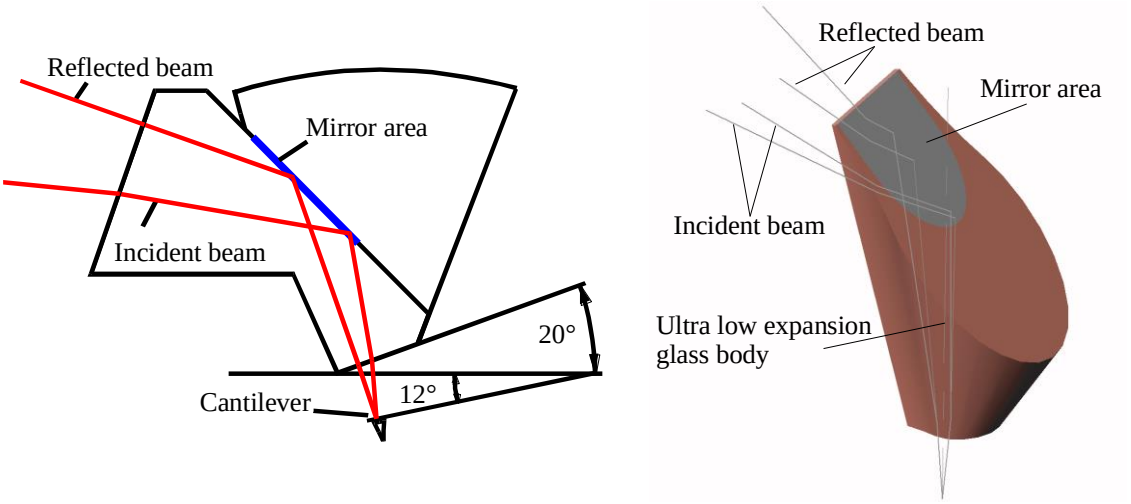

Fig. 5-8 Beam guidance inside the optical prism (left) and the mirror position (right)

This prism is used in the exchangeable service disc where the cantilever holder is mounted. The service disc is the upper cap of the encapsulated scan chamber. The wedge-shaped prism fits exactly into the service disc, minimising the effect of the thermal stack and preventing the escape of evaporated material of sample from the scan chamber. The cantilever has the usual tilt of 12° relative to the sample plane. The underside of the prism, which faces the cantilever, is tilted at 20° so that an angle of 8° occurs between the incident and reflected beam, enabling a better separation between the beams. Thus, the reflected beam strikes the surface under 88-89°, minimising the loss of light. However, as the angle is not 90°, multiple reflections between the cantilever and glass body that would otherwise disturb the photodiode detection of the deflected beam are avoided. Minimising light losses is important because light power cannot be increased at will due to the heating of the cantilever by the absorbed light[33].
Even light reflected from the sample surface cannot reach the 4Q-PD because of the 20° tilt of the underside of the prism. This results in an almost undisturbed beam deflection for detection by the 4Q-PD[30]. However, a misaligned beam produces a reflection from the sample surface that is observable in the optical microscope camera. The mechanism by which the beam of the deflection system is precisely adjusted onto the cantilever is the topic of the following section.

5.3 Precise positioning of the beam onto the cantilever and the photo detector

Measuring the interaction of cantilever and beam requires a very precise measurement apparatus. First, the beam must be positioned at the end of the cantilever. Every change of the cantilever requires a new beam adjustment because the position of the new cantilever may not be exactly the same as before and alterations in the cantilever size also re-position the cantilever.
For x- and z- positioning, piezo walker motors are used. The walker motors have a precise motion and can be locked into stability against outer mechanical impact. This fulfils the highest requirements for mechanical and drift stability.
Misalignment of less than 1° in the production of the fibre pigtail, as discussed in chapter 5.1, is adjusted using the static angle slide, as shown in the figure above. Therefore, the beam leaves the X-, Z- slide in the x-, z- central position where the beam is adjusted to the typical working position of a non-deformed cantilever.
The X-walker motor can now adjust the beam across the width of the cantilever. The y-motion of the beam along the length of the cantilever is performed by the Z-drive because the z-motion is reflected in the mirror in the prism (see last section) and transformed to a y-motion.

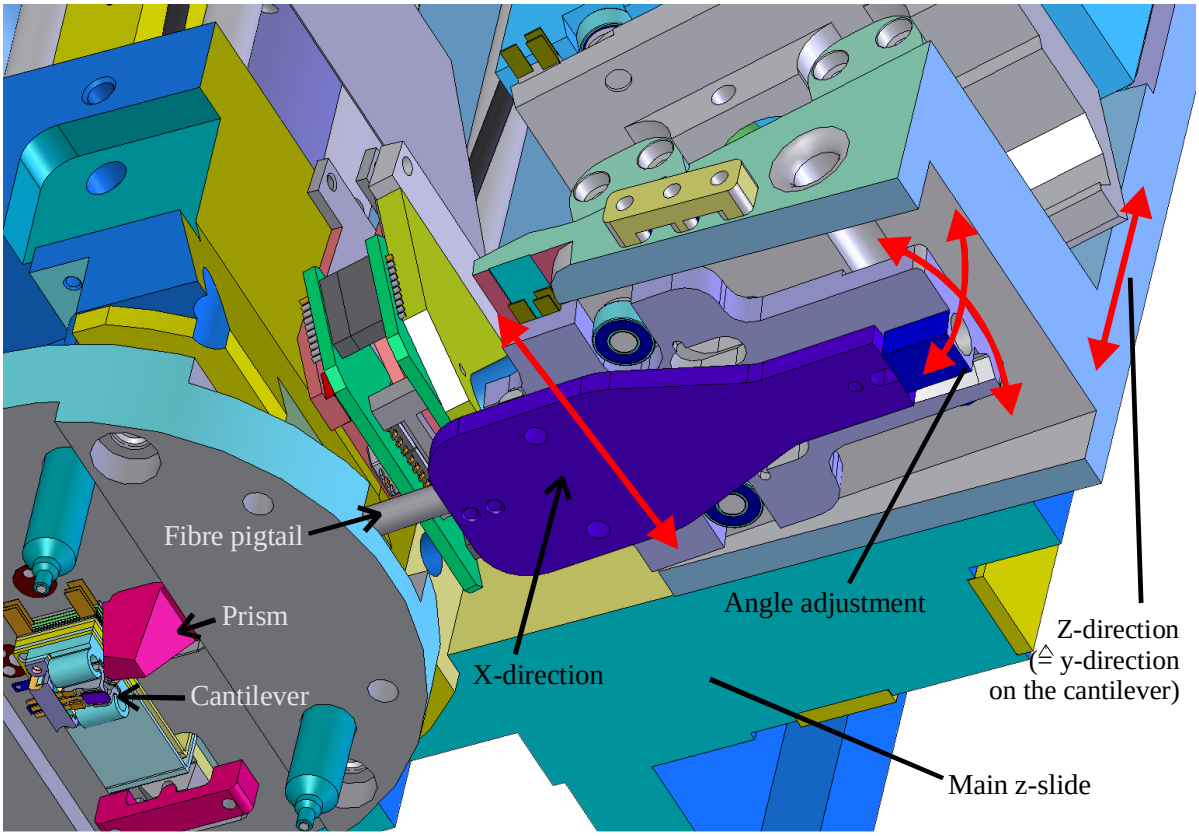

Fig. 5-9 X- and z-dynamic slides and a static angle slide for the beam to cantilever adjustment

After the adjustment of the beam to the cantilever, the photo detector must be moved to a specific position to collect the beam such that there is maximum separation of the lateral and normal motions of the cantilever. The next chapter describes the adjustment of the 4Q-PD by an additional rotation setting to improve this signal separation.

5.4 Adjustment of the 4-quadrant photodiode in all 3 spatial dimensions and adjustment of the tilt angle

The 4Q-PD will be adjusted similarly to the fibre pigtail. This system has four walker motors, two for x- and z-adjustment, one for moving forwards and backwards and one for rotation, to separate the lateral and normal signal.
As mentioned above, the cantilevers are not equal and bonding to the holder is an additional source of error. Thus, even the 4Q-PD has to be adjusted after a cantilever change. The x-adjustment works similarly to the beam pigtail adjustment, except that the detector Z-slide is mounted on the common Z-slide, which moves the beam pigtail (shown in Fig. 5-10). This construction reduces the work needed for calibration. If the pigtail is moved in the z-direction, the 4Q-PD is moved in the same way and the beam should remain in same position on the photodiode.
Fig. 5-10 shows the two Z-slides. With help of the springs, a high force is loaded onto the Z-piezo walker motor, leading to high stiffness of the motor. The springs must be strongly elongated to minimise force variations during the walking process. Furthermore, as can be seen from Fig. 5-10, the springs are tilted out of the horizontal plane to compensate for the effect of gravity on the mass and to ensure a constant velocity during motion.

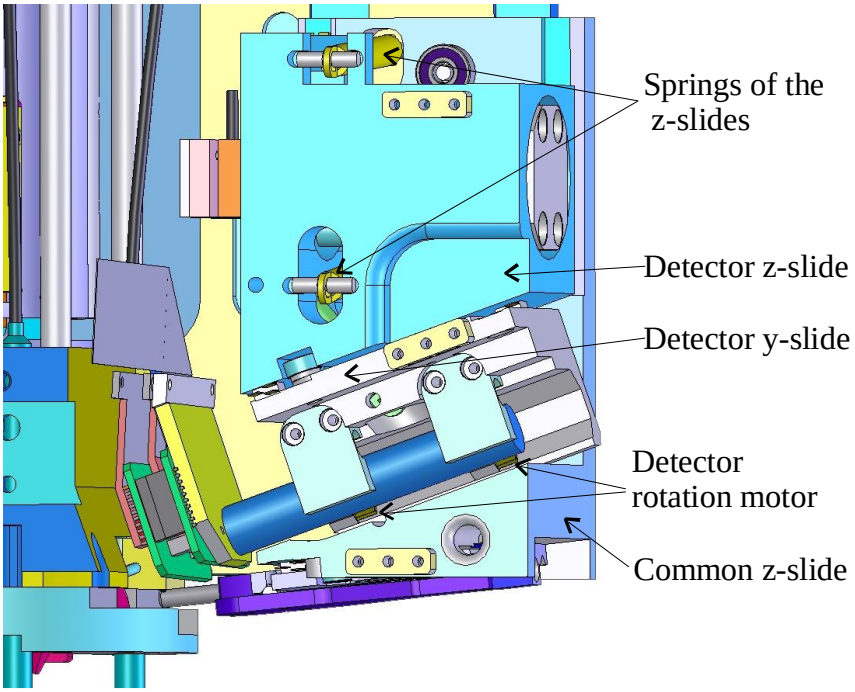

Fig. 5-10 Combination of two z-slides for the beam pigtail and detector

Upon adjustment of the x- and z-axis, the 4Q-PD can be moved back and forth along its own axis to optimise the spot diameter (see Fig. 5-11) and the deflection sensitivity.

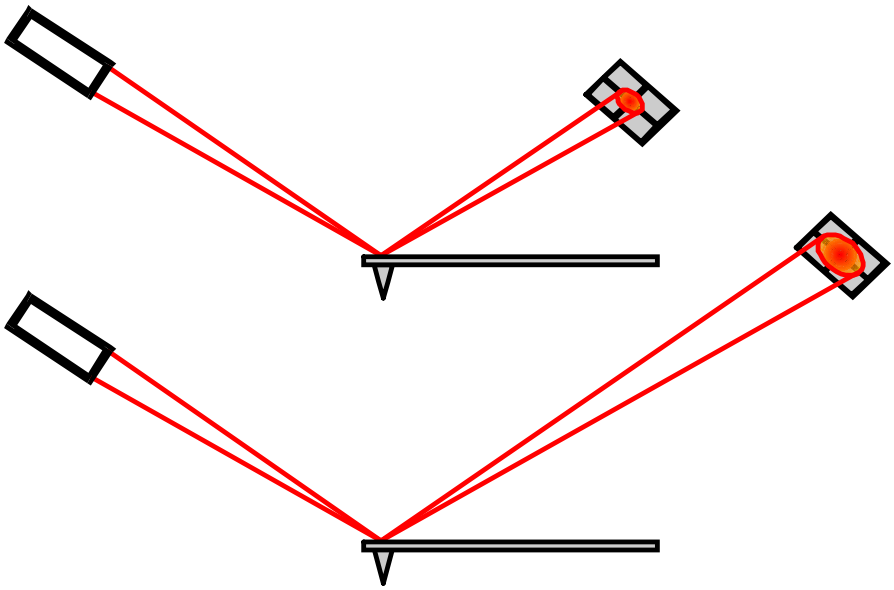
Fig. 5-11 In-axis optimisation of the beam spot diameter on the 4Q-PD

The lever amplification of the system only takes place if the beam is nearly parallel. The amplification follows from the theorem of intersecting lines, so that doubling the distance results in a doubling of the beam motion on the 4Q-PD. However, if the beam is not parallel and the beam diameter doubles in diameter, there is no effect and no increase in amplification.
To reduce light dissipation from lever amplification with a divergent beam, a four-quadrant lens helps to focus light onto each of the four photodiodes. This four-lens array, as shown in Fig. 5-12, has an advantage in addition to reducing the divergence: the influence of the gap of the 4Q-PD can be minimised or even cancelled. Therefore, the sensitivity within the gap area is increased.

With a ±2.5 mm travel range of the slide and a mean distance of 50 mm between the cantilever and the 4Q-PD detector, a 10% change in the sensitivity is possible. The nearest position with the shortest distance is useful for measuring force distance curves where high deviation of the cantilever at low resolution is needed. Using the furthest position provides the highest sensitivity at low deviation of the cantilever and is recommended for high-resolution images of samples with minor roughness.

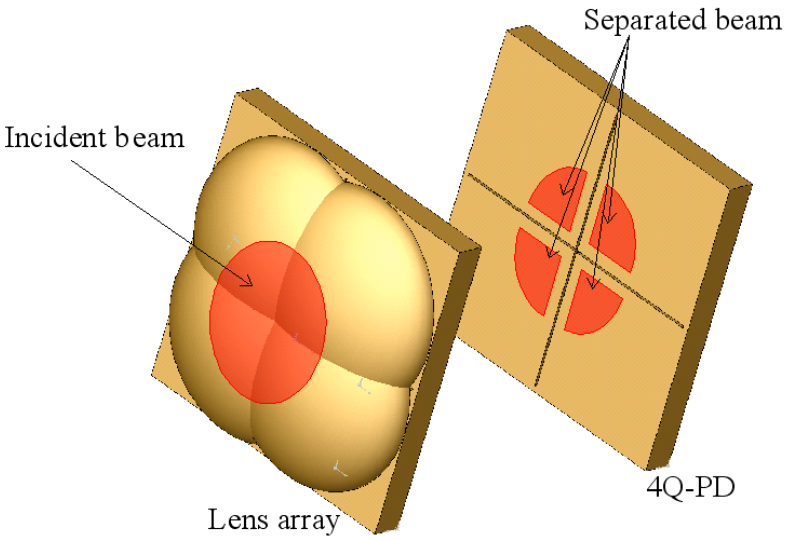

Fig. 5-12 Four-lens array for beam alignment in front of the 4Q-PD

The exact separation of the lateral and normal motions and their signals is important in friction measurements, necessitating a tilt correction. Fig. 5-18 and Fig. 5-20 in the next chapter show the normal and lateral thermal resonance of different cantilevers. The normal force resonance is only present in the normal force signal, which is known as the T-B signal (T-B = top minus bottom signal of the 4Q-PD). In contrast, the lateral force resonance is observable in both the lateral force signal, which is known as the L-R signal (L-R = left minus right), and in the T-B signal. This behaviour depends on the unsymmetrical setup of the lateral motion and on the tip mass being off the lateral symmetrical axis. Thus, the normal force cannot be completely removed, but the 4Q-PD should be rotated so that the normal component of the lateral moving signal is as small as possible. The rotation along the axis with a piezo walker motor can reduce the cross talk between the normal and lateral motion of the cantilever but cannot remove the unsymmetrical behaviour of an improperly glued cantilever.

5.5 Detection of the cantilever reflected beam by the 4-quadrant photodiode

A position-sensitive photo detector, in terms of the beam deflection, detects the motion of the cantilever. Common detectors for such beam deflection systems are the photosensitive detector (PSD) and the four-quadrant photodiode (4Q-PD). Different constructions of PSDs are possible. In a duo-lateral type PSD, a photosensitive barrier layer separates two resistive layers. The resistive layers each have two spatially opposite electrodes, where the electrodes in the lower layer are rotated 90° relative to the upper resistive layer. Therefore, a light spot generates a photocurrent in the barrier layer: this current is divided between the two resistive layers according to Kirchhoff's law. The ratio between the individual currents provides direct information on the "centroid" of the light spot. This type of position measurement has the advantage of being independent of the shape of the light spot, as long as the shape is constant. Additionally,

high linearity is typical with a suitable quality resistive layer. The electric current is converted to voltage by an electric current voltage converter. The position sensitivity depends on the length of the working area of the PSD. In the case of a voltage range of ±10V and a working distance of ±5 mm, a sensitivity of 2V/mm can be calculated. However, a 4Q-PD has a substantially higher sensitivity in the central crossover region (for example, 220V/mm with 10 µW light power and a spot size of approximately 100 µm). A higher positioning sensitivity can be achieved if the offset zoom principle is also used, so that the noise depends essentially on the light intensity[30] and the reference voltage.

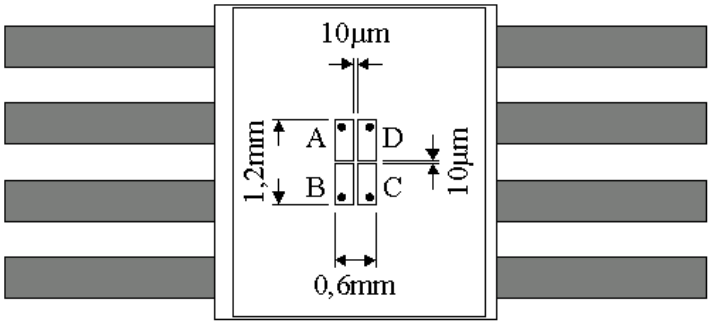

Fig. 5-13 Schematic of a 4-quadrant photodiode (Hamamatsu S6058)

In contrast, the 4Q-PD consists of a homogeneous photosensitive barrier layer covered by four symmetrical, translucent metal electrodes. To measure the four photocurrents, a gap is placed in between the four metal electrodes (an area that is not vaporised) as shown in Fig. 5-13.
If the light spot moves on the 4Q-PD, the individual photocurrents and the corresponding voltages of the four individual quadrants change. The T-B signal is determined by the difference between the two upper and lower photodiode pairs:

$$U_N = (U_A + U_D) - (U_B + U_C) \qquad \text{Eq. 5-2}$$

The subscripts of the last and following equation are derived from Fig. 5-13. The L-R signal is given by the difference of the two lateral photodiode pairs:

$$U_L = (U_A + U_B) - (U_C + U_D) \qquad \text{Eq. 5-3}$$

However, the modification depends on the shape of the light spot and on the size of the gap between the electrodes. Fig. 5-14 shows this behaviour for the one-dimensional case. It can be seen that the sensitivity depends on the beam shape[34].
Unfortunately, the beam shape can only be optimised to a limited degree in practice because the reflection layer of the cantilever dominates the light beam. Nevertheless, in contrast to the PSD case, higher sensitivity (220V/mm) is available in the zero crossing of the 4Q-PD using a light spot diameter of 60 µm, a Gaussian shaped profile and a 10 µW light power source. Fig. 5-15 shows the sensitivity measured for two different 4Q-PDs and three different spot sizes.
In addition to minimising the gap, the light intensity should be maximised. The 4Q-PDs (S6058 and S6242) from Hamamatsu used here have a gap of only 10 µm, while the S6695-01 has a gap of 15 µm. However, a light spot in the 100-µm diameter range, crossing the gap, has a noticeable effect on the sum signal (Fig. 5-16). As mentioned above, the light within the gap can be deflected to the active diode areas by using a quadrinomial micro lens (see Fig. 5-12), so a constant light power can be used even with a smaller light spot.

In general, the beam is adjusted to give a T-B signal that is zero or close to zero. The normal force feedback tries to hold this position fixed. Due to this fact, high sensitivity is more important than the linearity for the detection system. It is essential for both the performance of the PSD (photosensitive detector) and the 4Q-PD that the sensitivity be directly proportional to the light intensity. To avoid measurement errors caused by light intensity fluctuations, the signal difference of the individual photodiode has to be divided by the signal sum, or the sum signal must be controlled by a feedback loop (as used in this system).

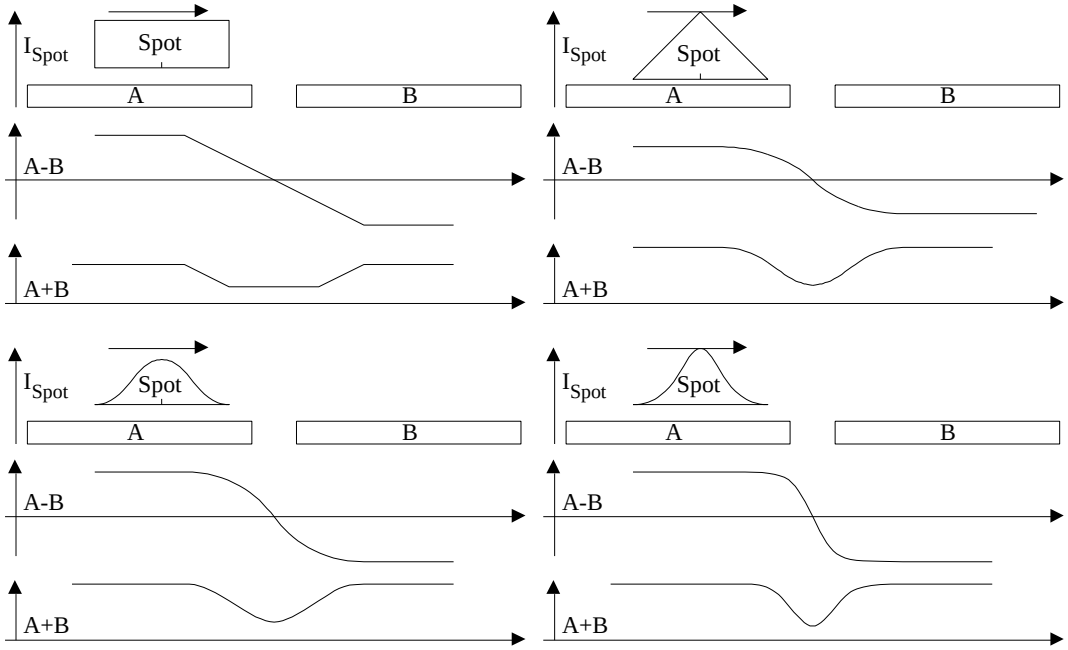

Fig. 5-14 The difference and sum signal of a double photodiode, depending on spot position and shape

This explains the error that arises when the light beam goes beyond the active surface area of both systems. The integral light decreases and a fault position is given by the PSD as well as the 4Q-PD detection system. This error increases until the light beam is strongly misaligned and off the active area of the both systems. In this situation, both systems give a signal of zero, which can be by mistake interpreted as a well-aligned system.

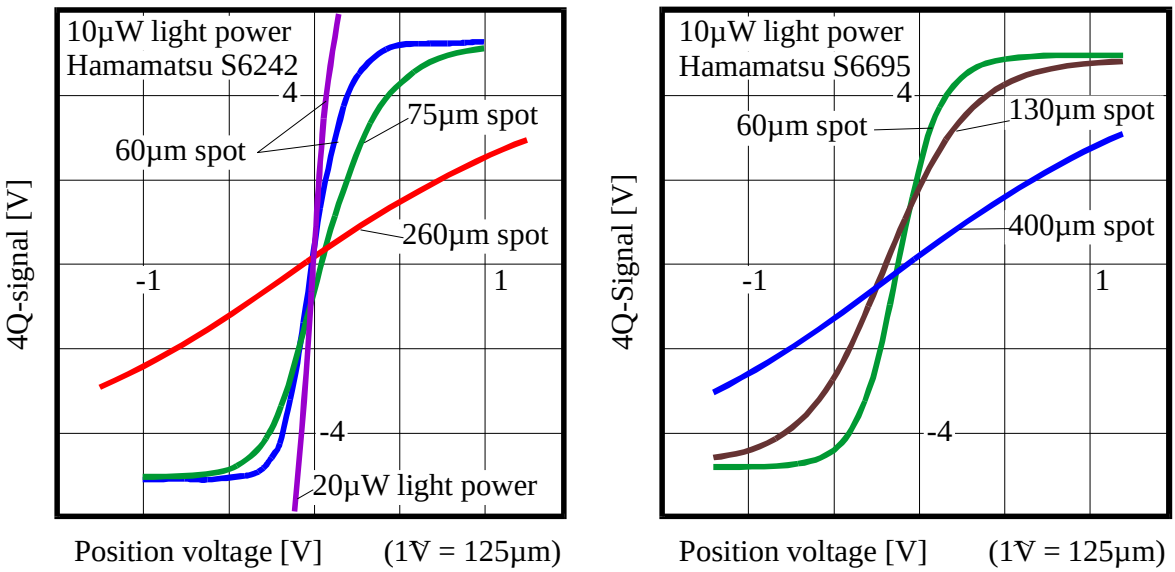

Fig. 5-15 Measured differential voltage T-B signal from two different 4Q-PDs for different spot sizes

The 4Q-PD has to be adapted to the size of the light spot and the dynamic positioning range. However, the diode areas should be as small as possible (which assumes a small light spot diameter) to minimise the dark current and the barrier capacitance. The dark current only generates an offset but the barrier capacitance lowers the bandwidth in two different ways:

1. if a resistor is connected in parallel to the photodiode, the voltage corresponds to the photocurrent multiplied by the resistance value
2. the barrier capacitance is parallel to the resistance and directly affects the cut-off frequency which is given below

$$f_{cut-off} = \frac{1}{2\pi R C_{barrier}} \qquad \text{Eq. 5-4}$$

If an operational amplifier (OP) with voltage feedback reads out the photodiode, then the barrier capacitance is located at the input of the OP and must be compensated for by an additional capacitor of the same size in the feedback to provide stable operation. The increase of the feedback capacitance directly lowers the bandwidth of the OP circuit of the current/voltage converter.

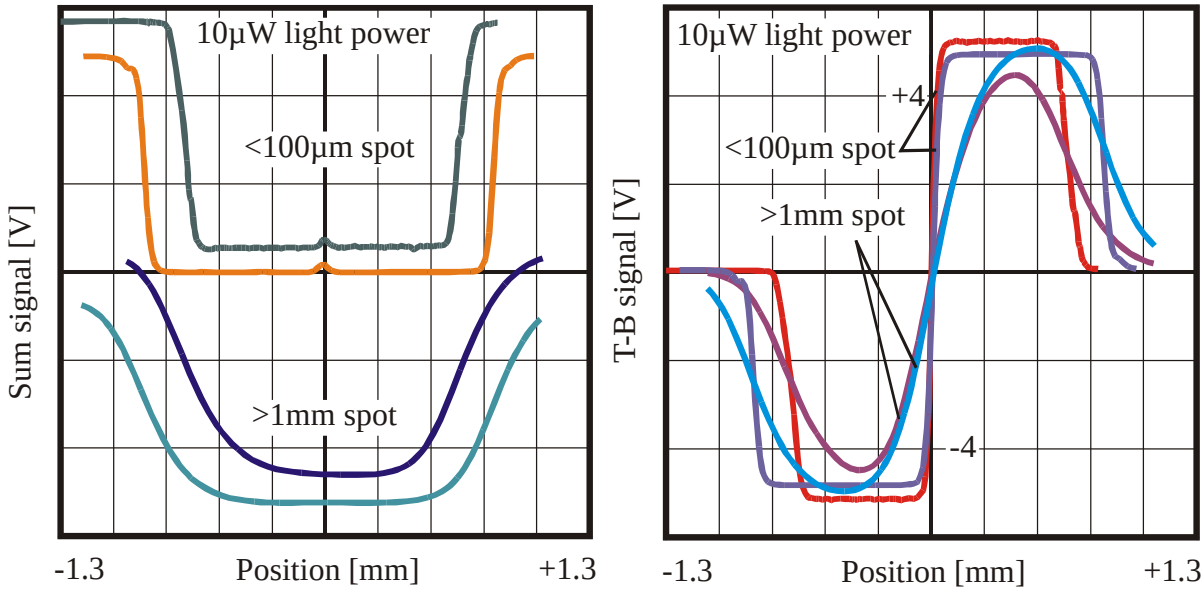

Fig. 5-16 Measurements of the sum (left) and T-B signal (right) of a light spot with varying diameter crossing two different 4Q-PDs

Applying a reverse voltage to the photodiode results in an increase of the space-charge region and a reduction in the barrier capacitance. A reverse voltage of 10 V applied to the photodiode S6058 reduces the diode capacity from 2 pF to 0.9 pF. This also causes a reduction in the feedback capacitance by the same factor. In the case of a light power of 200 µW for the 4Q-PD (50 µW per diode area) and a sensitivity of 0.5 $^{A}/_{W}$, a diode current of 25 µA per quadrant (for a light spot in the centre of the 4Q-PD) is expected. A feedback resistance of 200 kΩ (10 V amplitude) results in a cut-off frequency (@ -3 dB) of approximately 400 kHz. Other OPs are stable with gain 1 without a feedback capacitor (even with a load of 1 nF) so that the cut-off frequency rises to 800 kHz.
During the operation of a scanning force microscope, the light spot only moves a small amount on the 4Q-PD so that the light current is subject to only low fluctuations, which correspond to the measured signal. Therefore, a small fluctuation around a large signal value needs to be measured. As the signal is small, the OP should operate with as large a feedback resistance as

possible to maintain a high sensitivity. The current/voltage converter has to operate at the limit of its voltage supply that strongly reduces the dynamic range. To optimise the dynamics and sensitivity of the preamplifier, the offset zoom principle must be used. Generally, a bias current subtracts the offset of the light signal and a higher feedback resistor extends the output signal to a maximum value corresponding to the maximum motion of the light spot on the 4Q-PD. The filtering of the bias voltage is important because the noise of the bias source is amplified at the same level as the volitional signal. Therefore, the bias voltage must be filtered to less than 1 Hz to eliminate both the white noise and the $^{1}/_{f}$ noise.

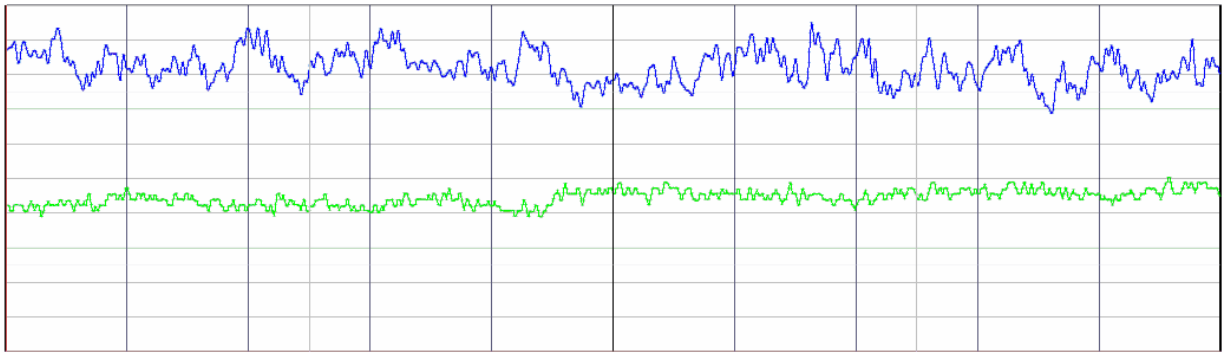

Fig. 5-17 The noise of the T-B signal (top) and the sum signal (bottom) @ 10 µW light power, 10 kHz low-pass, 3 $^{mV}/_{div}$ and a 20 ms time frame

The noise of the 4Q-PD is a combination of the thermal noise (also known as Johnson noise) and the shot noise of the dark current and the photocurrent:

$$I_{PD} = \sqrt{I_{JN}^2 + I_{SNDark}^2 + I_{SNPhoto}^2} \qquad \text{Eq. 5-5}$$

The shot noise is produced by carriers, which overcome a barrier depending on the current flowing through the material and the material properties as follows[35]:

$$I_{SN} = \sqrt{2eI_{dc}\Delta f_{BW}} \qquad \text{Eq. 5-6}$$

For low noise photodiodes, the NEP sums the thermal and shot noise at a certain block voltage and is divided by the maximum sensitivity.

$$NEP\left[{}^{W}/_{\sqrt{Hz}}\right] = \frac{Current\ noise\left[{}^{A}/_{\sqrt{Hz}}\right]}{Sensitivity\ at\ \lambda_p\left[{}^{A}/_{W}\right]} \qquad \text{Eq. 5-7}$$

The NEP of the S6058 4Q-PD used here is 6.5 10^{-15} $^{W}/_{\sqrt{Hz}}$ at a block voltage of 3 V. With a sensitivity of 0.5 $^{A}/_{W}$, a noise current of 3.25 $^{fA}/_{\sqrt{Hz}}$ is calculated. This value is 5 times higher than the noise of the OP602 that is used in this layout. Therefore, a high photocurrent is necessary because the shot noise only increases as the square root of the photocurrent.
The upper curve of Fig. 5-17 shows approximately 10 mV noise for the T-B signal. Consider as a worst-case scenario for the SFM system presented here that the cantilever is 500 µm long and that the distance between the cantilever and the detector is 50 mm. From Eq. 5-8, the slope for the light beam at the end of the clamped cantilever depends quadratically on the cantilever length[36].

$$f'(x) = \tan(\alpha) = \frac{F \cdot x^3}{6 \cdot E_m \cdot I} \frac{d}{dx} \xrightarrow{x=l} f'(l) = \tan(\alpha) = \frac{F \cdot l^2}{2 \cdot E_m \cdot I} \qquad \text{Eq. 5-8}$$

Using the values given above results in a gain of 400. For a sensitivity measurement of 220 $^{mV}/_{\mu m}$ in the zero crossing of the 4Q-PD, the noise is 0.114 nm_{pp}. Using a low-pass filter of 10 kHz, the noise is 1.14 $^{pm}/_{\sqrt{Hz}}$. Increasing the light power from 10 µW to 100 µW reduces the noise to 0.036 nm_{pp}. Thus, a low-pass filter can be dispensed with.
To improve the stability of the set point, a NTC (negative temperature coefficient) resistor is used as a temperature control on the preamplifier board. The board temperature is controlled by a Peltier element, which reduces the temperature drift of the electronic circuit, as well as the mechanical drift, which depends on the temperature. Thus, a long-term stable system that can produce a series of images under dynamically changing temperature conditions is obtained.
To demonstrate the sensitivity of the system, Fig. 5-18 and Fig. 5-20 show a frequency spectrum of a noise measurement. Both the basic and higher harmonic modes of the thermally stimulated resonances of the different cantilevers can be seen.

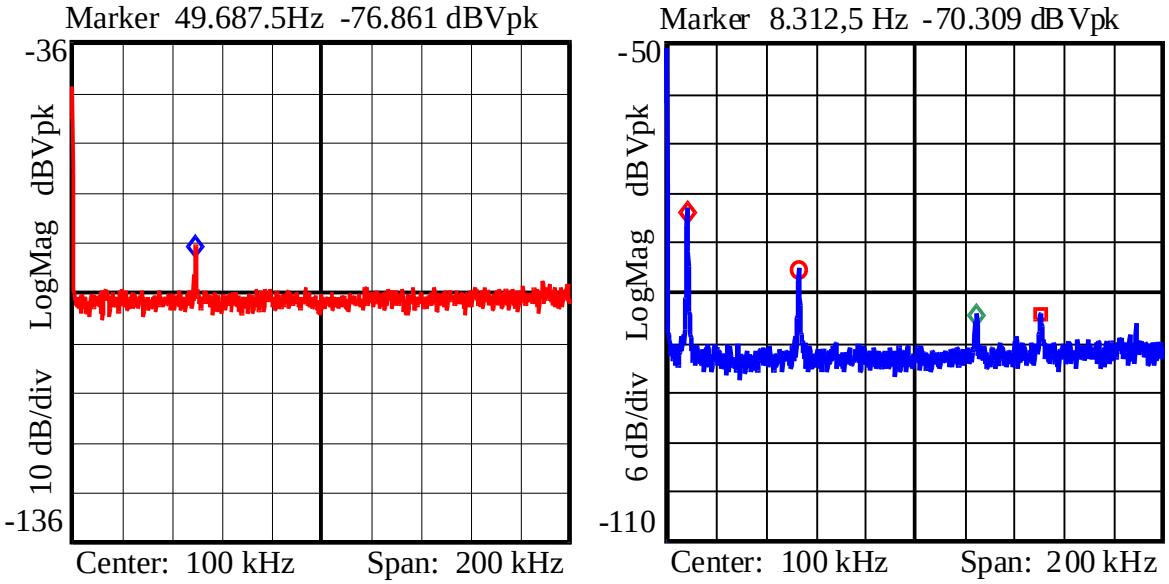

Fig. 5-18 The thermally excited normal force signal of (left) an intermittent mode cantilever and (right) a contact mode cantilever (average magnification x10 each)

The high quality factor of the cantilever system facilitates this characterisation. The right side of Fig. 5-18 shows the fundamental flexural resonance frequency of a contact cantilever at 8.3 kHz (red diamond marker): the first (red circle marker) and second (red square maker) flexural resonance at approximately 52 kHz and 149 kHz, respectively, can be observed to the right of the fundamental frequency. These results coincide with the eigenvalues calculated from the Euler-Bernoulli equation for a flexible beam clamped to an inelastic base. The eigenvalues are described as follows:

$$\frac{f_{nhm}}{f_{fm}} = \frac{(\alpha_n L)^2}{(\alpha_1 L)^2} \qquad \text{Eq. 5-9}$$

where f_{fm} is the fundamental mode and f_{nhm} is the nth harmonic mode of the resonance frequency. $\alpha_1 L$ is the first eigenvalue of the Euler-Bernoulli equation and $\alpha_n L$ is the nth eigenvalue corresponding to the nth harmonic frequency mode. Solution of the Euler-Bernoulli equation produces eigenvalues that can be used to identify the harmonic modes in a spectrum of a mixture

of different harmonic resonance frequencies of the cantilever and other resonance phenomena from other sources in the system, without exact knowledge of the cantilever size. The following table shows the fundamental and the first four higher modes for the cantilever corresponding to the measurements presented above.

nth mode	0	1	2	3	4
$\alpha_n L$ / $\alpha_1 L$	1.000	6.2669	17.5476	34.3860	56.8431
Frequency (kHz)	8,313	52.093	145.864	285.833	472.508

A finite element method calculation reproduces the measured results (see Fig. 5-19). The green diamond marker, on the right side of Fig. 5-18, indicates the normal component of the torsional deflection of the cantilever because the mass of the cantilever tip has moved off the axis of the centre-of-mass of the cantilever bar. A tilted cantilever assembly and/or unsymmetrical behaviour of the resistors in the amplification circuit cause this normal force component of the 124 kHz signal.

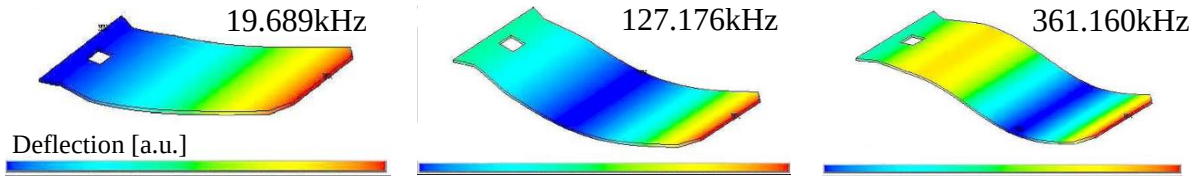

Fig. 5-19 FEM simulation of a dynamic cantilever deflection (basic, first and second mode)[37]

The lateral motion of the cantilever is shown in Fig. 5-20. The blue diamond in the left diagram marks the 124 kHz peak of the lateral component of the torsional motion. Even the resonance peak on the far left of the left-hand side diagram is a component of the basic normal force resonance frequency and has similarly originated from the tilted assembly of the cantilever and/or the unsymmetrical behaviour of the resistors within the preamplifier circuit. The right graph shows again the basic lateral component of the torsional resonance frequency as the highest peak, and the small, but visible, second harmonic of the lateral resonance frequency, marked by the red diamond.

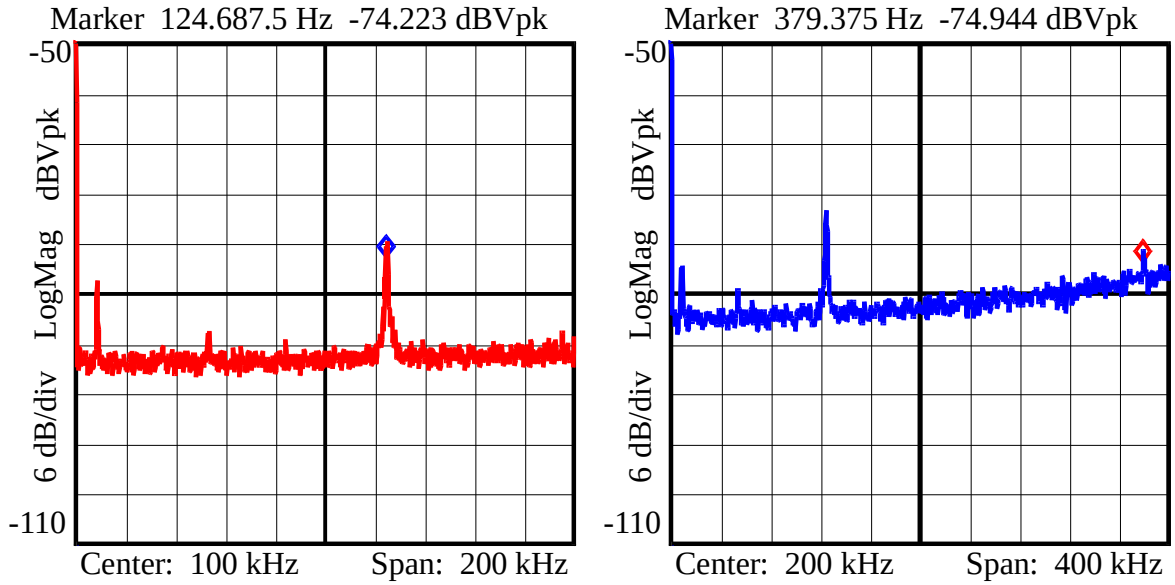

Fig. 5-20 Thermally excited lateral force signal of a contact mode cantilever: (left) basic resonance, (right) basic resonance and second harmonic (average magnification x20 each)

A further modification for the cantilever detection is the bias current subtraction directly before the first preamplifier stage of the 4Q-PD (Fig. 5-21). The figure shows a preamplifier with the bias current subtraction for one element of the 4Q-PD. The bias current is as large as the photocurrent from the 4Q-PD element during normal illumination of the beam. This procedure eliminates the dark current and consequently, the offset for the light signal. Thus, the gain can be increased to improve the signal-to-noise ratio and increase detection sensitivity.

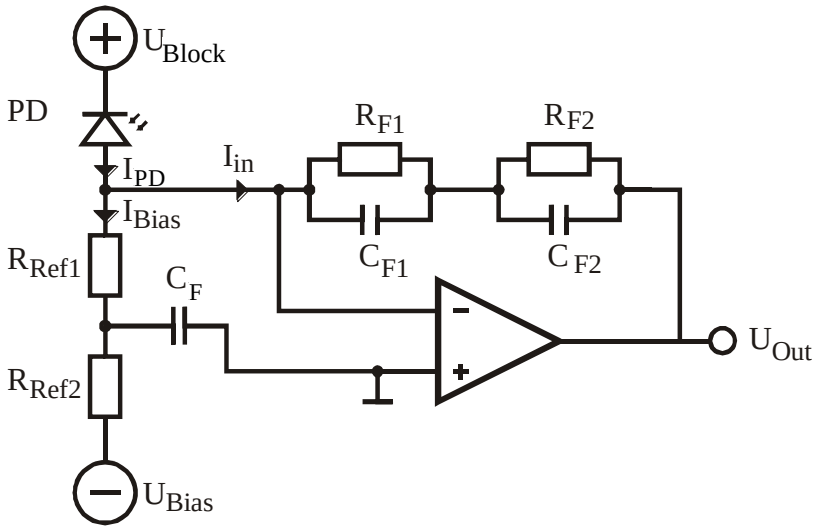

Fig. 5-21 PD bias current subtraction to produce a higher gain at the preamplifier

Following the detailed setup description of the z-detection unit, the lateral fine adjustment of the sample and the lateral and normal motion of the sample during the scan is the topic of the next chapter.

6 3-axes positioning and scan unit

The SFM system consists of a coarse positioning unit to place the sample under the tip and the scan unit. The coarse positioning of the sample is implemented via a piezo walker motor setup (Fig. 6-1). The yellow portions of both the left and right images show the same cross guidance which helps to guide the coarse positioning unit walking in x,y-direction and to avoid rotation caused by unequal step sizes of the different piezos. Actual positioning is controlled by a PSD (range ±2.5 mm, resolution below 2 µm). A PSD is used to provide an absolute value for the position of the sample even after a system power failure.

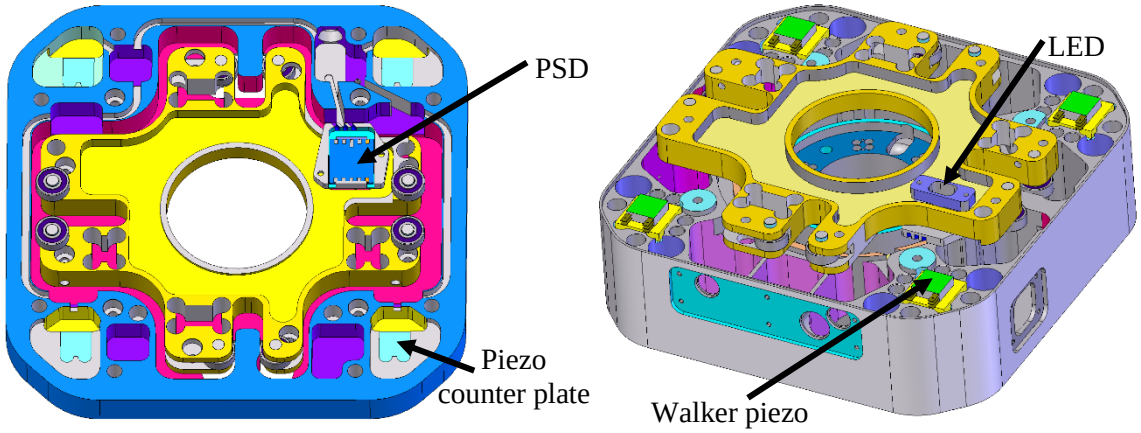

Fig. 6-1 Lateral coarse positioning unit with PSD: lower part (left), upper part upside down (right)

For a large scan range, all relevant components of the system must be several times faster than in currently available SFMs. Most SFM systems have a 200-µm or less scan range and a sample rate between 100 kHz to a few 100 kHz. The novel system has a 1000-µm lateral scan range and requires a sample rate of 1 MHz to be competitive with other systems. This section describes in detail the new solutions that fulfil this requirement.

6.1 Z-direction unit splitting to optimise the motion dynamic and plane subtraction

For the microscope described here, with a heating system and active sample vibration for friction experiments, the z-direction has the highest dynamic requirements. The heating system and vibration piezos must be moved in addition to the standard sample holder and sample. First, the Z-drive (as well as the XY-drive) is highly symmetrical to minimise temperature drift of the sample. Second, the additional force to move the heating elements and vibration piezos has to be provided by the Z-drive without disturbing the lateral motion due to restoring forces. The Z-speed has to be increased to compensate for the mismatch between the large scan range and precise and fast positioning. Therefore, the Z-drive is split into three parts: a low-frequency hydraulically driven component, a mid-range frequency component with piezo stacks and piezo compensation and a high-frequency piezo drive, also with piezo compensation. This frequency band separation facilitates the required speed and accuracy needed for constant-force microscopy.

The low-frequency hydraulically driven component has a range of approximately 300 µm, with a maximum frequency of 10 Hz for a 150-µm stroke. This part of the Z-drive is used to compensate for the sample tilt. The piezos are not stiff enough with respect to the setup of the mid-

range and high frequency Z-drive and therefore, the mass that uses the low frequency drive to move. The solution to this problem is to use an array of pressure cells as shown in Fig. 6-3.

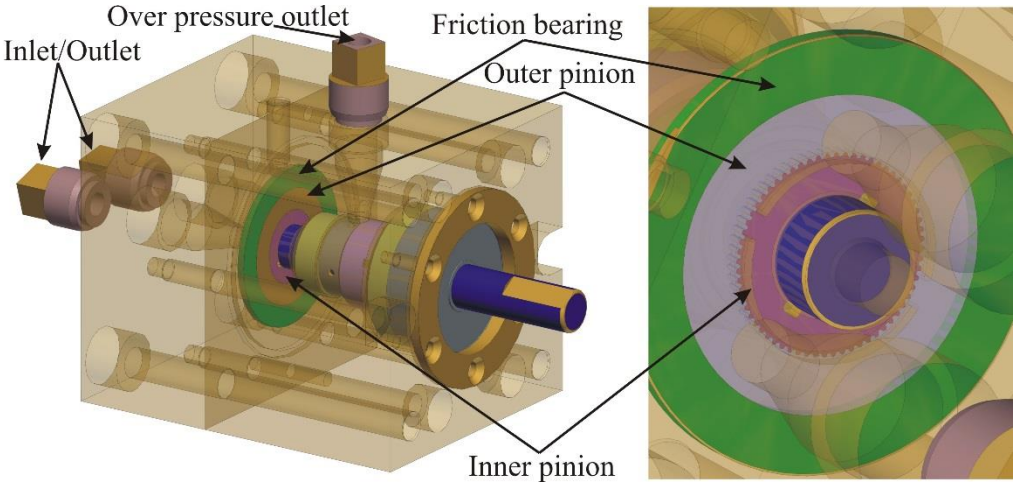

Fig. 6-2 Micro-gear pump (left) and gear for the pump produced with an wire-eroding machine(right)

Four independent working, micro-gear pumps feed the four pressure cells. This type of pump can produce a continuous flow in both directions, depending on the direction of the motor driving the pump, while the pulsation is proportional to the volume between two teeth of the gear of the pump. As sub-nanometre resolution is required, a self-constructed gear pump is used (Fig. 6-2).

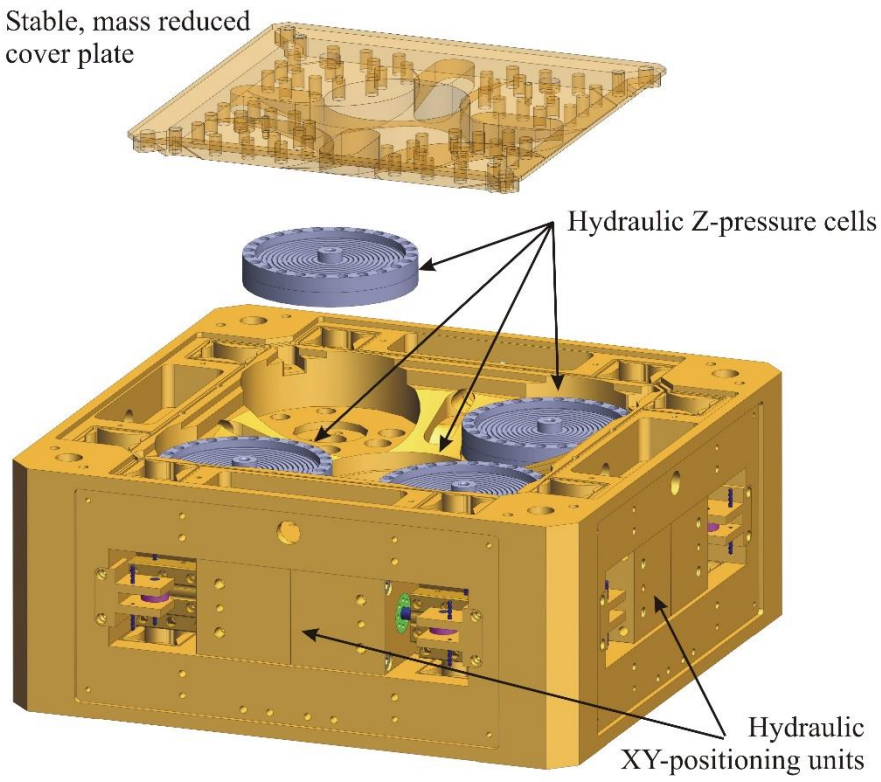

Fig. 6-3 Main casting with the four low frequency, hydraulic Z-cells and the low frequency cover plate mounted on the coarse positioning unit

The hydraulic cells are made of stainless steel because of the ductility of the material. The meander structure is the same inside and outside. Thus, the cell can be filled with hydraulic oil and a change in pressure results in an extension of the cell. It follows that the mid-range position causes a pressure higher than the ambient pressure. During a pull down of the scan head, this behaviour helps the pump from sucking the oil from the cell because the vapour pressure of the hydraulic oil avoids bubble formation.
The mid-range frequency component has a range of approximately 12 µm, with a permanent maximum frequency of 5 kHz for a 1-µm stroke, as shown in Fig. 6-4.

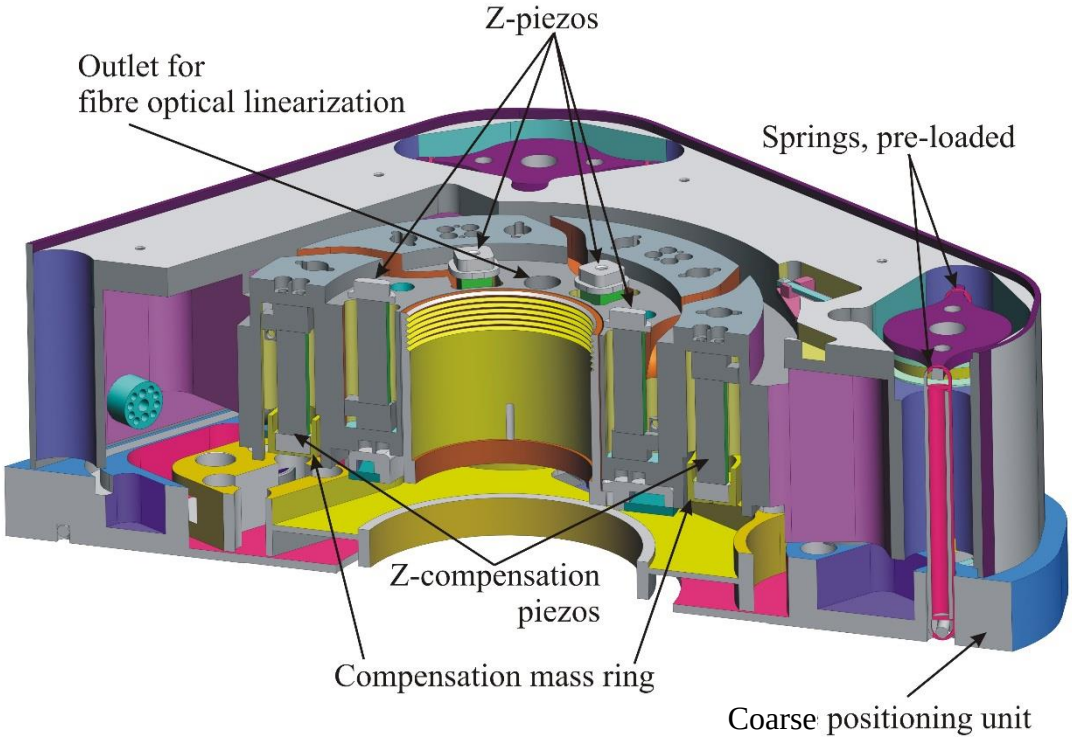

Fig. 6-4 Mid-range frequency piezo-driven and compensated Z-component

The figure shows the piezos for the sample motion, below which a second batch of equal piezos is connected to a mass ring. The motion of the mid-range Z-component is actively measured for the closed-loop operation and the lower set of piezos is controlled such that the mid-range mass is almost zero.
Finally, the high frequency Z-component has a 2-µm range and can work permanently at a 20 kHz frequency with a 0.5-µm stroke.
This mechanical Z-stack is controlled via the ECU (electronic control unit). The electronic scan module within the ECU that controls the three z-modules includes analogue temperature compensation and an analogue two dimensional plane subtraction, in addition to the analogue offset and zoom. As mentioned above, in addition to the dynamic requirements, the sample tilt must be compensated for to allow for large samples. The hydraulic low frequency Z-component can be used for this requirement. The four hydraulic cells can be treated separately. Therefore, the analogue plane subtraction can control the four independent gear pumps for the low frequency Z-component.

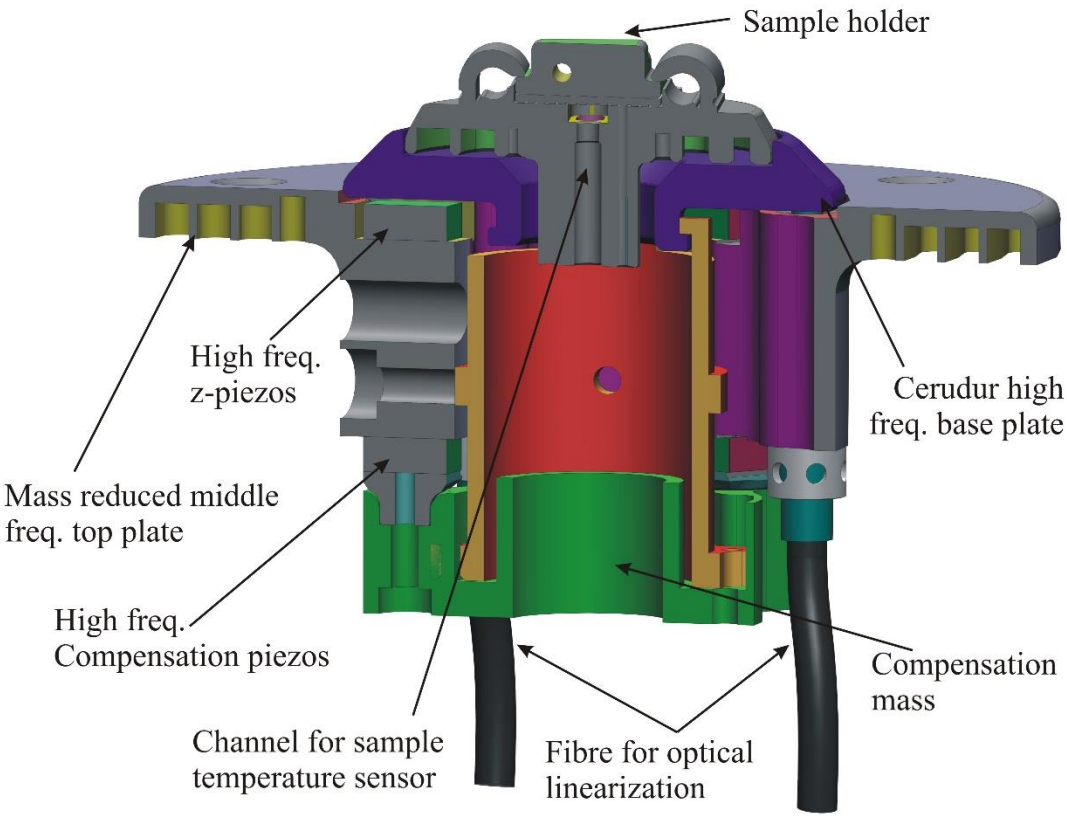

Fig. 6-5 High-frequency piezo-driven and compensated Z-component

Measurements for the overall scan module show a noise of less than 10 µV at a maximum input of ±10 V. The noise is calculated to be equivalent to 0.5 nm.

6.2 Hydraulic actuator for the lateral moving unit

The large scan range of approximately 1 mm, the heavy load, and a fast scan motion exclude the use of piezo elements as mechanical actuators for the lateral motion. Piezos appropriate for scanning force microscopes have a stroke of about a tenth of a micron. Higher strokes are possible but results in lower blocking forces or higher creep behaviour. For a scan range of approximately 1 mm, an up-gearing of the stroke is necessary. An up-gearing of the stroke results in a mechanically weak system and lead to an unstable microscope. Fast scan motions are no longer possible. A new hydraulic cylinder is especially constructed to establish a non-linear gain. The solution consists of a completely closed hydraulic system with a bi-directional cylinder, pressurised by an internal gear pump.
The advantage of this new design (as opposed to using conventional hydraulic actuators) is the removal of the gasket around the piston in the centre of Fig. 6-6. During standard operation in large machines, the gasket seals one oil chamber against the other so that no leakage leads to a position change when the pump is not working. The stick-slip effect of this gasket is too large for the novel microscope with nanometre resolution. Fig. 6-6 shows a symmetrical frictionally optimised hydraulic cylinder with a small bypass around the piston. This leads to a nearly friction-free movement of the piston.

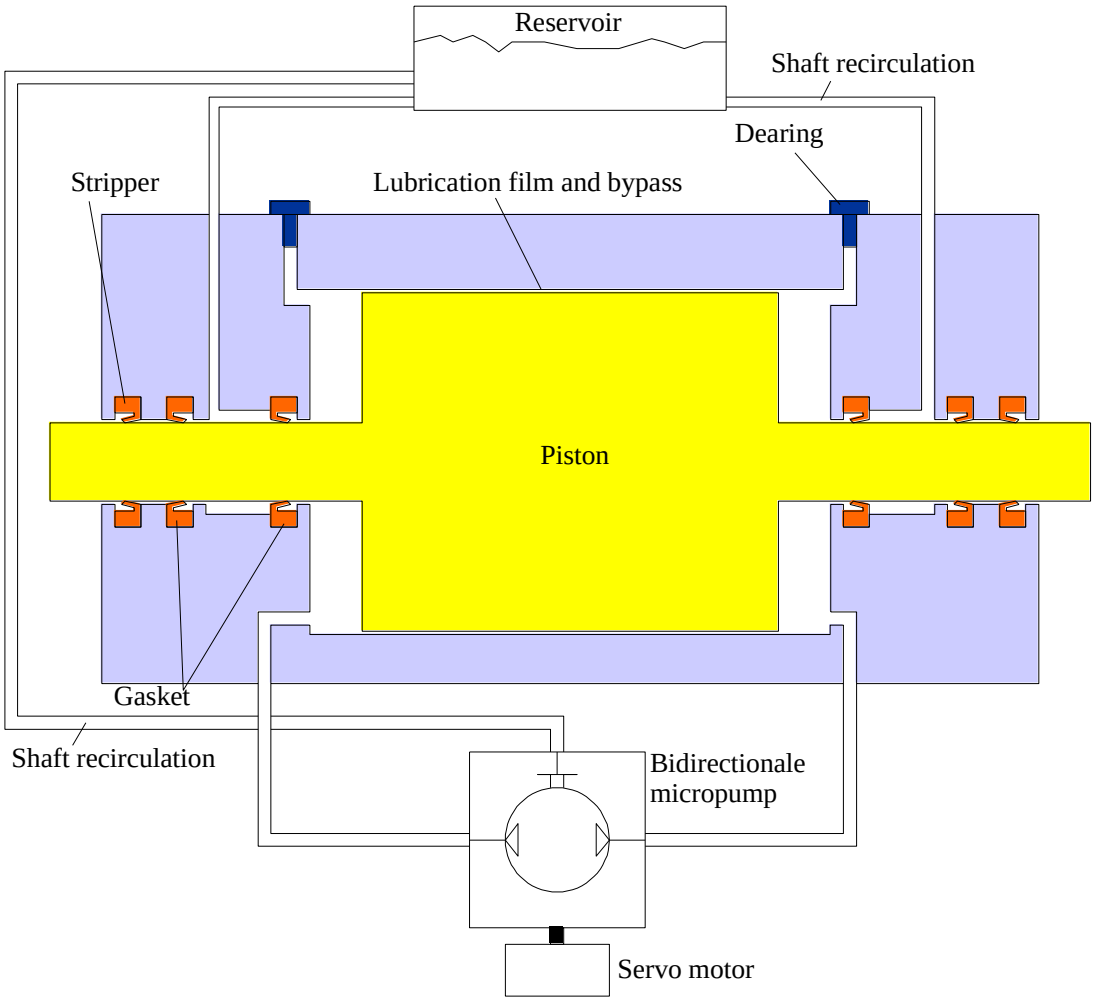

Fig. 6-6 Schematic of a symmetrical bi-directional hydraulic actuator (European patent pending[38])

The gaskets around the shafts in the lead troughs are lock-rings. These lock-rings have a contact area that is several times smaller than that for the gaskets around the piston. If the shafts are well polished, the friction is even less than that of the normal gaskets. The ducts between the lock-rings result in leakage of the hydraulic oil that is fed back to the reservoir. The reservoir has a partial pressure of approximately 200-300 mbar to avoid the permeation of air through the outermost lock-rings.

The new design, as shown in Fig. 6-7, has an effective piston area of 553 mm². This results in 553 N of force for a hydraulic pressure of 10 bars. This hydraulic pressure can easily be produced from a gear pump. The gap between the piston and the chamber wall is approximately 3-6 µm. Therefore, the piston slides on hydraulic oil lubrication film of the gap thickness. This gap acts as a bypass. If the micro pump works very slowly, the majority of the small amount of pumped oil flows through the bypass and the piston motion is in the nanometre range. If the micro pump works faster, the flow resistance within the gap increases: only a small part of the increased amount of oil can flow through the gap and so the piston moves faster. This non-linear behaviour between the micro-pump revolutions and the piston movement leads to the possibility of either a fine adjustment or a fast movement of the position, depending only on the speed of the pump.

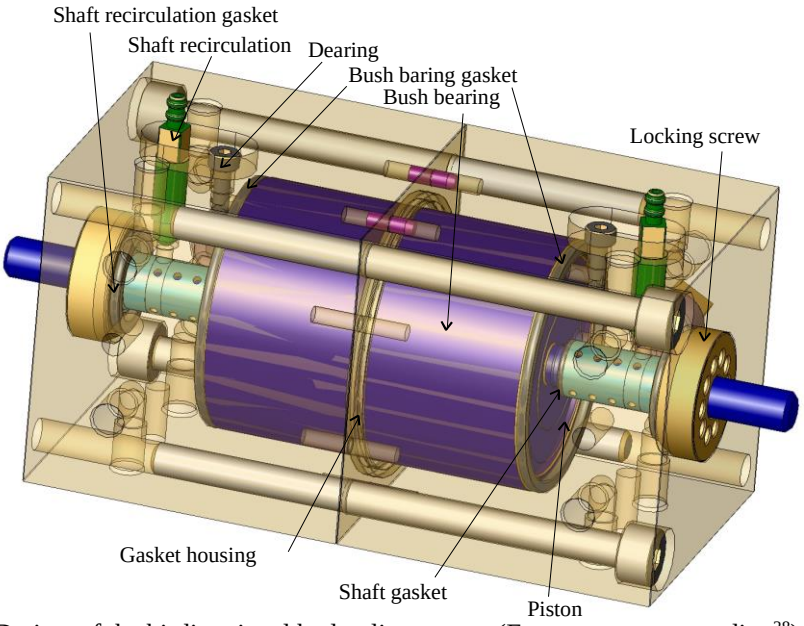

Fig. 6-7 3D view of the bi-directional hydraulic actuator (European patent pending[38])

6.3 Linearization of the 3-axes scan table

For a high-resolution scanning force microscope, a linearized piezo actuator positioning system is required to yield reproducible non-distorted images. Modern SFM methods sometimes need to pause at a measurement point to collect additional data. For manipulation methods such as lithographic techniques, a controlled positioning system is required. The hysteresis and creep typically found in piezo-driven drives also need to be prevented. In temperature-controlled experiments, the disadvantageous effect of the piezos is amplified by a temperature rise making linearization even more necessary. With the high resolution and reproducibility afforded by a commercial high-resolution piezo actuator, the capacitive system has asserted itself against the resistive strain gauges because strain gauges always exhibit hysteresis, creep and $^{1}/_{f}$ – noise.

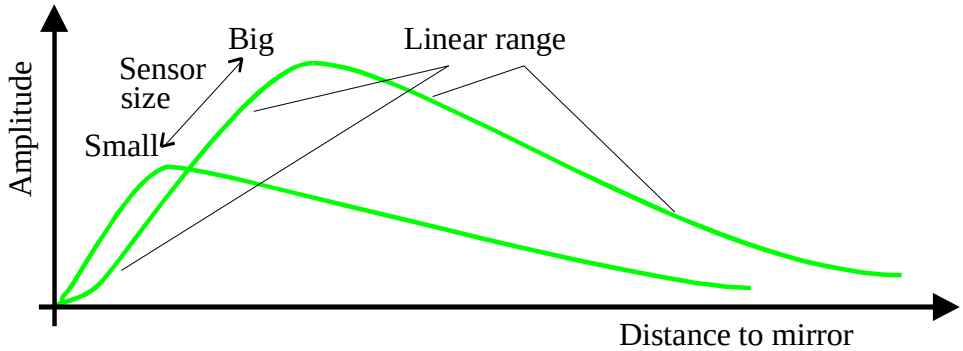

Fig. 6-8 Principal characteristic of the fibre sensor and its dependence on the fibre size

However, an adequate linearization of the capacitive system requires extensive effort. A further disadvantage of the capacitive system is that the second electrode, inclusive the coaxial or triaxial cable, has to be moved by the piezo actuator. This can reduce the dynamics if the mass of the electrodes is high. In an optical system, only a small mirror must be moved in the simplest case. Ground loop problems or electrical cross-talk is non-existent and there is negligible movement of the mass.

With glass fibre bundles, light can be brought to the reflector surface and the reflected light intensity can be detected. A spatial separation between the sensor location in a controlled system and the evaluation electronics is possible by the use of this arrangement. A concentric arrangement of the illumination and detection fibres produces two ranges where almost linear behaviour in the intensity versus distance curve is observed (see Fig. 6-8).

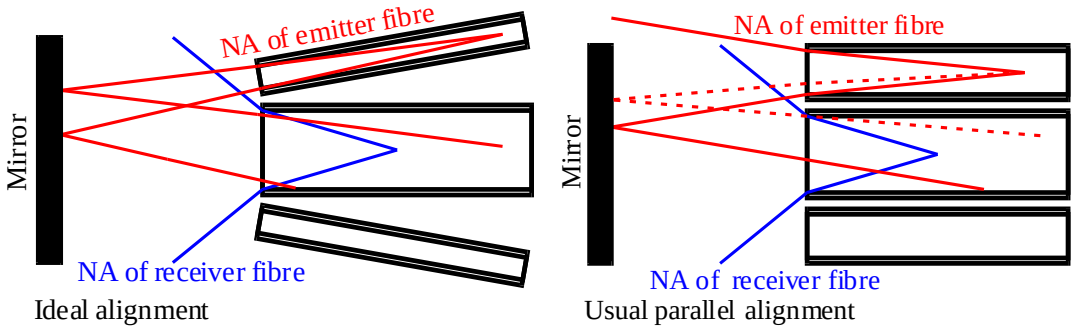

Fig. 6-9 Alignment for an ideal fibre sensor (left) and the conventionally used fibre sensor (right)

The light intensity increases dramatically with a small distance from the reflector surface, resulting in a high upward gradient and a correspondingly high sensitivity. If the distance increases, a maximum in the light intensity is achieved, beyond which the signal decreases and a second linear range with a smaller, downward gradient is observed. Using smaller sensor geometries, the upward gradient increases. These sensors are particularly suitable for measuring short distances. However, the sensor characteristic also depends on the numerical aperture of the fibres and consequently, the emission angles of the fibres. A high emission angle results in a lower gradient so that the sensor can measure longer distances. The highest sensitivity is related to the rate of the detected light. Fig. 6-9 (left) shows an ideal fibre sensor where 100% of the emitted light from the illumination fibre is reflected to the detection fibre. In practice, an easily produced fibre bundle is used (see the right side of Fig. 6-9), where only approximately 20% of the illumination light is collected.
A lens can be used to extend the working distance of the fibre sensors, which is not required for a short-stroke piezo actuator. Only a portion of the total range can be used for the linearization capability and an offset zoom principle must be used to achieve a reasonable signal level from ±10 V.

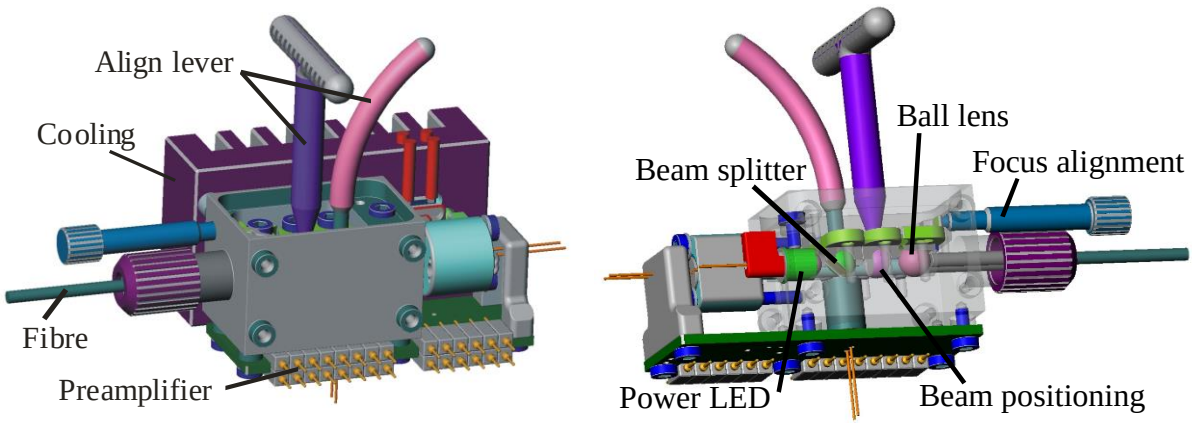

Fig. 6-10 First prototype of the fibre sensor arrangement[21]

A low gain of the electric amplifier is needed for a low-noise fibre system because the noise increases with amplification due to the noise of the feedback resistor and the bandwidth decreases with increasing resistance. For an optimal use of the operation amplifier (OP), the offset current must be subtracted before the gain amplification of the OP. This is the same procedure

as for the detection of the laser beam with the 4-quadrant photodiode of the beam deflection system in chapter 5.5. Thus, the amount of incident light is also maximised here. However, a noise and drift-depleted light source is needed in addition to the maximised light power. Fig. 6-10 shows the arrangement for the novel SFM system. The chosen beam splitter cuts off 10% of the Power-LED light. A feedback loop with a noise and drift-depleted photodiode (S2386-18 Hamamatsu) is used for the electric power control.

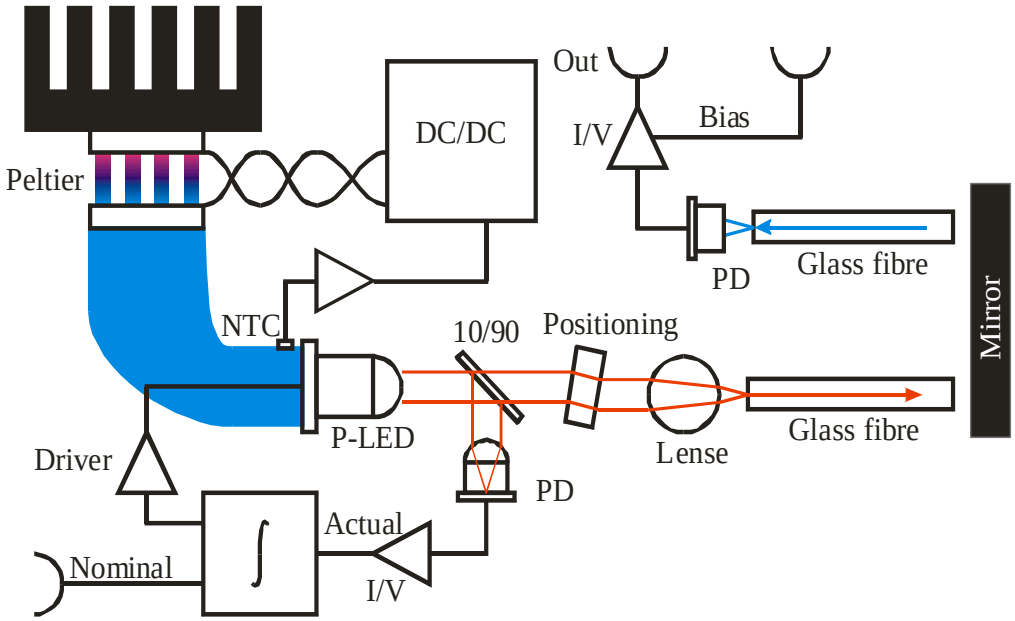

Fig. 6-11 Schematic diagram of the fibre sensor system setup[21]

The beam splitter is adjusted over a ball joint mounting such that the photodiode maintains a maximum light power. The rest of the primary light can be adjusted by tilting a parallel disc onto a sphere lens so that the maximum intensity is coupled into the glass fibre (the fibre bundle). The focus of the spherical lens can be adjusted to also optimise the intensity of the light that is guided into the glass fibre. The reflected light of the reference mirror is coupled into the detection glass fibre to a further photodiode, where it is transformed using an electric current-to-potential converter into a voltage that correlates with the fibre-mirror distance. A schematic of this modification is shown in Fig. 6-11.
After mechanical positioning to one of the inflection points where the highest linearity is located, the output voltage can then be adjusted to the centre position (at 0 V) by the bias current at the receiving photodiode amplifier. The light performance increases with the amplification until the maximum movement is equivalent to a voltage signal of ±10 V. Further linearization is possible, depending upon the position of the characteristic curve, by adding a quadratic or cubic term to the output.

$$U = U + a \cdot U^2 + b \cdot U^3 \qquad \text{Eq. 6-1}$$

The factors *a* and *b* include the algebraic sign required to minimise the error. The static value was already eliminated by the adjustment with the bias current.
An AD633 (Analog Device) is used for analogue multiplication. The required error corrections are in the range of a few per cent; thus, the noise and drifting of the device can be neglected, as these failures can be reduced by a voltage divider.
After the linearization adjustment, the total range of the ±10 V signal can be adjusted again by the offset-value and the amplification. This procedure must be repeated several times to obtain

a good adjustment. With the help of this linearized distance measurement unit, a closed loop piezo or hydraulic positioning system can then be set up.

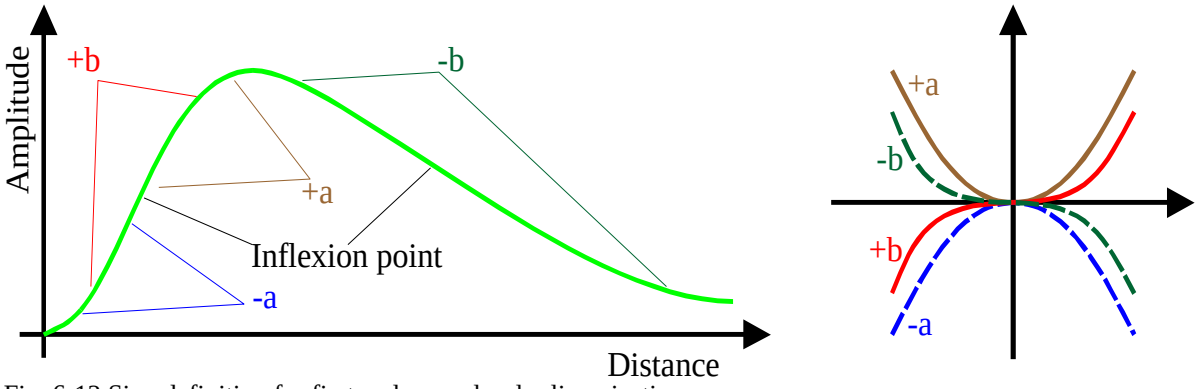

Fig. 6-12 Sign definition for first and second order linearization

A differential fibre arrangement is needed for a high resolution positioning measurement with long scan-range to lower the drift and the noise of the light source. The light of one high power LED is thus linked to two fibre sensors. Light fluctuations in both signals are removed by the subtraction of the signals if the light is controlled by a constant sum signal. The noise of the preamplifier, which is dominated by the feedback resistor of the current/voltage converter (see chapter 5.5), can also be lowered.
For a high-resolution SFM system, a hardware linearization for all three axes is obviously needed. Capacitive sensors are used for this purpose in most commercial systems. This system uses optical sensors. The clear advantage of the optical fibre, unlike a capacitor with extensive and complex guarded electrodes, is that only a light source is needed and a small mirror is used as a moving part.

6.4 Complete setup of the sample moving stage

The elements described above form the main mechanical section of the sample moving stage and the linearization capability. As shown in Fig. 6-14, the main body is comprised of four pressure cells for the low frequency Z-drive and the lateral hydraulic XY-drive.

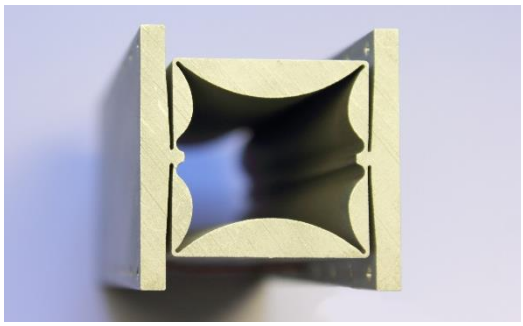

Fig. 6-13 Flexure hinge of the lateral XY-drive

The XY-drive consists of a moving block in the centre with four pressure cells connected to the outer main block via eight flexure hinges. The flexure hinges are constructed such that the degrees of freedom are in X- and Y-directions and the hinges are stiff in the Z-direction (see Fig. 6-13). The material thickness at the edges of the square is approximately 300 µm.

A cover plate connects the pressure cells together where the coarse XY-positioning unit is located on top of the plate. The coarse positioning unit holds the mid-range frequency Z-drive (all the water-cooling units have been removed for clarity).

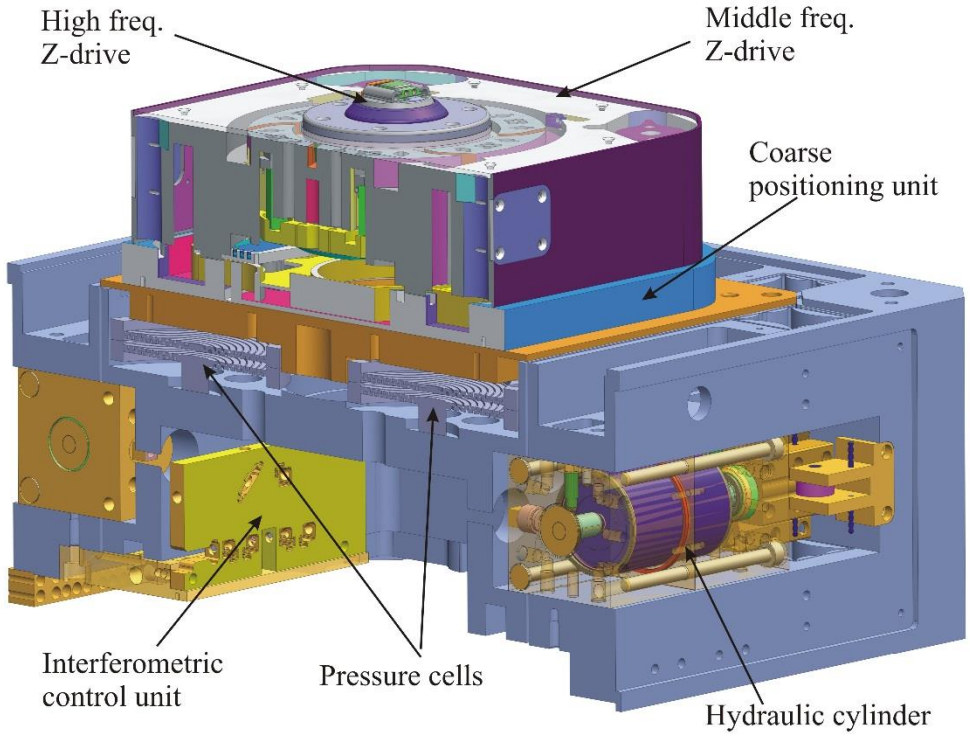

Fig. 6-14 Mechanical setup of the sample moving stage (with the additional interferometric linearization unit for calibrating the standard linearization of the XY unit)

The high frequency Z-drive is mounted with the sample holder on top of the mid-range frequency Z-drive. The XYZ-drive couples high frequency motion, by connecting the hydraulic drive and piezo drive, with highly precise positioning due to the linearization of the XY-drive and all three Z-drives, along with a multi-level cooling system.

7 Electronic control unit, and control, communication and visualization software

The novel SFM with its extended scan width, additional environmental controls and fast and high resolution data acquisition requires completely new techniques for data acquisition and processing, data transfer from the electronic control unit (ECU) to the personal computer (PC) and last, but not least, data storage and visualisation on the monitor. The following sections describe the new techniques developed for the SFM system.

7.1 DSP-control of the electronic control unit

A digital signal processor (DSP), specifically a Texas Instruments 6711 floating-point processor with a100 MHz clock rate, is used for triggering each write and read cycle and the separation of data streams, as well as an initial data reduction.

	r/w	Name
1	r	ADC 1+2 Topography changes from last to actual sample (ADC1=high z-piezo, ADC2= mid z-piezo)
2	w	DAC 1 last high z-piezo sample
3	w	DAC 2 last mid z-piezo sample
4	w	DAC 3 & 4 X & Y scan
5	w	DAC 5-10 Walker
6	r	ADC 3+4 (two 16bit input channels, each ADC/channel 1 MSPS)
7	r	ADC 5+6 (two 16bit input channels, each ADC/channel 1 MSPS)
8	r	ADC 7+8 & 9+10 (two times two 16bit input channels, each channel 500 kSPS)
9	w	ADC 11+12 & 13+14 & 15+16 & 17+18 (four times two 16bit input channels, each channel 250 kSPS)
11	w	ADC 7+8 & 9+10 channel multiplexing
11	w	ADC 9+10 & 11+12 & 13+14 & 15+16 channel multiplexing
12	r/w	128er splitting of slower read and write channels

Fig. 7-1 Time-slices of the DSP data acquisition

The first four time-slices are important for the basic functions of the scanning force microscope. As described in the earlier chapters, the z-scanner is separated into three units. The low frequency Z-scanner for the static plane subtraction, the mid-range frequency scanner and the high frequency scanner are all feedback-controlled and read out in time-slice 1. These signals are modified by the offset and zoom principle, so that the analogue-to-digital converters (ADCs) deliver the difference between the previous and present points of measurement.

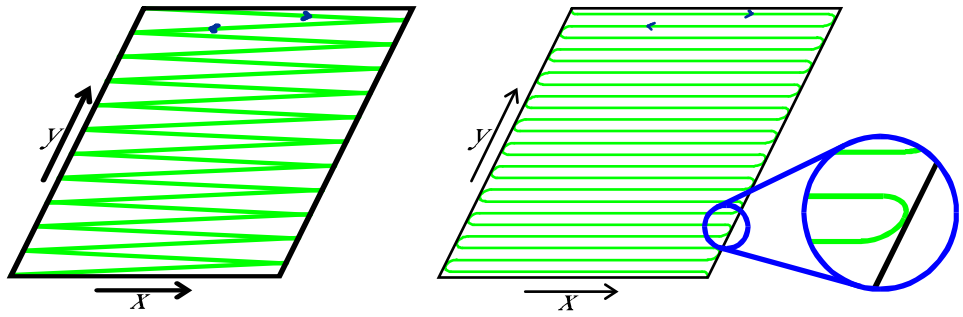

Fig. 7-2 Different ways scanning a probe surface

The DSP adds these values to the most recently stored position values of the high and mid-range frequency piezos. These values are stored in the DSP and sent via the digital to analogue

converter (DAC) with 24-bit resolution to the high frequency z-piezo in time-slice 2 and to the mid-range frequency z-piezo in time-slice 3.
Time-slice 4 sets the new values for the lateral motion in x- and y-directions. DAC 3&4 both use 24-bit resolution. With a bus width of 32 data bits, the two values have to be set separately. The scan system does not perform the triangular sweep shown in Fig. 7-2 (left) because this behaviour requires continuous updating of x- and y-values and the data rows are only virtually parallel.

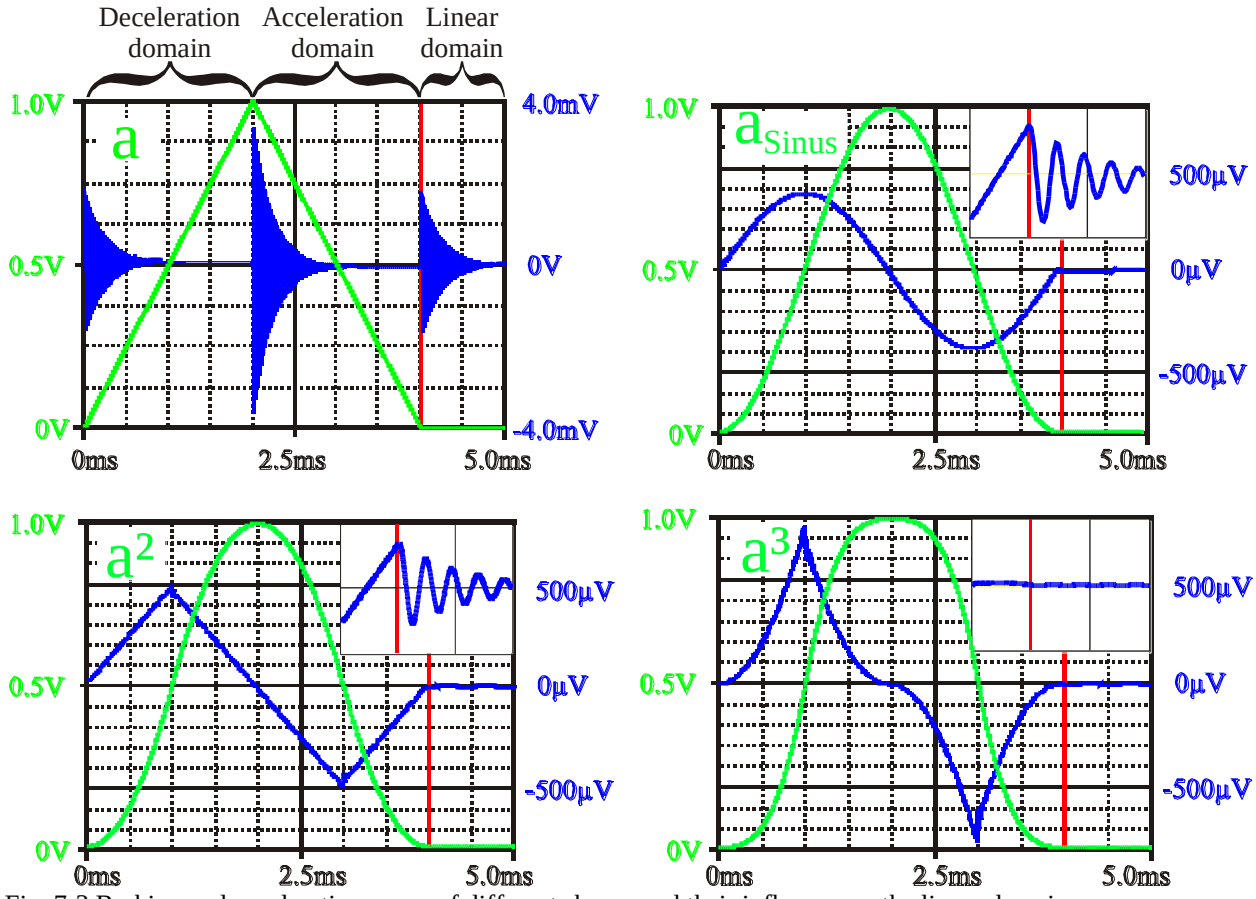

Fig. 7-3 Braking and acceleration zones of different shapes and their influence on the linear domain

The novel scan system uses a scan row that is completely free of y-motion. In the deceleration zone, for a decreasing the x-velocity, the spatial y-offset is successively added to the next row, with increasing values until the x- inflection point is reached. After this point, the process works in the opposite direction, with the acceleration in x-direction during the y-step value decreasing to zero, after which the linear motion starts again (Fig. 7-2, right side). The y-free motion guarantees a maximum uniform velocity in the x-direction, which is necessary for experiments measuring friction and for certain other scan modes. The domain width in which the deceleration and acceleration take place depends only on the velocity of the linear scan domain. Therefore, every change of the scan velocity increases or decreases the maximum linear scan width. However, analysing how the acceleration decreases or increases the velocity reveals a second way of optimising the linear scan range. The set of curves in the upper left of Fig. 7-3 shows a linear increase and decrease of the acceleration that describes the constant velocity behaviour during the linear x-motion (green curve). The blue curve shows aberrations in the simulated piezo position, which are high at the points of discontinuity. A resonance of the piezo is stimulated at these points. Changing the acceleration curve to a sinusoidal shape (upper right, Fig. 7-3) reduces the visible distortions, especially at the transition to the linear domain (inset in the upper right corner). The calculation of a sine value is time-intensive for a processor, even a

DSP. The DSP takes approximately 27 clock cycles to calculate a sine value. The diagram on the lower left of Fig. 7-3 shows the aberration with quadratically shaped acceleration behaviour. There is no observable difference between the aberration of the sine and the quadratically shaped acceleration, but the DSP needs only up to 3 clock cycles to calculate a squared number. However, the last diagram on the lower right side shows the aberration with a cubically shaped acceleration. The aberration within the deceleration and acceleration zone increases, but this is not interesting for the linear behaviour and the measurement itself. The most important observation is that the error after the transition to the linear zone is several times smaller than before. Based on this behaviour, the size of the reversal zone can also be reduced to increase the size of the linear zone.
As a result, only one time-slice is necessary for x- and y-motion even if a rotation angle is added to the scan area. The zoom function used is shown in the figure below.

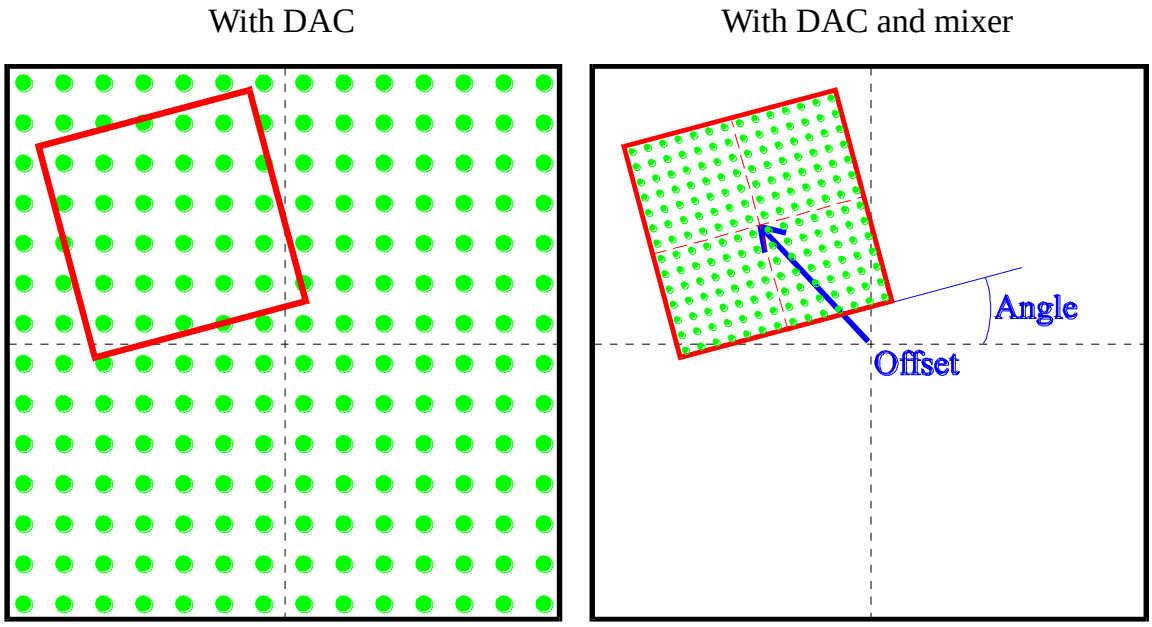

Fig. 7-4 Data logging using a digital-to-analogue converter (DAC), without and with the mixer circuit board

An analogue mixer circuit can achieve this behaviour. This circuit is shown in Appendix A - 3. The x- and y-signals are multiplied by a factor between –1 and +1 to zoom in and out. If the x- and y-signals are not equal, a non-quadratic scan can be performed. Both signals are added with an additional offset and an additional signal called the z- or temperature input. The offset is used for a non-centric scan. The temperature input can be used to eliminate a first-order temperature drift of the system with a fixed value or by installing active drift compensation if the system has an active temperature control.
With two mixers (Appendix A - 4, page 85), a rotation of the scan orientation is possible using the following co-ordinate transformation:

$$\begin{pmatrix} X' \\ Y' \end{pmatrix} = \begin{bmatrix} \cos\alpha & \sin\alpha \\ -\sin\alpha & \cos\alpha \end{bmatrix} \begin{pmatrix} X \\ Y \end{pmatrix} \qquad \text{Eq. 7-1}$$

The offset, zoom, scan area shape and angle are only static values within the mixers. They are calculated once before the scan is started, and they do not influence the DSP generated x- and y-values. Thus, the resolutions for the DACs for x- and y-positioning are also not reduced during a zoomed scan (see Fig. 7-4, right).

Time-slice 5 is only used if no scan is in progress. The different walker motors of the system are connected via electronic switches, to the:

- ‘coarse’ sample adjustment,
- beam deflection laser x-, y- adjustment
- 4Q-PD x-, y-, z- and δ-adjustment
- Z-camera adjustment in the x-, y- and z-directions
- Z-slide for the combined motion of the Z-camera and the cantilever approach

The values in this time-slice generate up to six voltage ramps to move the walker piezos as demonstrated below.
During the step phase, each piezo (one after another) slips a few 100 nm and sticks at a certain position. After every piezo of the walker motor has performed this step, all of the piezos move back simultaneously with a slower velocity and take the slider with them. This movement can occur in one time-slice because the DAC addressing can call one defined output for one piezo (slipping-phase), or can address and update all outputs at the same time (walk phase).

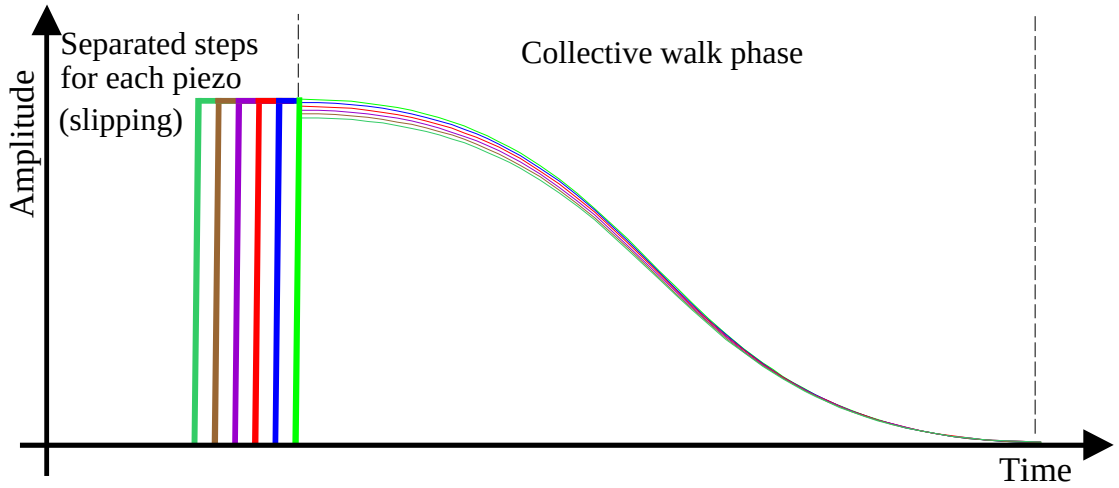

Fig. 7-5 Piezo walker ramps

The time-slices 6 to 9 are channels for reading different boards. For example, as shown in the list above, there are two fast cards with two 16-bit 1 MSPS data rates, one card with two- times-two multiplexed channels with 16-bit and 500 kSPS data rates each and last, but not least, 4 times-two channel inputs with 16-bit 250 kSPS data rates. These channels can be used for different additional signals with high or semi-high performance. Time-slices 10 and 11 are used to switch the channels from the ADC cards of time-slices 8 and 9. It is important to switch this multiplexer as fast as possible after the readout of the ADCs because the electronics need time to measure the next values. The cards have their own filter for each input so that the switches are between the filters and ADCs and the filters do not need any time to settle down to a new input value. Only the ADCs need time to sample the next ‘true’ value. The twelfth slice is a special as it measures up to 128 different signals. Here, each cycle of the time-slice table changes to a different signal input. Every time-slice is used one million times a second and 128 different signals are read or set with a frequency of approximately 7.8 kHz (which is equivalent to 7.8 kSPS). If necessary, one signal can be set or read two times or to another power of two, while low frequency signals can be read or set only once per 128 cycles. These channels are used for temperature, humidity, air pressure and so on.

The DSP separates the incoming values and rearranges them into data chains. The data of the fast channels can also be reduced with a finite-impulse-response filter (FIR filter) because the number of saved data points in x- and y-directions is only limited by the sample rate of the ADCs. Thus, if a user sets the scan area to one by one millimetre and the time per line to 10 seconds, the following data rate will be transferred and stored on the PC via the fast channel:

$$filesize = resolution_{data} \cdot linetime \cdot samplerate_{ADC} \cdot datalines_{y-direction} \quad \text{Eq. 7-2}$$

Using a resolution of 16 bits, a scan time of 10 s per line, an ADC sample frequency of 1 MSPS and a quadratic scan, $datalines_{\text{y-direction}}$ equals *linetime* multiplied by $sample\text{-}rate_{ADC}$ so that the equation above gives the following result:

$$filesize = 16bit \cdot 10s \cdot 1 \cdot 10^6 s^{-1} \cdot (10s \cdot 1 \cdot 10^6 s^{-1}) = 1.6 \cdot 10^{15} bit \quad \text{Eq. 7-3}$$

This results in a $1.86*10^5$ Gbyte or 182 Tbyte file size. Obviously, this is a difficult volume of data for one channel to transfer to or store on the PC (an image of this size would take approximately 116 days to be generated). While the software places no limit on the number of data points and data lines, a current state-of-the-art personal computer has a rational limit for an image of 100.000 points by 100.000 lines, which results in an 18.6 GB file per channel even this image would take over one day with one second per scan line to complete.
The DSP also has 64 MB of external RAM. Using the re-trace mode to collect additional data during the backward scan at the same line, the spatial information from the forward scan must be stored and re-loaded within the electronic control unit (ECU) to avoid data collisions on the serial bus due to heavy data loads. Data can be stored at a maximum of 33 seconds with a full 16-bit 1 MSPS data rate. The data that is stored within the ECU is raw data that has not been filtered; thus, the back scan is as exact as possible.
The collected and sorted data stream of each channel must now be transferred to the personal computer. This action is performed by a serial communication called FireWire®.

7.2 Communication between the electronic control unit und the personal computer

The serial communication is an IEEE 1394a (iLink®, FireWire®) bus interface that can accommodate up to 63 devices.
As this serial communication uses an 8B10B code (8 bit to 10 bit code), the connection between the ECU and the PC is electrically isolated (no ground loop). The data rate for the 1394a interface can go up to 400 $^{\text{Mbits}}/_{\text{s}}$, theoretically. This serial connection can transfer high data rates from the ECU to the PC and can be updated to the next IEEE 1394b standard with up to 800 or 1600 $^{\text{Mbits}}/_{\text{s}}$ with minimal hardware and software changes. Since October 2008, an advance 1394b standard offers 3200 $^{\text{Mbits}}/_{\text{s}}$. The transfer via this bus is separated into an asynchronous and an isochronous transfer. The asynchronous transfer can be used for small amounts of data down to a single bit transfer. This type of transfer is mostly used from the PC to the ECU because the settings of the gain levels, filter levels, offset values, address presets and so on are normally only a few bytes long. The asynchronous transfer has the disadvantage of being able to be performed, if allowed, by the isochronous time slot control of the serial communication between the isochronous data transfer slots. The isochronous transfer is for streaming data, which is performed each 125 µs and can carry 4 Kbyte data load per package. A total of 32 $^{\text{MB}}/_{\text{s}}$ isochronous data transfer is possible; therefore, a theoretical maximum of 16 fast channels with 1 MSPS and 16-bit data, or a division of more, but slower, channels can be transferred.

One of the main advantages of FireWire is its peer-to-peer and autonomous structure. The bus resets itself every time the bus changes or a device is either added or removed. During the reset, each node is assigned to a device number and a root node (normally the fastest node) is chosen to coordinate all the activities on the bus. The bus reset occurs within 300 µs after a change. The ability of the bus to dynamically reconfigure itself is one of the great advantages of FireWire in opposite to USB. USB requires a central controller/host computer, whereas FireWire requires that each device, if chosen, is able to run the bus. Furthermore, this self-control of the bus nodes releases the processors of the PC and the ECU. With adequate software on the PC and the ECU, even a break in communication can be intercepted and the ECU can stop the actual scan and re-start from the last position. This causes some disturbances within the scan line, but for an image, which can take hours or even a day to scan, one line, is an acceptable loss.
This security issue is connected to that of the PC, which is discussed below.

7.3 PC control and visualisation software

The PC software is a multi-threaded working and user interface environment. It starts with a call to the user to select a personal experiment profile. Within the PC, all user setups are automatically stored under a user-defined name for further use. The profiles not only store the names of data channels but also store the last scan position, size, velocity, cantilever set point, feedback parameters and so on. A certain name and unit can be given to all the ADC channels that are used in the entire user interface. A zero-adjust and a gain-adjust are accessible to calibrate each channel. Additionally, a gain (1-16) and a filter (mute, 10 kHz, 20 kHz… 150 kHz) can be set for some ADC cards.
The received data must be specially handled to address the large amount of incoming data for each channel and the large number of channels. The data stream of each channel is re-filtered down to the user-defined scan resolution, if necessary. The data are then transferred and stored on the hard disc. After the user hits the start button and before the scan takes place, the complete file is generated on the hard disc. The complete file is filled with mid-range values. For the large amount of data calculated with Eq. 7-3 in chapter 7.1, it is not possible to store all the data in the PC memory. Neither is it useful to try to visualise a 100,000 by 100,000 point image on a monitor, even one with high resolution. The visualisation of the data is either a reduced image of all the data of each channel or a zoom of the data. This type of image pixel reduction is well-known from Google Earth®, for example, and is called “mipmap” and “clipmap”[39]. The maximum resolution is calculated from the user-defined size of the visualisation window of a channel and the image is recalled from the hard disc. The “mipmap” is a stack of images on the hard drive with an inverted pyramid resolution, where each level has twice the resolution of the one under it. The “clipmap” is a tiling technique, where during a zoom only a small portion of the entire image is visualised for the user and only this portion of the image is loaded so that storage in the PC RAM is possible, even with all the other possibly open channels. The recall of the data that takes place during the scan involves two data streams per channel: the incoming stream that has to be written and the visualisation stream that must be read from the hard disc.
All the user-defined changes that affect the ECU are stored on the PC in the user profile and are transferred to the DSP internal RAM in the ECU. This is the next security feature of this software. After an electrical breakdown of the PC and/or the ECU, the disrupted scan can be continued from the last scanned position so that a time-intensive scan can be completed.
The user only needs to start a new scan with a new sample, without completing the old image, if the sample is dynamically changed by temperature, electric fields, chemical influences or if the time between the breakdown and re-start is excessive. Nevertheless, even the unfinished

image can be visualised because the data are stored continuously on the hard disc and the remainder of the image has been filled with constant mid-range values, as mentioned above.
The software presented here for the new scanning force microscope demonstrates the need of completely new techniques for the acquisition of the basic and advanced data channels, the preprocessing of data.
The storage and recall of data within the electronic control unit, the transfer of date from the electronic control unit to the personal computer, and finally yet importantly, the handling of the data to visualise the different channels in a user-defined manner needs new techniques as well.

8 Conclusion and perspectives

In this thesis, a novel scanning force microscope was presented for temperature-controlled static and dynamic friction measurements, using an extended normal and lateral working range with high spatial resolution. Other than the large scan range of approximately 1000 µm by 1000 µm, the thermal guidance of the cantilever and sample is the most labour-intensive component of the microscope. Detailed construction of the cantilever holder and sample holder, light beam guidance for the normal and lateral forces, the positioning and scan unit, and ECU, control software and communication software have been discussed.

The entire microscope was constructed as symmetrically as possible using mechanical construction to avoid thermal drift. For thermal measurements and thermally assisted friction measurements, a concept for separately heating the cantilever holder and the sample holder was discussed. A simulation on the cantilever holder showed that a temperature difference of 150°K could be reached after 40 s and that the cool down cycle took only 38 s. During the heating and cooling cycle, the temperature was held for 60 s and the temperature rose by only 62 K at the nearest piezo. The same analysis was performed for the sample holder. Only the junction temperature for unknown samples and the temperature behaviour of these samples was calculated. After 15 s of heating, the junction reached 150 °K above the ambient temperature; a hold time of approximately 85 s demonstrated the temperature stability of the sample heating, and the cool-down cycle took less than 40 s. The thermal path to the next piezo element is more critical than the one for the cantilever holder setup, especially because the Curie temperature of this piezo element is lower than the piezo at the cantilever. Therefore, the thermal management is more complex. However, the analysis has shown a maximum rise of 32 K above the ambient temperature at the piezo element for the heating and cooling scenario described above.

For the beam deflection setup, a single-mode glass fibre supply of the laser light beam was used. A special grinding technique was used to form fibre tips, which can be short-duration fused to form a small lens for pre-focusing the light beam (two patents have been submitted). The focused beam is sent through a specially manufactured prism. The prism is used for the incoming and cantilever-reflected laser beam, masking all light that is not from the cantilever, and allows a perpendicular observation of the cantilever and sample surface via a camera system. The adjustment of the laser beam to the cantilever and on the 4Q-PD is achieved completely via software-controlled piezo drives. A sample setup showed that the self-assembled laser beam has a diameter of approximately 60 µm. With 10 µW of light on the 4Q-PD using a standard cantilever, the electronics produced a displacement equivalent to the noise of approximately 0.1 nm with a 10 kHz low-pass filter. With a good SFM, the thermal noise of the cantilever can be detected by the SFM electronics. With the beam deflection system introduced here, even the first and second resonances, in addition to the basic one, were observable with the spectrum analyser. The torsional basic mode and its first harmonic were also observed.

The Z-drive was separated into low, mid-range and high-frequency components. This separation aids with the thermal management of the microscope to avoid and/or remove unwanted thermal heating in areas of the system where mechanical drift disturbs the scanning force measurements. Active cooling with Peltier elements and water-cooling at certain positions facilitate thermal management. However, this was not the only motivation for designing the Z-drive as described. The considerable enlargement of the lateral scan size leads to much the same enlargement of the Z-scan size as afforded by the tilt compensation capability. The hydraulically driven low frequency Z-component fulfils this requirement. A European patent has been granted for the hydraulic cylinder design.

While linearization in x-, y-, and z-direction is always desirable, it is a necessity for the scan range of the microscope introduced here. In terms of weight reduction, linearity and handling, an optical solution was designed for the microscope. Each scan range could be assembled with a specially adapted linearization unit (fibre bundle and mirror) as the linear behaviour of each

linearization unit is proportional to the numerical aperture of the guiding fibres. Therefore, the scan unit was equipped with four 1000-µm linearization units for the XY lateral scan stage, four 300-µm units for the low frequency Z-drive, three units with 12-µm linearization capability for the mid-range frequency Z-drive, and three units for the 2-µm Z-drive.
Finally, the ECU and the control, communication and visualisation software were presented. The centrepiece of the ECU is a Texas Instruments 6711 floating point DSP. This unit features the real-time capability that is necessary to drive such a microscope. The DSP communicates via a serial, insulated interface (FireWire®) with the PC in burst mode, while collecting data from the sensor channels in strict, fixed time-slices. Again, the data channels have to be precise and very fast due to the large scan range, to keep the scan times in a manageable regime. Six channels have 16 bit resolution at 1 MSPS, four channels have 16 bit resolution at 500 kSPS, and eight channels have 16 bit resolution at 250 kSPS. One time-slice was also used up to 128 times for multiplexing pre-selection for one arbitrary channel, which can be used to detect slowly changing signals. At this sample rate, a meander-shaped scan line could be achieved. Different types of deceleration and acceleration behaviour were calculated to obtain the largest possible linear scan range, resulting in cubical behaviour during deceleration and acceleration for even the smallest disturbance in the linear scan regime. The mixer electronics were designed with offset and zoom capabilities. This results in linear DAC sample steps within the chosen region, independent of the user-chosen region of interest (angle and size).
Data are transferred in burst mode to the PC while one line is being scanned and can be held in the DSP external RAM for Lift-Off back-scanning capability. The datasets are separated in each channel within the PC. No limit on the digital resolution was deliberately set. The user can define reasonable values with the PC being the limiting element. The outcome is a new visualisation technique for such microscope systems. The data are first saved to a hard disk and structured in such a way that the user can define whether a "low resolution" overview screen or a "high resolution" zoom of a portion of the entire scan will be observed.

Many ideas could not be implemented during this thesis, which will be briefly described as possible future extensions of the system presented here.

Controlling the local atmosphere within the sample covering glass tube
Isolating the sample in a glass tube allows variation in and dynamic control of the pressure, the gas mixture and the humidity within the tube. The multiplexed data channel could be used to measure and control these values.

Lithography:
A lithography system can be implemented using the open electronics and software. Given that the system has for all three dimension a closed –loop control, the implementation of lithography system is predominantly a software work. In addition to controlling the atmosphere as mentioned above, different gas mixtures, gas temperatures and pressures could be used.

Fluid cell:
A fluid cell could be built within the gas tube so that fluids could be interchanged and exchanged during measurement. The interaction of the fluid cell and the gas tube can extend the use of the fluid cell, for example, if volatile fluids are used or harmful gases have to be removed.

Heating the sample and cantilever with different temperatures:
As in the "nose project"[40], the separately temperature-controlled sample and cantilever could be used to conduct temperature-resolved mass measurements of volatile sample components.

Cantilever with a sphere instead of a tip:

A cantilever with a sphere up to 100 µm diameter, for example, could be used with the 1-mm scan range. This size range closes the gap between the tip radius of a tribometer and the tip radius of an SFM cantilever.

Triboelectric effect and triboluminescence:
Measuring the tribolectric effect during friction experiments could provide additional information about material composites. Similar information could be obtained if a photosensitive detector collects the triboluminescence. It is conceivable that data could be stored on a sample by storing charges in the sample if triboelectricity and triboluminescence could be observed. This effect could be switched on and off by switching the dither piezo on and off, for example.

Active bypass for the hydraulic cylinder:
An active bypass can enhance the discussed advantages of the hydraulic cylinder in terms of both the high dynamic and the precise and low-noise characteristics.

The analysis for the novel scanning force microscope presented here shows the feasibility of this system. The enhancement of the scan range and the use of temperature guidance lead to a major re-design of most of the hardware and software components of such a microscope. The analysis of the response to temperature variations was also helpful in designing the XYZ-drive as presented in this work.

A Appendix

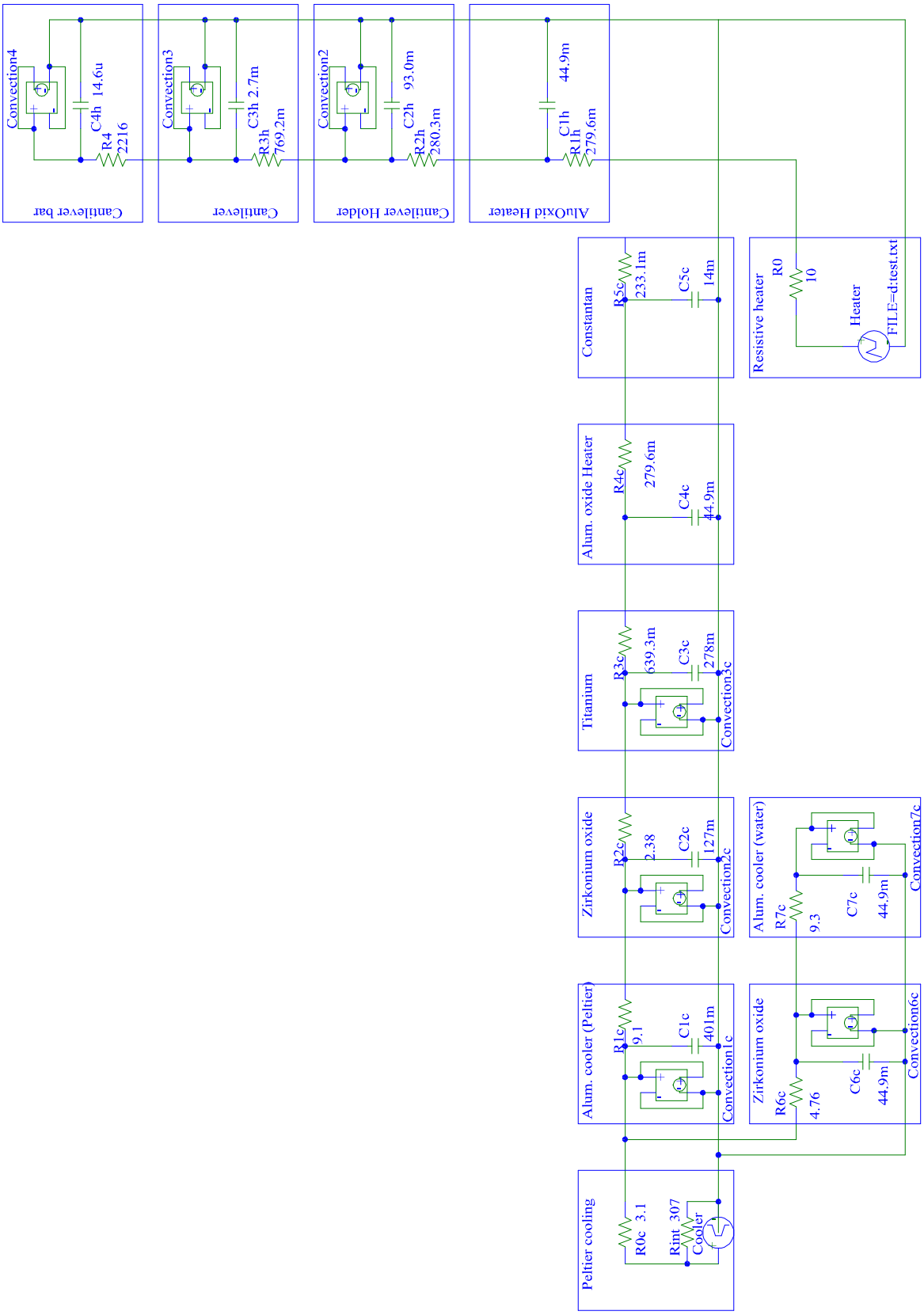

Appendix A - 1 Schematic of the cantilever heater and cooler setup

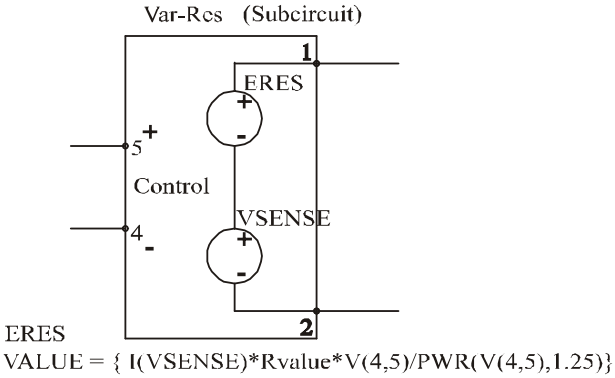

Appendix A - 2 PSpice simulation model for a variable and non-linear resistor

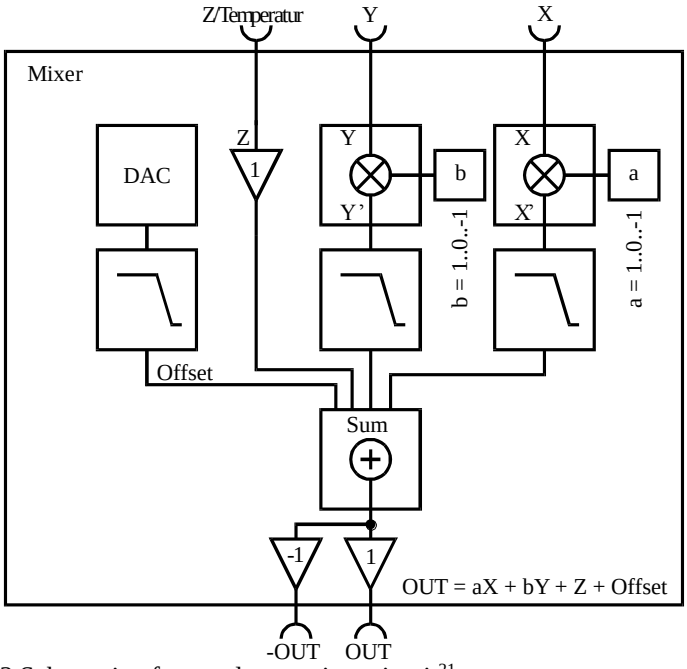

Appendix A - 3 Schematic of an analogue mixer circuit[21]

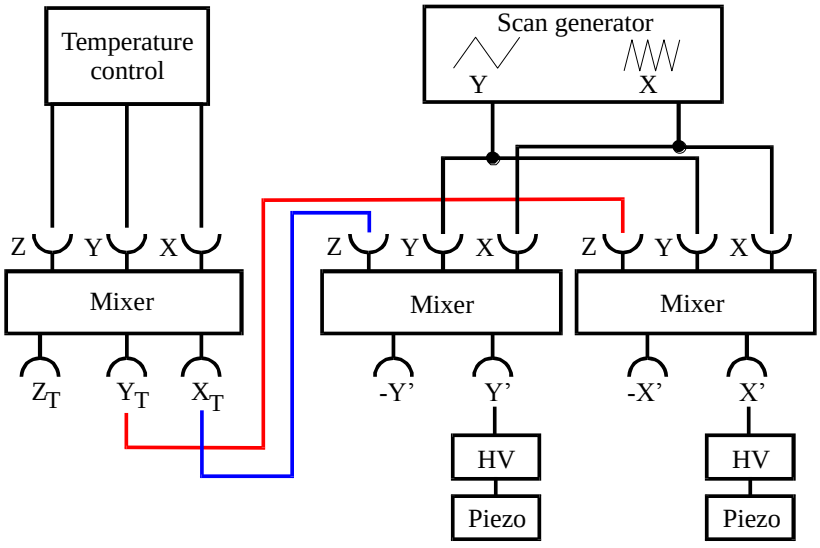

Appendix A - 4 Schematic of a temperature-compensated mixer setup

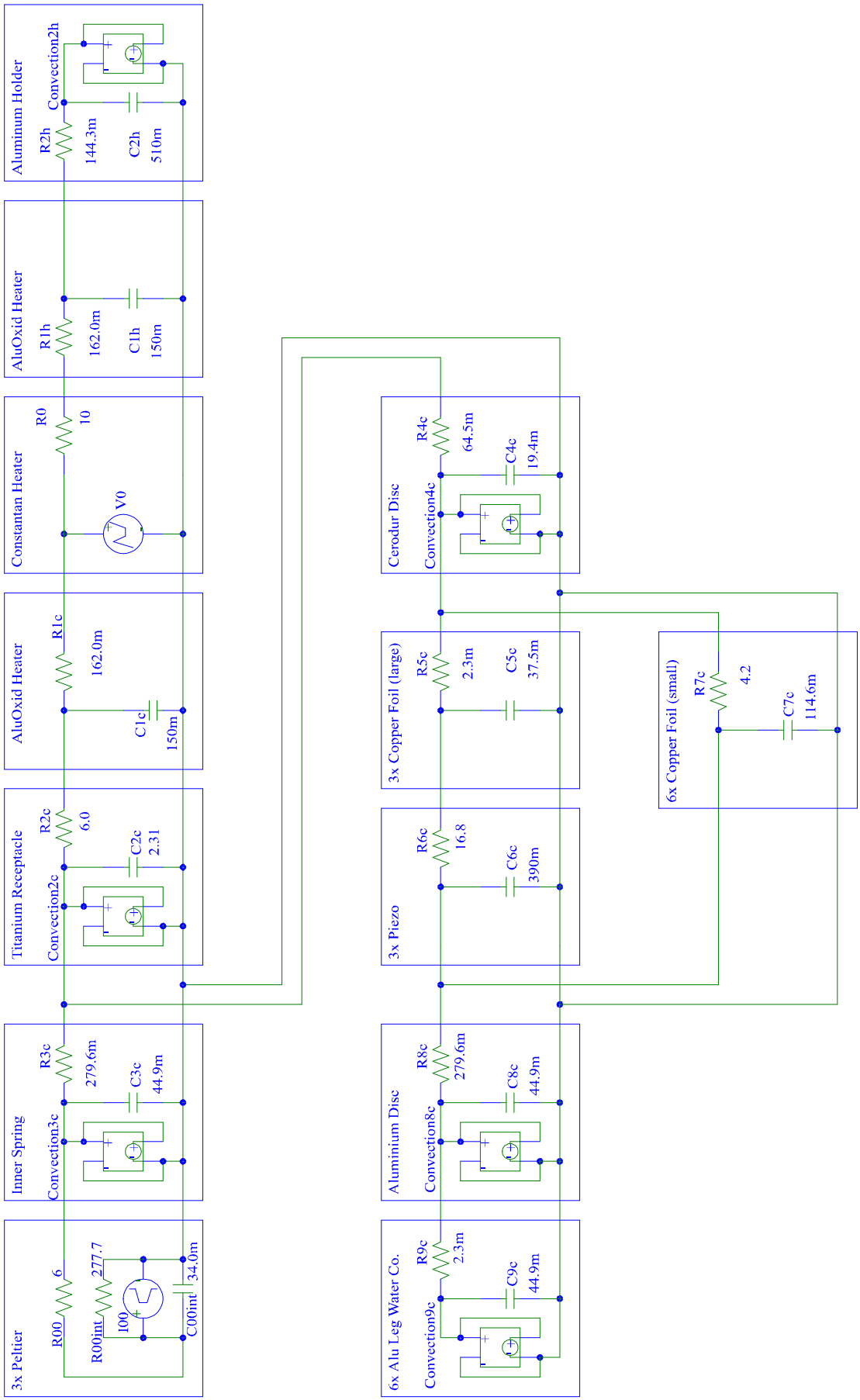

Appendix A - 5 Schematic of the sample heater and cooler setup

References

[1] G. Binnig, H. Rohrer, Ch. Geber, and E. Weibel, *Surface Studies by Scanning Tunneling Microscopy,* Physical Review Letters, **49**, 57 (1982)

[2] G. Binnig, C.F. Quate, Ch. Gerber, *Atomic Force Microscope,* Phys. Rev. Letters, Vol. 56, No 9, 1986, p 930

[3] R. Young, J. Ward, F. Scire, *The Topografiner: An Instrument for Measuring Surface Microtopography,* Rev. Sci. Inst., Vol 43, No 7, p 999

[4] R. Daniels, S.N. Magonov, *Method and system for increasing the accuracy of a probe-based instrument measuring a heated sample,* US Patent Application No 09/354,448, 15.7. 1999.

[5] D.A. Ivanov, R. Daniels, S.N. Magonov, *Exploring the High Temperature AFM and Its Use for Studies of Polymers,* Application Note 45, Veeco Instruments Inc.

[6] Nose Project (here adapted for temperature disperse condensation measurements)

[7] A. Knoll, P. Bächtold, J. Bonan, G. Cherubini, M. Despont, U. Drechsler, U. Dürig, B. Gotsmann, W. Häberle, C. Hagleitner, D. Jubin, M.A. Lantz, A. Pantazi, H. Pozidis, H. Rothuizen, A. Sebastian, R. Stutz, P. Vettiger, D. Wiesmann and E.S. Eleftheriou, *Integrating nanotechnology into a working storage device,* Mic. Eng., Vol 83, Issue 4-9, 1692-1697 (2006)

[8] Yueming Hua, Shubham Saxena, Clifford L. Henderson, William P. King, *Nanoscale thermal lithography by local polymer decomposition using a heated atomic force microscope cantilever tip*, J. Micro/Nanolith. MEMS MOEMS, Vol. 6, 023012 (2007)

[9] Sonderforschungsbereich 605, *Elementarreibereignisse,* Leitung TU-Berlin

[10] Da Vinci, Leonardo, *Codex Arundel,* The British Library (Owner)

[11] Akademie der Wissenschaften Göttingen, Leipzig, München und Wien, *Encyklopädie der mathematischen Wissenschaften mit Einschluss ihrer Anwendungen,* page 199 pp Leipzig Verlag und Druck 1935

[12] F.P. Bowden, D. Tabor, *Friction and Lubrication,* Methuen & Co. LTD., London (1956)

[13] H. Hertz, *Über die Berührung fester elastischer Körper*, Journal für die reine und angewandte Mathematik 92, 156-171 (1882)

[14] D. Tabor, *Surface forces and surface interactions,* Journal of Colloid and Interface Science, 58(1), 2-13 (1977)

[15] V. M. Muller, V. S. Yushchenko and B. V. Derjaguin, *On the influence of molecular forces on the deformation of an elastic sphere and its sticking to a rigid plane,* Journal of Colloid and Interface Science, Vol. 77, 1, page 157-167 (1980)

[16] B. Cappella, G. Dietler, *Force-distance curves by atomic force microscopy,* Surface Science Reports Vol. 71, 1-3, page 1-104 (1999)

[17] K. L. Johnson and J. A. Greenwood, *An Adhesion Map for the Contact of Elastic Spheres,* Journal of colloid and interface science, 192, page 326–333 (1997)

[18] C. Mathew Mate, Gary M. McClelland, Ragnar Erlandsson, and Shirley Chiang, *Atomic-scale friction of a tungsten tip on a graphite surface*,
Physical Review Letters, Vol. 59, 17, page 1942-1945 (1987)

[19]E. Gnecco , R. Bennewitz, T. Gyalog, Ch. Loppacher, M. Bammerlin, E. Meyer , and H.-J. Güntherodt, *Velocity dependence of atomic friction*,
Physical Review Letters, Vol. 84, 6, page 1172-1175 (2000)

[20] Yaxin Song, Bharat Bhushan, *Atomic force microscopy dynamic modes: modelling and applications*
Journal of Physics: Condensed Matter, 20, 225012 (2008)

[21] V. Dworak, *Konzept eines hebelarmverstärkten Probenpositioniersystems mit piezoelektrisch/hydraulischem Hybridantrieb und aktiver Kompensation mechanischer und thermischer Störgrößen*,
Dissertation at the University of Wuppertal, Department of Electrical Engineering, ISBN 978-3-86844-144-4 (2009)

[22] M. Meincken, L. J. Balk, R. D. Sanderson, *Measurement of thermal parameters and mechanical properties of polymers by atomic force microscopy*,
Surface and Interface Analysis, Vol. 35, page 1034–1040 (2003).

[23] M. Modest, *Radiative Heat Transfer, 2nd Edition*,
Academic Press, ISBN: 978-0-12-503163-9, page 173

[24] C.P. Arora, *Refrigeration and Air Conditioning*,
Tata McGraw-Hill Publishing Company Ltd., ISBN: 0-07-463010-5, page 623

[25] M. Santamouris, *Environmental Design of Urban Buildings. An Integrated Approach*,
Earthscan, ISBN: 978-1-90-291642-2, page 127

[26] H. J. Mamin, *Thermal writing using a heated atomic force microscope tip*, Applied Physics Letters, Vol. 69, page. 433–435 (1996)

[27] Benjamin W. Chui, Kenneth E. Goodson, Robert P. Ried, *Low-Stiffness Silicon Cantilevers with Integrated Heaters and Piezoresistive Sensors for High-Density AFM Thermomechanical Data Storage*, Journal of Microelectromechanical Systems, Vol. 7 (1), page 69-78 (1998)

[28] Constant A.J. Putman, Bart G. de Grooth, Niek F. van Hulst and Jan Greve, *A theoretical comparison between interferometric and optical beam deflection technique for the measurement of cantilever displacement in AFM*,
Ultramicroscopy, 42-44, page 1509-1513 (1992)

[29] Takeshi Fukuma, Suzanne P. Jarvis, *Development of liquid-environment frequency modulation atomic force microscope with low noise deflection sensor for cantilevers of various dimensions*,
Rev. Sci. Instrum. **77**, 043701 (2006).

[30] T. Fukuma, M. Kimura, K. Kobayashi, K. Matsushige, and H. Yamada, *Development of low noise cantilever deflection sensor for multienvironment frequency-modulation atomic force microscopy*,
Rev. Sci. Instrum. 76, 053704 (2005)

[31] J. Selbeck, V. Dworak., Heinz Sturm, *Ersatz der Flusssäureätzung beim Dünnen von Lichtfasern aus Glas durch einen Schleifprozess*
(patent handed-in)

[32] J. Selbeck, V. Dworak., Heinz Sturm, *Optimierung der numerischen Apertur einer Lichtfaser durch Anschmelzen des Faserendes*,
(patent handed-in)

[33] M. Radmacher, J. P. Cleveland, P. K. Hansma, *Improvement of Thermally Induced Bending of Cantilevers Used for Atomic Force Microscopy*,
Scanning Vol. 17, 2 (1995)

[34] E.C.C.M. Silva, K. J. van Vliet, *Robust approach to maximize the range and accuracy of force application in atomic force microscopes with nonlinear position-sensitive detectors,*
Nanotechnology 17, page 5525-5530 (2006)

[35] Walter Schottky, *Small-Shot Effect And Flicker Effect.,*
Physical Review, Vol. 28, page 74-103 (1926)

[36] H.D. Motz, *Technische Mechanik,* Anhang A, page 135, 137, ISBN 3-8171-1371-4, Verlag Harri Deutsch

[37] Ivanov, Tzvetan, *Piezoresistive cantilevers with an integrated bimorph actuator,*
Dissertation at the University of Kassel, Department of Physics (2004)

[38] J. Selbeck, V. Dworak, H. Sturm, *Hydraulischer Antrieb für Aktuatoren und Positioniersystem für große Wege, bei hoher Kraft und mit Nanometerpräzision*
(Patent [DE 10 2008 030 981.8], European patent pending)

[39] C. C. Tanner, C. J. Migdal, M. T. Jones, The Clipmap: A Virtual Mipmap
Proceedings of the 25th annual conference on Computer graphics and interactive techniques, ISBN:0-89791-999-8, page 151-158(1998)

[40] M. K. Baller, H. P. Lang, J. Fritz, C. Gerber, J. K. Gimzewsk, U. Drechsler, H. Rothuizen, M. Despont, P. Vettiger, F. M. Battiston, J. P. Ramseyer, P. Fornaro, E. Meyer, H. J. Guntherodt, *A cantilever array-based artificial nose,* Ultramicroscopy, Vol 82, 1-4, page1-9 (2000)